NUMERICAL MODELING OF SEAFLOOR INTERACTION WITH STEEL CATENARY RISER

A Dissertation

by

JUNG HWAN YOU

Submitted to the Office of Graduate Studies of
Texas A&M University
in partial fulfillment of the requirements for the degree of

DOCTOR OF PHILOSOPHY

August 2012

Major Subject: Civil Engineering

NUMERICAL MODELING OF SEAFLOOR INTERACTION WITH STEEL CATENARY RISER

A Dissertation

by

JUNG HWAN YOU

Submitted to the Office of Graduate Studies of
Texas A&M University
in partial fulfillment of the requirements for the degree of

DOCTOR OF PHILOSOPHY

Approved by:

Co-Chairs of Committee,	Giovanna Biscontin
	Charles Aubeny
Committee Members,	Chloe Arson
	Jerome J. Schubert
Head of Department,	John Niedzwecki

August 2012

Major Subject: Civil Engineering

ABSTRACT

Numerical Modeling of Seafloor Interaction

with Steel Catenary Riser. (August 2012)

Jung Hwan You, B.S., Yeungnam University;

M.S., Texas A&M University

Co–Chairs of Advisory Committee: Dr. Giovanna Biscontin
Dr. Charles Aubeny

Realistic predictions of service life of steel catenary risers (SCR) require an accurate characterization of seafloor stiffness in the zone where the riser contacts the seafloor, the so-called touchdown area (TDA). This paper describes the key features of a seafloor-riser interaction model based on the previous experimental model tests. The seafloor is represented in terms of non-linear load-deflection (P-y) relationships, which are also able to account for soil stiffness degradation due to vertical cyclic loading. The P-y approach has some limitations, but simulations show good agreement with experimental data. Hence, stiffness degradation and rate effects during penetration and uplift motion (suction force increase) of the riser are well captured through comparison with previous experimental tests carried out at the Centre for Offshore Foundation Systems (COFS) and Norwegian Geotechnical Institute (NGI).

The analytical framework considers the riser-seafloor interaction problem in terms of a pipe resting on a bed of springs, and requires the iterative solution of a fourth-order ordinary differential equation. A series of simulations is used to illustrate the capabilities of the model. Due to the non-linear soil springs with stiffness degradation it is possible to simulate the trench formation process and estimate deflections and moments along the riser length. The seabed model is used to perform parametric studies to assess the effects of stiffness, soil strength, amplitude of pipe displacements, and riser tension on pipe deflections

and bending stresses. The input parameters include the material properties (usually pipe and soil), model parameters, and loading conditions such as the amplitude of imposed displacements, tension, and moment. Primary outputs from this model include the deflected shape of the riser pipe and bending moments along riser length. The code also provides the location of maximum trench depth and the position where the maximum bending moment occurs and any point where user is interested in.

To my parents, my sisters, and my wife

ACKNOWLEDGMENTS

I am deeply grateful to Dr. Giovanna Biscontin and Dr. Aubeny for their guidance and support during my graduate program at Texas A&M University. They provided the great opportunity and environment for the research work. I could develop myself and enjoy working on an interesting research topic under their support. Their assistance and guidance is gratefully acknowledged. I have learned a lot but there is still more to learn from them. I also appreciate my committee members, Dr. Chloe Arson and Dr. Jerome Schubert, for their advice and encouragement.

I want to extend my gratitude to Dr. Don Murff. He were really good mentor whenever I needed advice. Thanks also go to my friends and colleagues and the department faculty and staff for making my time at Texas A&M University a great experience. In addition, I would like to acknowledge the support of Department of the Interior Minerals Management Service, the Offshore Technology Research Center, Centre for Offshore Foundation Systems, and Norwegian Geotechnical Institute.

Finally, I deeply appreciate my parents and sisters for their endless support and encouragement in my life. I would also like to express my appreciation to my lovely wife, Sujung, her family, and my son, Eric. Their dedication and encouragement led me to the completion of this dissertation.

TABLE OF CONTENTS

CHAPTER Page

CHAPTER Page

LIST OF TABLES

LIST OF FIGURES

FIGURE Page

FIGURE Page

FIGURE Page

FIGURE Page

FIGURE Page

CHAPTER I

INTRODUCTION

1.1. Overview

Recently, development offshore technologies and increased economical efficiency due to high oil price has led to the more intense exploitation of petrolic products in increasingly deep water environments (up to 3,000 m). This need to develop oil and gas fields. The steel catenary riser (SCR) is the system conveying the oil and natural gas from the seabed well to the large floating structure anchored to the seafloor by mooring lines. The migration of the work area to deep or ultra-deep water need longer risers which require more complex dynamic analysis and raise more concerns about the seafloor interaction with riser influencing the riser motion loaded by extreme storms, vessel movements, and vortex-induced vibrations.

Deep sea or ultra deep sea has required a transition to steel catenary riser systems instead of the conventional method. Steel catenary risers (SCRs) offer a low cost alternative to rigid and flexible risers on floating platforms and can also provide economic riser design solutions for fixed platforms by relative cost savings made as a result of the simplified arrangement (Howells, 1995). Furthermore, steel pipe is more adaptable for design purposes (specially submarine environment such as low temperature and large external pressure) and has better availability than flexible pipe. Risers with simple tubular cross-sections offer several advantages over flexible risers made of numerous layers of different materials. In addition, steel pipe configurations maintain curvatures that cause little bending and thus make them better suitable for deep water use. Due to these advantages of SCRs, they have

---

This dissertation follows the style of the *Journal of Geotechnical and Geoenvironmental Engineering.*

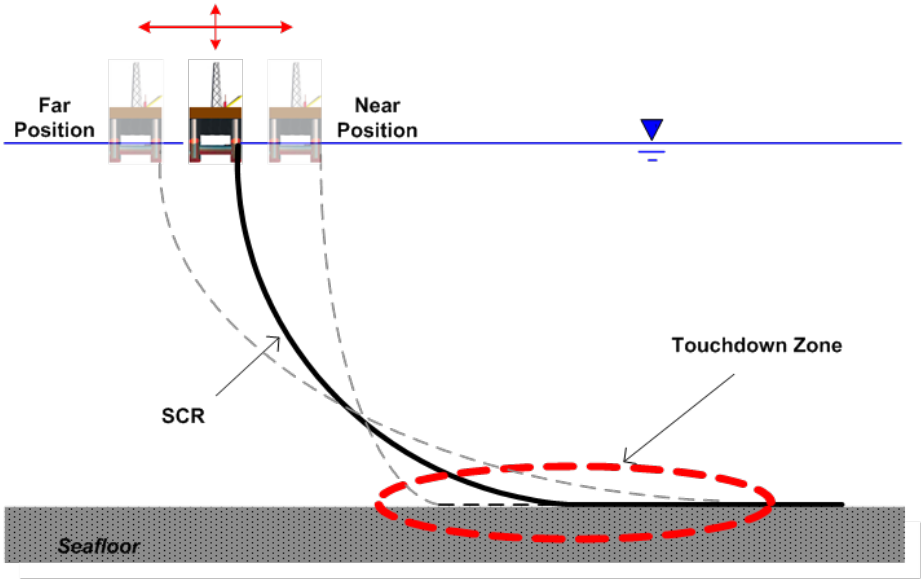

Fig. 1. Seafloor-Riser Interaction Problem

been chosen as the primary method to transfer carbonate resource from the deep sea.

The fatigue life of a riser pipe is one of the critical issues when designing a riser system. In particular, it is difficult to estimate fatigue stresses accounting for the riser-seafloor interaction behavior because of the high non-linearity of the soil response. The touchdown zone (TDZ) where the SCR contacts the seafloor (Fig. 1) has often proved to be the critical location for fatigue analysis, since the maximum bending stresses usually occur in this part of the riser (Bridge et al., 2003, 2004). In addition, these studies have also shown fatigue damage to be sensitive to seafloor stiffness.

The full-scale (Bridge et al., 2004; Bridge and Willis, 2002) and model tests (Aubeny and Biscontin, 2008; Clukey et al., 2005; Langford and Aubeny, 2008) conducted to better understand the seabed response to riser's motion, showed complex behavior including trench formation processes, non-linear soil behavior involving plastic penetration, soil suction and separation of the riser from the soil; as well as degradation of seafloor stiffness under cyclic loading and strength recovery due to thixotropic phenomena or consolidation.

Although linear elastic seafloor models (Pesce et al., 1998) and equivalent linear soil stiffness models (Bridge and Willis, 2002; Fontaine et al., 2004) calibrated with model tests provide very useful insights about seafloor-riser interactions, they cannot fully describe the complex interaction problem. Recently proposed P-y models (Aubeny et al., 2006; Randolph and Quiggin, 2009) can describe all phases such as penetration, partial separation after elastic rebound, full separation, and reloading conditions a riser may be subjected to. However, they do not account for the reduction in soil stiffness due to repeated uplift and lay-down movements of the riser pipe.

The proposed study will include a semi-empirical model for seafloor-riser interaction developed after the extended review of previous work (Dunlap et al., 1990; Aubeny and Biscontin, 2008; Clukey et al., 2005; Langford and Aubeny, 2008) to describe seabed response under cyclic loading conditions. The model has the ability to account for the initial riser penetration into the seabed (backbone curve), the unloading phase when riser and soil are still in contact, the suction generation, the riser separation from the seabed, and the riser re-penetration. The seafloor response for each mode is described by a mathematical relationship between load and displacement (P-y). Furthermore, the model considers the effects of the penetration rate, the degrading of the seabed stiffness, and the regained soil stiffness by consolidation. The proposed model will be also validated through comparison with experimental results.

In addition, this research will provide an analytical framework for simulating seafloor-riser interaction as a linearly elastic pipe with a series of non-linear P-y models. The proposed seafloor-riser interaction model considers only vertical riser motions. Although lateral motions of the riser also affect riser performance (Hale et al., 1992; Morris et al., 1988), observations for current installed risers indicate that typical riser trenches are about 4 pipe diameters wide. Therefore, significant lateral soil resistance will be mobilized only when the pipe is pushed into contact with the walls of the trench. Otherwise, vertical

soil resistance will be generated during every load cycle, even if displacements are small in amplitude. In addition, the magnitude of the soil resistance is generally greater in the vertical than in the lateral direction, due to the greater confinement provided with depth. This seafloor-riser interaction model considers only the length of the riser comprising the touchdown zone. Small displacement beam analysis is adapted to treat the interaction problem, since the typical ratio of trench depth to trench length is about one percent. The end moment, generated by large uplift motions at the touchdown point (TDP) and axial tension in the riser are also considered as boundary conditions in the model.

1.2. Research Objectives and Scope

The main goal of the proposed work is to understand seafloor-riser interaction mechanisms and to develop a numerical seabed model for the seabed-riser interaction behavior and an analytical model to predict the riser configuration, the trench evolution, and the maximum bending moment of the riser due to its vertical motion within the touchdown zone. In particular, the following objectives will be addressed:

- Objective 1: Observation on previous model tests

  Analyze the previous model test data to better understand the complex non-linear soil-riser interaction response.

- Objective 2: Development of the Non-Degrading P-y Model

  Develop a non-degrading load-displacement (P-y) model to describe the interaction response of riser and seafloor with analytical descriptions for each mode including penetration into seabed, uplift under contact with seabed, separation from seabed, and re-penetration, as shown in model tests.

- Objective 3: Development of the Degrading P-y Model

Develop a degrading P-y model by using the proposed degrading rule.

- Objective 4: Parametric study and Validation for the proposed P-y Models
  Investigate the effects of various model parameters on the P-y curves and validate the model against experimental model tests.

- Objective 5: Development of the Interaction Model
  Develop the global riser-seafloor interaction model with a seabed model within the touchdown zone. The response of the seafloor to SCR movements will be studied to identify proper boundary conditions at the seafloor touchdown zone for structural analysis of a riser subjected to up and down loading. The relative importance of various seafloor and loading conditions on bending stresses of the riser pipe by the proposed P-y models will also be investigated.

- Objective 6: Parametric Study and Validation for the Interaction Model
  Carry out a parametric study on the interaction model and validate the developed numerical interaction model with large scale testing (harbor test).

1.3. Organization of Dissertation

A brief description of the organization of the chapters that form this dissertation follows:

Chapter II deals with a summary and review of previous works related with the seafloor-riser interaction problem.

Chapter III discusses observations of previous experimental model tests and investigates the characteristics of soil-riser interaction response to apply in the development of the seabed model.

Chapter IV describes the proposed non-linear degrading seabed model, presents an investigation of the effect of each parameter on the seabed model and suggests an acceptable

range of parameter values from parametric studies. Further, the developed seabed model simulations are compared with real model test results.

Chapter V explains the interaction model involving the nonlinear seabed spring model. The governing equation transformed by a central finite difference (FD) method is adapted to predict SCR behavior under variable conditions of loadings, seafloor support, and material properties.

Finally, summary and conclusions are presented in Chapter VI with the recommendations for future work.

CHAPTER II

LITERATURE REVIEW

2.1. Steel Catenary Riser (SCR) System

2.1.1. Offshore Risers

Risers are conduits to conveying hydrocarbon materials (oil or gas) from seabed to floating production platform. Subsea risers are one of pipeline types developed for vertical transportation. There are a number of different risers, which include attached risers, steel catenary risers, top-tensioned risers, hybrid risers, and drilling risers.

- Attached Risers: Led on Fixed Platforms, Concrete gravity Structures and Compliant Towers.
- Steel Catenary Risers: Connect Seafloor facilities to production facilities above as well as floating production platforms
- Top Tensioned Risers: Completely vertical systems that terminate directly below the facility.
- Hybrid Risers: Ideal for floating facilities as vertical and horizontal movement take place.
- Drilling Risers: Connect the blowout preventers (BOP) on top of the well at the bottom to the rig at the top, and transport the drilling fluid to surface.

Especially, a steel catenary riser (SCR) prolonged from sub-sea pipeline attached to a floating structure in a catenary shape has been one of attractive choices at offshore industry after first use in 1994 by Shell on the auger tension leg platform moored in 872 m off water

(Mekha, 2001). The risers are typically 8-12 inches in diameter and operate at a pressure of 2000-5000 psi (Howells, 1995; Hatton and Willis, 1998).

2.1.2. SCR Behavior

Steel catenary riser (SCR) systems have become an attractive choice for deep water developments. The basic concept of the riser system is to connect between a floating production vessel and pipelines on the bottom by way of a flex joint. The steel catenary riser is linked to a receptacle on the floating platform and hangs at a prescribed angle to keep a stable catenary shape. The top connection point is subjected to high tension forces due to the weight of the whole length of riser. The SCR is free-hanging and extends down to the seafloor to the touchdown point (TDP) where the SCR becomes buried in a trench. The last portion of riser pipe lays on the surface where it is effectively a static pipeline.

The application of SCRs from floating production in deep water harsh environments presents design challenges, due to the large wave-induced motions on the platform and large vessel offsets caused by wind, current, and slow-drift wave motions. There are also buckling issues at the touch down point (TDP), caused by large heave and surge motions, and fatigue problems due to vessel motions and soil-riser interaction.

SCR designs are very sensitive to the motion characteristics of floating support platforms or vessels to which they are typically attached. The floating structure moves back and forth or up and down by wave action. Even though the movement of floating platforms involve a small degree of vertical motion, mostly they move laterally. The typical positions as shown in Figure 2 include:

- Nominal position: the structure is in its initial position without displacement in any directions.
- Far position: the structure is displaced in the plane of the SCR away from the TDP

for the nominal position, causing the departure angle to increase with a shorter length of the SCR lying on the seabed.

- Near position: the structure is displaced in the plane of the SCR towards the TDP of the nominal position, causing the departure angle to decrease with a longer length of the SCR lying on the seabed.

- Cross offset position: the structure is displaced out of the plane of the SCR with the structure in the in-plane nominal position.

Even though the TDP is a critical location when designing the SCR due to its largest curvature, it is important to note that the TDP changes location along the SCR due to the platform motion. Therefore, the terms touchdown zone (TDZ) or touchdown area (TDA) are more applicable to describe this location.

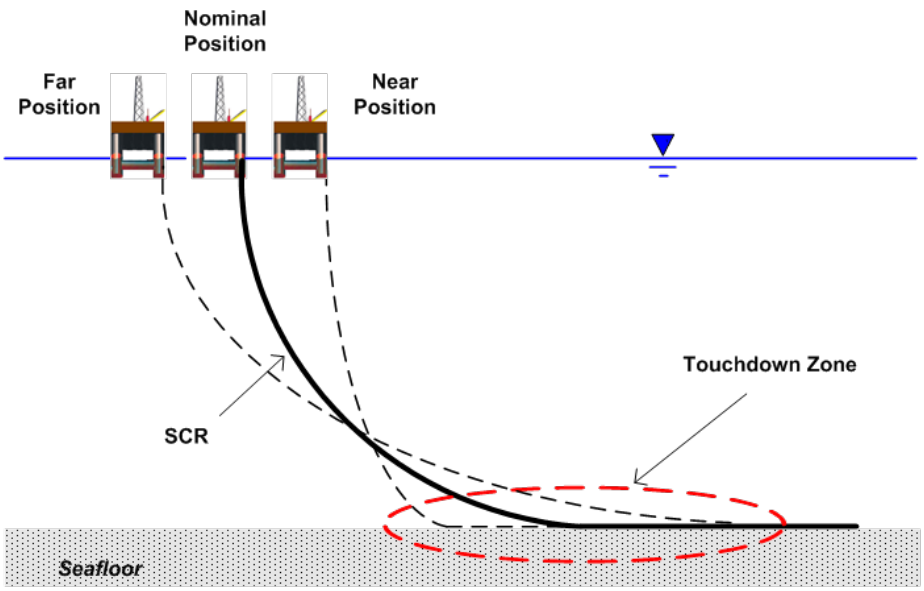

Fig. 2. Riser Shape Change depends on Positions of Floating Platform

The dynamic motions of the SCR as a direct effect of waves cause the riser to change shape resulting in fatigue damage and high stresses near the touchdown zone. A potential fatigue failure is directly related to the maximum bending stress and moment in the SCR, which depend on the stiffness and damping of the seafloor and the motions of the SCR. For example, an SCR on a soft seafloor will have reduced bending stresses when a load is applied, while one on a rigid seafloor will have more critical bending stresses.

The other loads affecting SCR design are vortex induced vibration (VIV) and extreme storms. VIV may result in severe fatigue damage in many geographic locations where current velocities are high. Even though the sensitivity to VIV increases due to the lower tension near the bottom of the risers, in the touchdown area (TDA), extreme current velocities are often much lower near the seabed than at the surface.

Storm loading results in an increase in the stress level, which may become unacceptable in extreme conditions. However, the large water depths are also beneficial in that dynamic excitation from extreme wave action at the surface is damped as it travels to the seabed (Howells, 1995) and extreme storm stresses are not particularly sensitive to seabed stiffness (Theti and Moros, 2001).

2.1.3. Riser Installation

One of critical factors when designing SCR is complete and successful installation without damage. The damage during the installation process can directly reduce the fatigue life of SCRs. There are many types of SCR installation methods such as J-lay, S-lay, reel, and hybrid. J-lay (Fig. 3) has been widely selected as the leading method as development field is moving to deepwater. Riser stalks of up to 6 joints are prefabricated onshore, reducing the number of welds that need to be made during offshore installation. J-lay collars used to support the pipe during installation are welded around the pipe and can act as buckle arrestors. The advantages of J-lay include reducing the tensions and moments in the riser

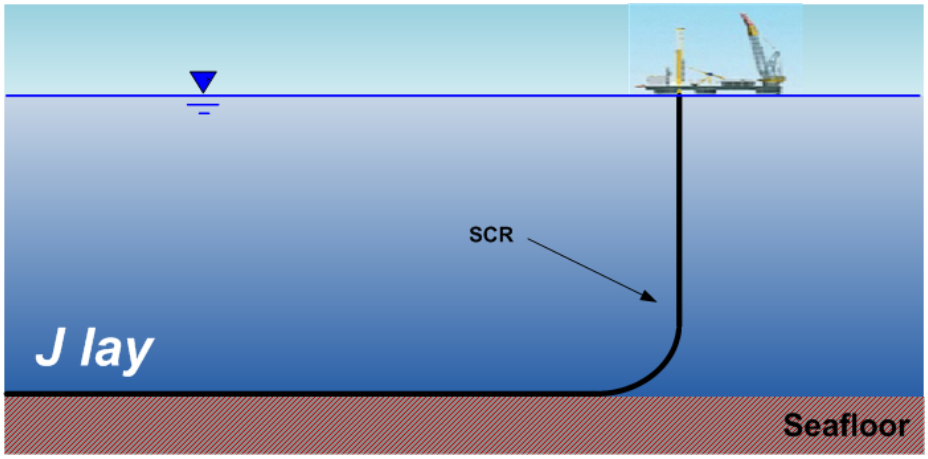

Fig. 3. J-lay Installation Method

pipe to the minimum in TDZ and top joint section when compared with other installation methods such as S-lay and reel methods. J-lay is also suite for all diameters. However, the J-lay may be more expensive than other methods due to a limited number of vessels which have J-lay capability.

The S-lay method (Fig. 4) is another option to install SCR. It is similar to the J-lay method, except the pipes are handled in the horizontal position, allowing multiple joints to be welded simultaneously. The technique is generally not well suited to deepwater due to the very high back tensions required to prevent overstressing of the sag bend and over bend. This high back tension also makes dynamically positioning the installation vessel difficult. Consequently, increased water depths reduce the number of capable installation vessels. Prior to the decision to install the strakes with the SCRs by the S-lay method, tests were performed to demonstrate the feasibility of strakes passing over the rollers of the S-lay vessel stinger, and withstanding the loads imposed on the strakes without damage. The Prince SCRs (Mekha and Heijermans, 2003) were also designed to accommodate residual stresses and strains during installation using the S-lay method.

To overcome the cost disadvantage of J-lay and to satisfy the stress and fatigue design

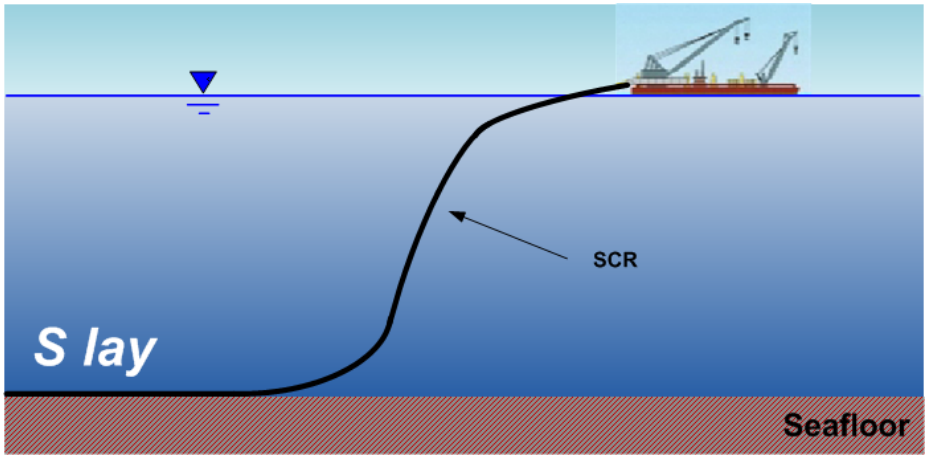

Fig. 4. S-lay Installation Method

requirements, a hybrid installation approach was introduced. One of the typical hybrid methods is the combination of S-lay and J-lay methods. The entire export pipeline system including the SCRs is installed using the S-lay method with the exception of the top section of the SCRs where the VIV strakes were needed. This top section with strakes is installed using the J-lay method. Special attention is required in examining the fatigue behavior of the SCRs, because of residual stresses and strains that were imposed on the SCR pipe during the S-lay installation. Another method is the hybrid reel and J-lay method. The SCR intermediate section between the touchdown section and the top joint section where fatigue is not critical and the export pipeline system are installed by the reel-lay method. The J-lay mode of the same installation vessel is used for installation of the SCR's two fatigue critical areas, touchdown and top joint section because the SCR by using reel-lay method can have plastically strained to about 200 percent of the yield strain after installation.

2.1.4. Characteristic of Deepwater Marine Clay

Unlike offshore foundations, the critical depth range with respect to pipelines in the deep-water environment is limited to up to 1 m from the surface of the seabed, corresponding to

an observed trench depth of 5 to 6 riser diameters near the touchdown area turned (Bridge and Howells, 2007). Most marine deposits consist of very soft clays characterized by low undrained shear strength and high void ratio. The undrained shear strength is a critical parameter needed for design of SCRs. The undrained shear strength profile can generally be defined as function of depth (z).

$$S_u = S_{uo} + S_g z \tag{2.1}$$

where S_{uo} is the undrained shear strength at the surface of the seabed and S_g is the shear strength gradient with depth. Figure 5 shows a typical range for strength of marine clay. S_{uo} may generally be taken as 0 to 4 kPa while the intact strength gradient may be as high as 0 to 20 kPa. In-situ strength measurement tools have been developed to measure the low shear strength near the mud-line and obtain more accurate values of soil strength. The shear vane and various penetrometers (T-bar, ball) are widely used field testing tools.

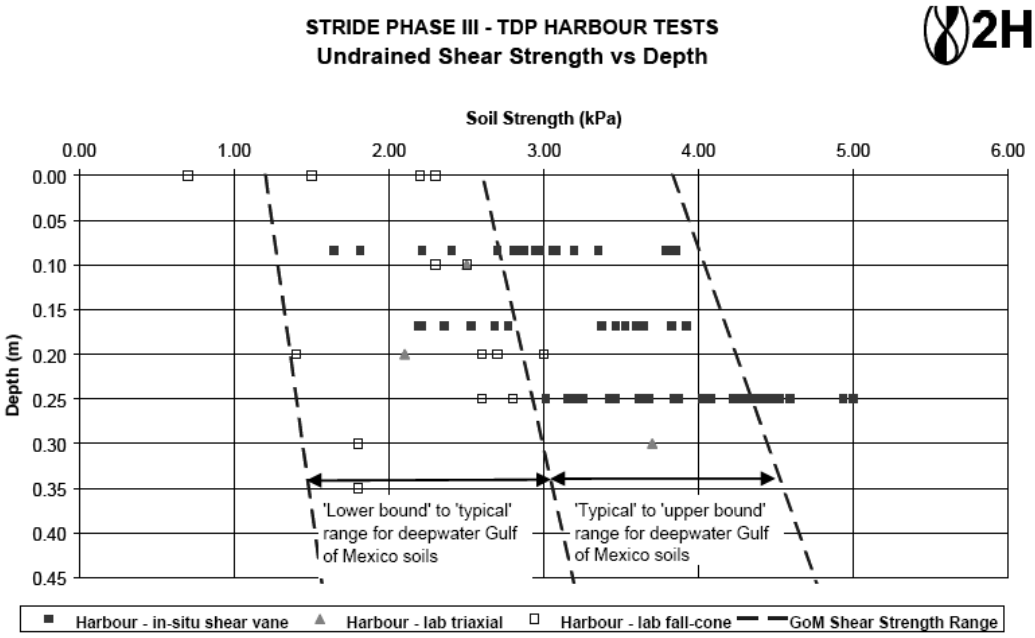

Fig. 7 – Seabed Shear Strength

Fig. 5. Undrained Shear Strength in the Gulf of Mexico (Willis and West, 2001)

2.2. SCR-Seabed Interaction Behavior

2.2.1. Trench Formation Process

The riser movements caused by a variety of sources, such as currents as well as the motion of the floating structure, result in the formation of a trench on the seabed. The SCR can be decided into three regions: catenary zone, buried zone, and surface zone (Fig. 6). The catenary zone means the riser hangs in a catenary shape. The buried zone is where the riser is in a trench formed by the riser interaction with the seabed. Finally, the surface zone indicates that the riser statically rests on the seafloor.

In the buried zone beyond the TDP, deep trenches cut into the seabed. Figure 7 illustrate trench formation by repeated vertical riser motion in the buried zone based on real trench observations. The trench near the touchdown point is wide and shallow, although vertical movement of the SCR is large. At the mid-point of the buried zone, the riser motion forms a deeper and narrower trench.

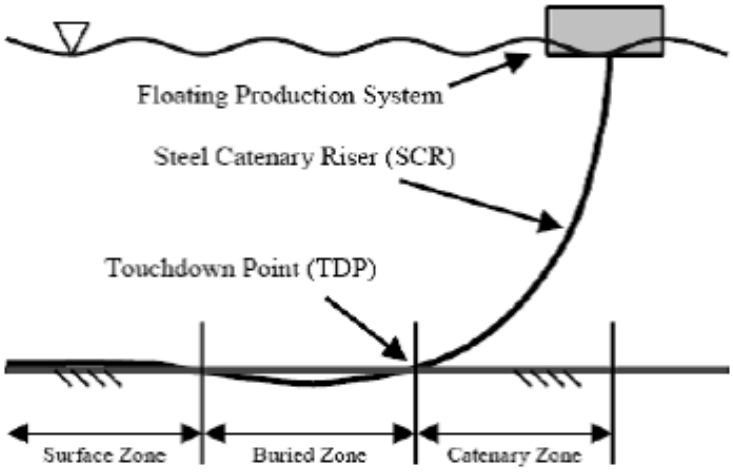

Fig. 6. General Catenary Arrangement (Bridge et al., 2003)

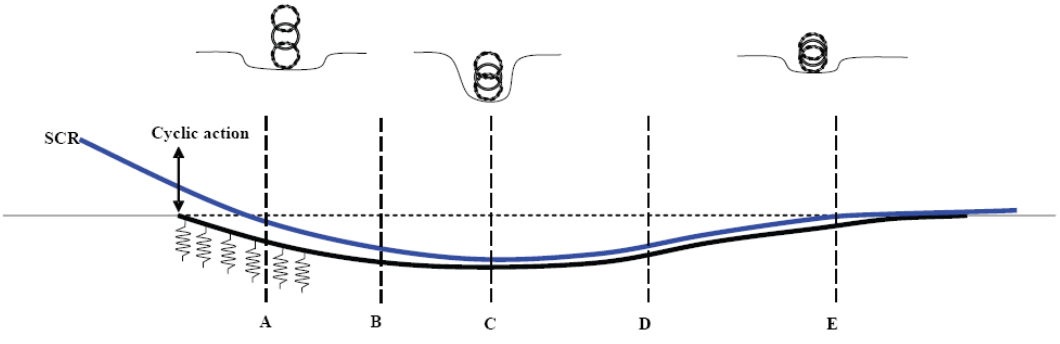

A	Shallow trench with small suction and no effect of lateral soil
B	Deeper trench (2-3xOD) with increasing embedment due to lateral SCR motions
C	Deep (up to 5xOD) and narrow trench with the pipe completely embedded. The maximum break out resistance is at its maximum
D	Shallow trench with some embedment
E	Shallow and narrow trench close to static condition

Fig. 5 Typical SCR Trench Characteristics – WoA FPSO Applications

Fig. 7. Typical SCR Trench Characteristics (Amicis et al., 2008)

The mechanisms of trench formation are not well understood because the response of the riser at the seabed TDP and the interaction with the seabed is complex. However, it is thought that the dynamic motions of the riser, including scour, sediment transport, and seabed currents produce the trench. Also, storm and current action can pull the riser upwards out from its trench, or laterally against the trench wall.

The complex resistance of the seabed soil can be divided into a vertical, lateral and axial components relative to the riser longitudinal axis. The vertical soil resistance show different characteristics depending on the direction of the riser motion, uplift and lay-down. On the lay-down (downward) cycle, the soil behaves to some degree elastically at small initial penetration strains. On the uplift cycle, the seabed soil generates a suction force on the riser due to the soft clay adhering to the pipe. Hence, a considerable vertical pull force is required to completely break out from the suction phenomenon. Lateral resistance consists of friction between the riser and seabed, and the passive resistance of the soil as the

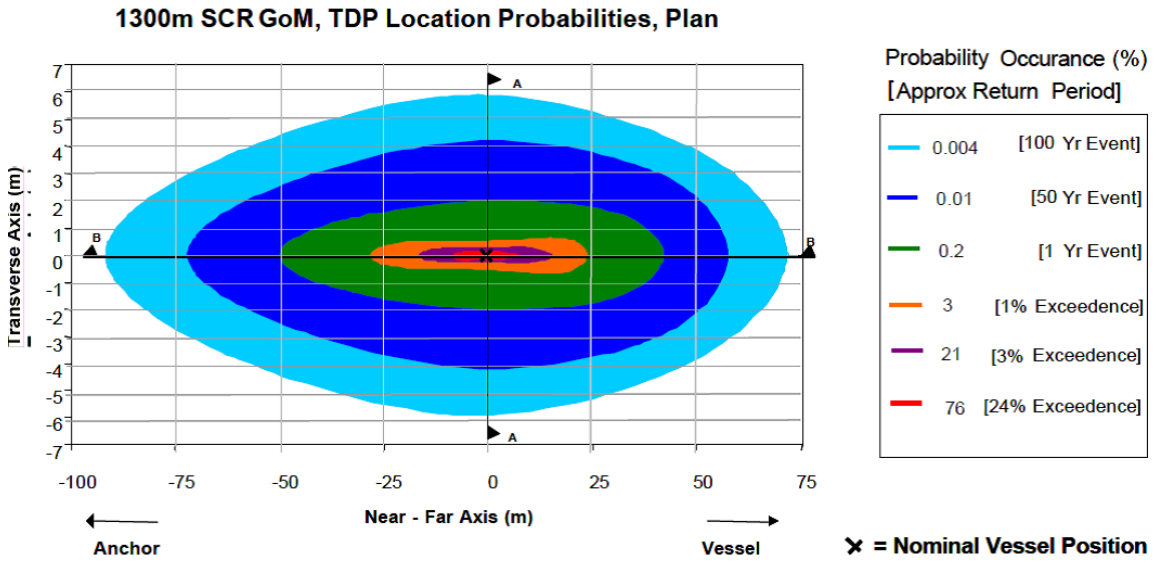

Fig. 8. SCR/Spar TDP Global Dynamic Movements **?**

riser moves sideways out of a depression or into a trench wall. Finally, the axial resistance is the function of friction coefficient.

Figure 8 shows the occurrence of TDP movements defending on environmental loading and vessel motions over the service life. TDP mapping is useful in defining the TDZ limits and identifying sections of the riser in the TDZ that move very frequently such that the soil within this region is always in a remolded condition. The plot indicates that the riser motion occurs within 35 m of the long strip area, indicating that the vertical riser motion rather than lateral or axial dominates the dynamic motion of the riser. Hence, most of the previous studies (Bridge et al., 2004; Clukey et al., 2005) focused on the vertical interaction between seabed soil and riser.

Bridge et al. (2004) developed advanced models using published data and data from the pipe and soil interaction experiments conducted within the STRIDE and CARISIMA JIP's. They describe an example of the development of a pipe-soil interaction curve with an unloading and reloading cycle, as presented in Figure 9. The mechanism of pipe and

soil interaction is described in the following steps:

1) The pipe is initially in contact with a virgin soil.

2) The pipe penetrates into the soil, plastically deforming it. The pipe and soil interaction curve tracks on the backbone curve.

3) The pipe moves up and the soil acts elastically. The pipe and soil interaction curve move apart from the backbone curve, the force decreases over a small displacement.

4) The pipe resumes penetrating the soil, deforming it elastically. The pipe and soil interaction curve follows an elastic loading curve.

5) The pipe keeps going to penetrate into the soil, plastically deforming it. The pipe and soil interaction curve meets again with the backbone curve and tracks it.

In addition, Bridge et al. (2004) updated the force-displacement curve and considered the soil suction effect, as shown in Figure 10 and described below:

- Penetration - the pipe penetrates into the soil to a depth where the soil force equals the penetration force.
- Unloading - the penetration force reduces to zero allowing the soil to swell.
- Soil suction - as the pipe continues to rise the adhesion between the soil and the pipe causes a tensile force resisting the pipe motion. The adhesion force quickly increases to a maximum then decreases to zero as the pipe pulls out of the trench.
- Re-penetration - the re-penetration force-displacement curve remains at zero when the pipe enters the trench again, only increasing when the pipe re-contacts the soil. The pipe and soil interaction force then increases until it rejoins the backbone curve at a lower depth than the previous penetration.

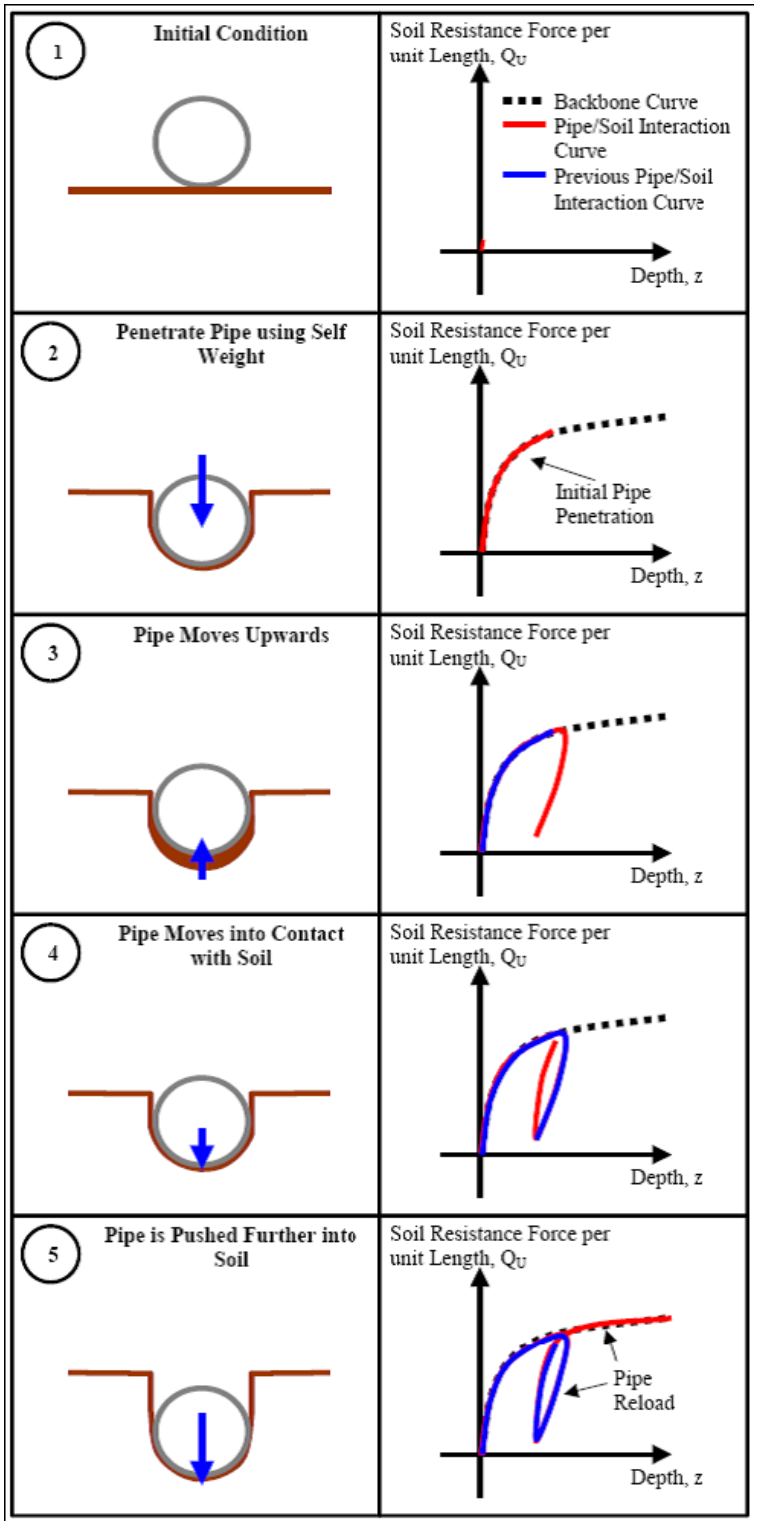

Fig. 9. Illustration of Pipe-Soil Interaction (Bridge et al., 2004)

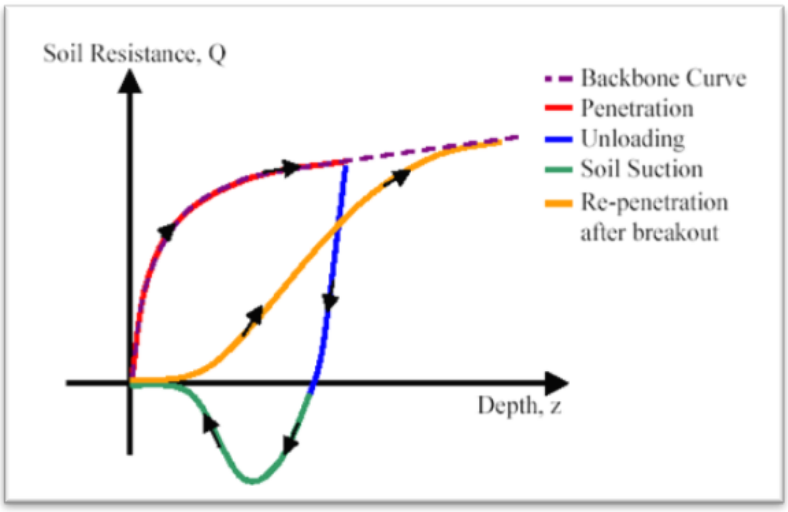

Fig. 10. Pipe-Soil Interaction Curves (Bridge et al., 2004)

The seabed soil also experiences stiffness degradation due to cyclic loading, consolidation and thixotropy during the service life of the SCR. Previous model tests (Clukey et al., 2005; Aubeny et al., 2008) show there is certainly a tendency for the soil stiffness to be reduced as the number of cycles increases under displacement controlled test. It is possible that the trench depth is slowly increased due to iterative riser movements even without extreme loading from a storm. Time-related soil resistance recovery could be significant under certain circumstances (Langford and Aubeny, 2008). If there is no riser motion in the buried zone, soil resistance increases and the trench depth is sustained without any large change until extreme riser motion initiates.

2.2.2. Load-Deflection (P-y) Curves

To describe riser-seafloor interaction behavior, most previous studies have developed numerical models based on load-deflection (P-y) curves inferred from laboratory model test. P-y curves are often used to solve the problem of a laterally loaded pile using the concept of a beam on an elastic foundation (Winkler model).

Currently employed P-y curve models were developed based on the results of field tests by Matlock (1970) and Reese et al. (1974). The traditional P-y curve models are semi-empirical models in which soil response is characterized as independent nonlinear springs at discrete locations. The P-y curves are adjusted mathematically involving nonlinear modeling of the soil-pile interaction response using empirical parameters to extrapolate beyond the soil's specific field test conditions. In this method, a finite-difference solution is obtained to the following equation:

$$\frac{d^2M}{dz^2} + T\frac{d^2y}{dz^2} - P = 0 \tag{2.2}$$

The term M and T mean the bending moments of beam and the axial load, respectively. In addition, the load term P designates the soil resistance in units of force per unit length. In addition, the y refers to the vertical displacement of the riser pipe. This equation includes the effects of axial load and variations of pile stiffness with depth can also be incorporated. The equation above can be written in finite-difference form, and a full description of the resulting equations was given by Reese and Desai (1977). Design procedures for constructing P-y relationships based on the results of field measurements on full-size instrumented piles, have been developed by Matlock (1970) for saturated soft clays subjected to either short-term static loading or cyclic loading. Other cases have subsequently been treated by Reese and his co-workers and are summarized by Reese and Welch (1975).

Dawson (1980) presented simple method for predicting lateral response of deeply

driven piles based on the work by Matlock (1970) for clays and Reese et al. (1974) for sands. The theory assumes a linear relationship between the soil resistance and pile deflection up to a critical displacement level, after which it remains unchanged with further increases in displacement. The soil response to elastic and plastic parts by the critical displacement depth.

P-y curves can be employed in a comprehensive numerical soil-structure interaction analysis (e.g., a finite- element program) to model the soil-pile response of a structural problem involving the superstructure along with the substructure.

Grashuis et al. (1990) introduced the numerical model (TILLY) based on Matlock (1970) and Skempton (1951) to calculate the cyclic response of laterally loaded foundation piles. The backsliding of the gap has been modeled by a reduction of the gap length as a function of the actual soil strength. The friction between pile and slot-wall has been included using an elasto-plastic interaction. However, this model did not include the tensile stress state that occurs during the unloading in experiments of Matlock.

Ashour and Norris (2000) considered the additional effect of soil and pipe properties to develop the traditional P-y curves by strain wedge (SW) model formulation. The SW model (Ashour et al., 1998) provides a theoretical means for developing P-y curves that reflect the influence of pile bending stiffness, pile cross-sectional shape, pile-head fixity, and pile-head embedment that have an effect on the resulting P-y curves. Also, the SW model includes the relation of stress-strain-strength behavior of the layered soil in the wedge to a beam on an elastic foundation (BEF) to allow the appropriate selection of BEF parameters for solving the differential equation (Eq. 2.2).

Fontaine et al. (2004) conducted a series of experiments to better comprehend and measure the averaged vertical stiffness and equivalent damping describing the soil-pipe response under static and cyclic loading with different pipe diameters (D) and soil strengths (S_u). From the tests, they observed that the stiffness (K) decreases rapidly towards a low

level as the cycle amplitude (a) increases, indicating the vertical stiffness is directly proportional to the soil cohesion and the relative amplitude of the imposed motion is the main parameter driving its evolution. In addition, at the average percentage of critical damping ranges almost linearly from 0.5 to 0.9 for a/D varying 0 to 0.35. They especially emphasized the importance of the choice of the design value for the soil cohesion since the average vertical soil stiffness varies as a linear function of the soil cohesion and pipe diameter.

2.2.3. Static Penetration

Classical approaches to estimating static pipe penetration into soil are constructed using bearing capacity theory for strip footings. The ultimate vertical load per unit length of pipe applied on soil expressed in terms of the undrained shear strength (S_u), submerged unit weight (γ), and bearing width of pipe (B) is defined as:

$$Q_u = q_u B = (N_c S_u + \gamma z) B \tag{2.3}$$

where z is the invert depth of pipe. The term γz is applicable only for no backfilled or buried foundation. **?** substituted equation 2.1 into 2.3 and calculated the bearing factor N_c as follows:

$$Nc = 5.14 \left(1 + 0.23\sqrt{\frac{z}{B}}\right) \tag{2.4}$$

where the bearing factor cannot exceed 7.5 and the bearing width in the penetration range smaller than half diameter is $2\sqrt{Dz - z^2}$.

Murff et al. (1989) suggested upper and lower bound plasticity solutions for pipes with full adhesion and no adhesion. This plasticity solution also included the effect of heave and strength increase with depth. Dunlap et al. (1990) proposed an empirical estimate for pipe embedment under monotonic loading based on an experimental study to explain the effect of penetration velocity (v). The suggested formula shows a nonlinear relationship

Table 1. Fitting Coefficients for Power Law, $N_p = a(z/D)^b$ (Aubeny et al., 2005)

Boundary Roughness	Coefficients a, b	
	$z/D < 0.5$	$z/D \geq 0.5$
Smooth	a = 4.97	a = 4.88
	b = 0.23	b = 0.21
Rough	a = 6.73	a = 6.15
	b = 0.29	b = 0.15

between embedment depth and the penetration force with an inverse dependency on the shear strength and pipe diameter as given below:

$$\frac{z}{D} = 0.01573 \left[\frac{P/D}{S_u (v/D)^n} \right]^{1.7822} \tag{2.5}$$

where P and n are force per unit length of pipe and non-dimensional visco-elastic rate (0.03 for test soil), respectively. Also, the term v/D represents a nominal shear strain rate.

Aubeny et al. (2005) reported numerical simulations of the collapse load for a cylinder embedded at the bottom of a vertically sided trench in cohesive soil. Based on Murff's approach, they extended the plasticity solution for a seabed with linearly increasing shear strength with depth. They suggested a power law expression of the normalized load in terms of shear strength at the pipe invert, expressed as:

$$\frac{P}{S_u D} = a(z/D)^b \tag{2.6}$$

Fitting coefficients a and b for limiting conditions of roughness (perfectly smooth and rough) were given as detailed in Table 1.

Bruton et al. (2006) proposed another force-displacement response model based on large and small scale tests performed on deepwater soils from the Gulf of Mexico and West

Africa, and also in kaolin. This model is expressed as:

$$\frac{z}{D} = \frac{S_t}{15}\left(\frac{P}{DS_u}\right)^2 \tag{2.7}$$

where S_t is the soil sensitivity. Although the model does not account for the variation of the soil shear strength with depth and needs further improvement of the model in this area, Bruton et al. (2006) commented on the discrepancy between the model and the classical plasticity solution (Murff et al., 1989) even for a sensitivity value of 1.0. They suggest that the discrepancy might be due to additional consolidation settlement in the test data or over-estimation of the shear strength at shallow penetration due to softening close to the free surface.

Randolph and White (2008a,b) presented yield envelopes obtained from tipper-bound plasticity solutions for pipeline embedment of up to $0.5D$ in clay soil, offering a simple way to estimate the embedment resistance for various combinations of horizontal and vertical loading. They also considered linearly increasing shear strength with depth, but ignored the effect of self-weight due to its small role at shallow embedment for common ratios of effective stress to shear strength. They also discussed the significant importance of buoyancy and local heave on the penetration resistance for a given embedment and compared the results with large deformation finite element (LDFE) analysis.

2.2.4. Breakout Force

Published literature on the breakout phenomenon is relatively scarce. Some interesting empirical results from long-lasting marine salvage operations and extrication of sunken ships from the seabed are presented in Poinc's book (Poinc, 1970). He proposed a rough estimate for the magnitude of the force (F) necessary to lift up the object from the seabed:

$$F = (1 + k_p)G \tag{2.8}$$

where k_p denotes an empirical coefficient which depends on the subsoil type, k_p = 0.05-0.1 for coarse sands, k_p = 0.15-0.2 for fine sands, and k_p = 0.25-0.45 in the case of a clayey bottom. It should be noted that equation 2.8 gives only approximate prediction with respect to the magnitude of the uplift force, since the breakout force is strongly related to factors such as object shape, size, degree of embedment in bottom sediments, and breakout time necessary to raise the object. An essential conclusion which follows from Poinc's empirical observations is that the type of subsoil has a great influence on the amount of force required to detach the object from the seabed (Sawicki and Mierczynski, 2003).

Previous studies (Bouwmeester et al., 2009; Das, 1991) proposed relationship between breakout force, rest time and unloading velocity. Longer rest time increases uplift force while shorter breakout time develops larger suction force. Figure 11 shows a reasonable coefficient of determination R^2 = 0.76 between the breakout force ratio and the rate of loading, with an expected trend of breakout force ratios increasing as the rate of loading increases. Thus, when breakout time was shorter suction forces were stronger.

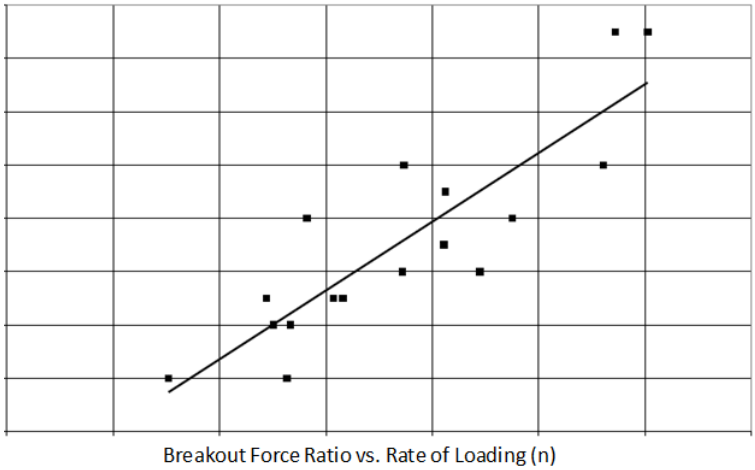

Fig. 11. Breakout Force Ratio vs. Rate of Loading (n) (Bouwmeester et al., 2009)

2.3. Harbor Test

A number of studies have been directed toward understanding the mechanism of steel catenary riser behavior. The first, the full-scale test to research the effects of fluid, riser and soil interaction on catenary riser and stresses in riser pipe at the touch down point (TDP) was conducted over 3 months at Watchet Harbor in the west of England by the STRIDE JIP, 2H Offshore Engineering Ltd in 2000 (Willis and West, 2001). The purpose of the full-scale test was to estimate the significance of fluid, riser and soil interaction and to develop finite element analysis techniques to predict the measured response.

A 110 m (360ft) long 0.1683 m (6-5/8 inch) diameter riser pipe was used for this experiment. The riser was connected with an actuator on the harbor wall to an anchor point on the seabed. A programmable logic controller (PLC) to simulate the vessel drift and the wave motions of a platform in 1000 m (3,300ft) water depth was used to actuate the top of the pipe string. Tensions and bending moments were monitored by installing strain gauges along the pipe length.

The seabed consists of soft clay with undrained shear strength of 3 to 5 kPa, a sensitivity of 3, a plasticity index of 39 and a normally consolidated shear strength gradient below the mud layer. Table 2 shows the geotechnical parameters for seabed soil in detail.

Bridge et al. (2003) reviewed the results of full-scale riser test by 2H Offshore Engineering Ltd. The authors concluded based on the test data that the soil suction force, repeated loading, pull up velocity and the length of the consolidation time can affect the fluid, riser and soil interaction. The possible mechanisms for the trench creation were identified as follows:

- Up and down motions of the pipe driven by the actuator can form the trench. Water rushing out from beneath the riser can also scour out a trench.

- Additional scouring and washing away of the sediment around the riser may be

Table 2. Geotechnical Parameters of Clay at Watchet Harbor (Bridge and Willis, 2002)

Geotechnical Parameter	Value
Water Content (ω_c)	104.7 %
Bulk Density (ρ)	1.46 Mg/m^3
Dry Density (ρ_d)	0.73 Mg/m^3
Particle Density (ρ_s)	2.68 Mg/m^3
Liquid Limit (w_L)	87.6 %
Plastic Limit (w_P)	38.8 %
Plasticity Index (I_p)	48.9 %
Average Organic Content	3.2 %
Specific Gravity (G_s)	2.68
Undisturbed Shear Strength	3.5 kPa
Remoulded Shear Strength	1.7 kPa
Sensitivity of Clay	3.3
Coefficient of Consolidation (c_v)	0.5 m^2/yr
Coefficient of Volume Compressibility (m_v)	15 m^2/MN

caused by the flow of the tides.

- Vortex induced vibration (VIV) motions which were observed when the tide came in or went out are the result of the flow of the seawater across the riser. The high frequency vibration produces a sawing motion slowly cutting into the seabed.

- Buoyancy force causes the riser to lift away from the seabed when the riser is submerged. Loose sediment in the trench or attached to the riser would be washed away.

Bridge and Willis (2002) also conducted numerical modeling to calibrate the soil suction model of 2H Offshore Engineering Ltd. The upper bound curve (Fig. 12) based on the STRIDE 2D pipe and soil interaction analysis Willis and West (2001) was employed as the soil suction curve in the numerical modeling. The soil suction curve consists of three parts: suction mobilization, suction plateau and suction release as shown in Figure 12.

In addition, test measurements from strain gauge locations were compared to the simulations. Computed bending moments based on actual data were bracketed by simulation predictions accounting for suction and without suction. The results of this comparison show good agreement, as illustrated Figure 13. Further, differences in bending moments during pull up and lay down response were evaluated, considering the effects of soil suction. The results of these comparisons are as follows:

- A sudden vertical displacement of a catenary riser at its touchdown point (TDP) after a period at rest could cause a peak in the bending stress.

- Soil suction forces are subject to hysteresis effects.

- The soil suction force is related to the consolidation time.

- Pull up velocity does not strongly correlate with the bending moment response on a remolded seabed.

- Soil suction can cause effects such as a suction kick, oscillation moment response appeared to be due to a rapid release of soil suction when riser moves fast.

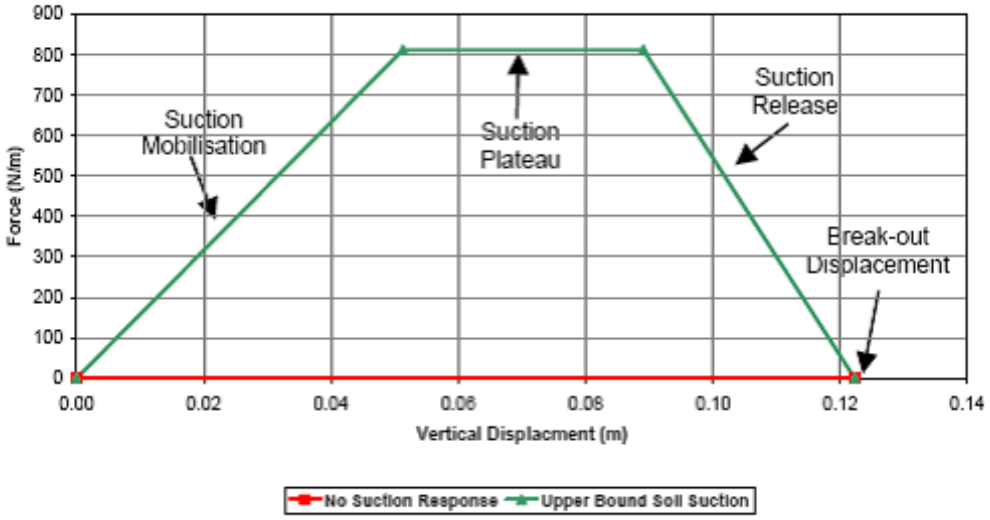

Fig. 12. Soil Suction Model (Bridge and Willis, 2002)

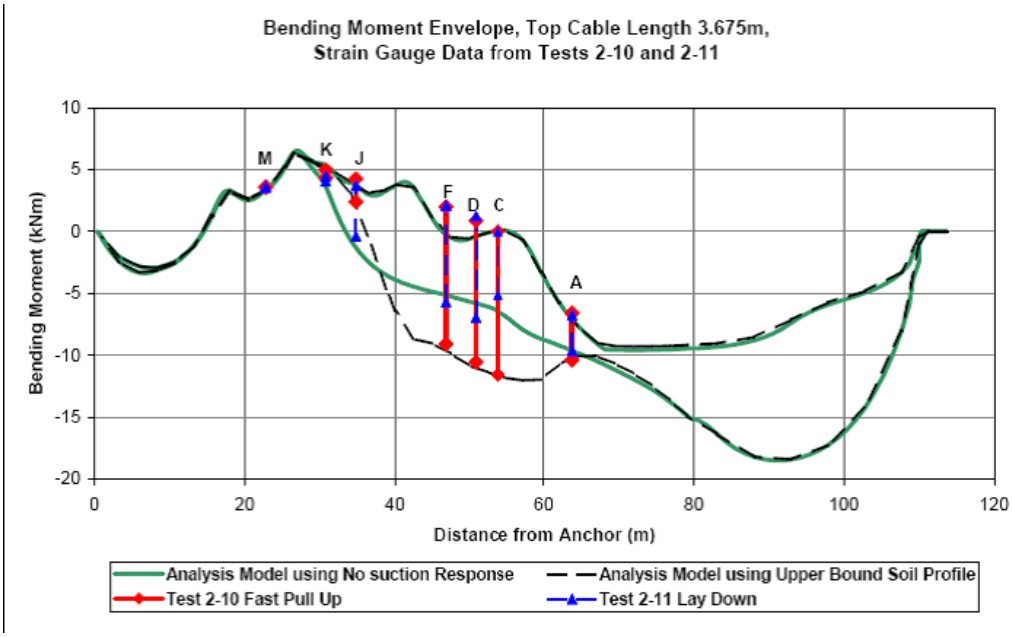

Fig. 13. Comparison of Test Data and Analytical Bending Moment Envelope (Bridge and Willis, 2002)

CHAPTER III

OBSERVATION FROM MODEL TESTS

3.1. Introduction

Model tests are the widespread method to measure soil stiffness when dealing with the SCR-seafloor interaction problem near the touchdown zone (Fig. 14). Previous model tests (Dunlap et al., 1990; Clukey et al., 2005) have shown the effects of the degradation in stiffness due to cyclic loading, as indicated by cyclic load tests of model pipes supported on soil. Figure 15 illustrates consecutive stages of typical soil-riser interaction behavior. Studies by Dunlap et al. (1990) and Bridge et al. (2004) indicate that appreciable soil suction may develop during uplift, although the maximum value of P in tension is significantly less than that in compression. At sufficiently large magnitudes of uplift motion, the pipe begins to separate from the seafloor, point (y_2, P_2). Model tests indicate that the breakaway is not abrupt; rather, the P-y curve gradually tends toward zero as depicted by path (y_2, P_2)-(y_3, P_3). With continued uplift the riser pipe is completely detached from the seafloor. Upon deflection reversal, the pipe again moves downward and eventually re-contacts the seafloor at point (y_3, P_3). After re-contacting, soil resistance mobilizes gradually as depicted by the S-shaped curve. However, re-contact soil strength generally is not larger than P_1 at y_1, as soil resistance declines with load cycles. Unloading-reloading reversals can occur from any point.

Recently, the Centre for Offshore Foundation Systems (COFS) and Norwegian Geotechnical Institute (NGI) conducted model test programs to evaluate cyclic degradation of soil stiffness and to investigate the trend of equivalent vertical stiffness under water cover (Aubeny et al., 2008; Langford and Aubeny, 2008). The major differences between the two test programs are the properties of soil and pipe as shown in Table 3.

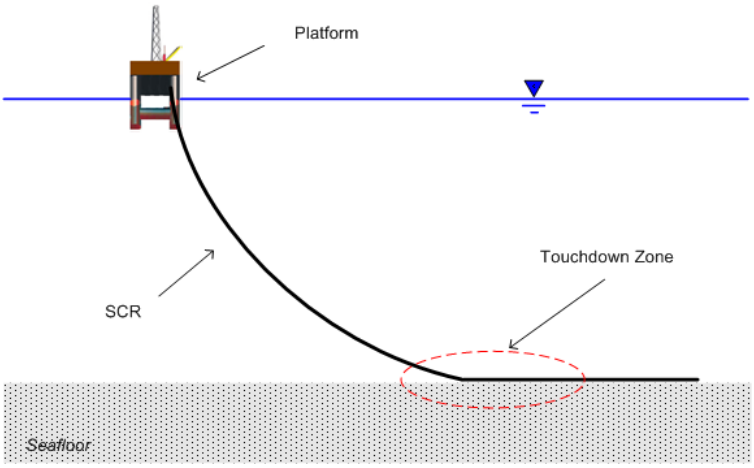

Fig. 14. SCR and Touchdown Zone

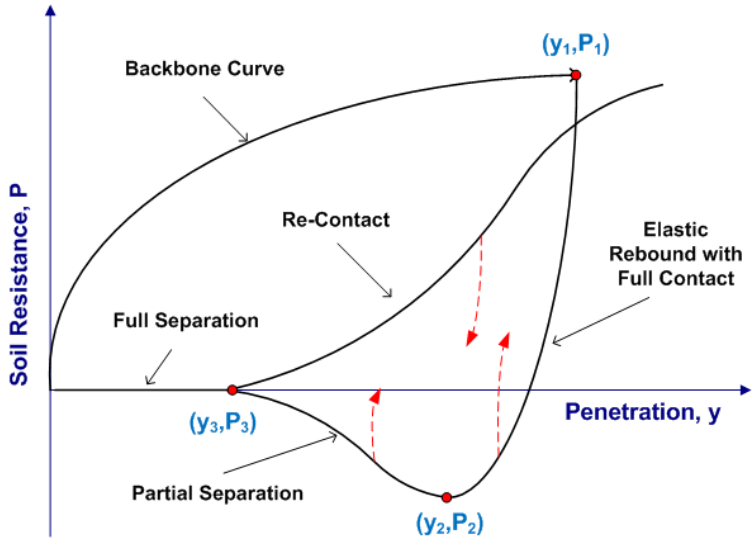

Fig. 15. Typical Soil-Riser Interaction Behavior

Table 3. Details for Model Tests

	COFS	NGI
Methods	TEST 3: Reference Test (0.1 mm/s) TEST 8: Small Amplitude Cyclic Test $\rightarrow$ Load-Controlled TEST 9: Large Amplitude Cyclic Test $\rightarrow$ Load-Controlled (0.1 mm/s)	TEST 1: Cyclic Penetration/Extraction (0.05 mm/s) TEST 2: Small-Cyclic Tests $\rightarrow$ Load-Controlled (0.05 mm/s) TEST 3: Small-Cyclic Tests $\rightarrow$ Displacement-Controlled (0.05 mm/sec) TEST 4: Cyclic penetration/Extraction (0.5 mm/s)
Test Bed Size	650 x 390 x 325 (220) mm	3600 x 1700 x (240) mm
Soil	Kaolin S_{uo} = 3.7 kPa (from 20 mm) S_g = -0.0029 kPa/mm	Marine Clay (LL=160, PI=100) S_{uo} = 2 kPa S_g = 13 kPa/m
T-bar	D = 5 mm L = 20 mm v = 1 mm/s N_{T-bar} = 10.5	D = 25 mm L = 120 mm v = 20 mm/s N_{T-bar} = 10.5
Pipe	D = 25 mm L = 125 mm	D = 174 mm (rough coated element) L = 1300 mm

While the model testing at COFS used kaolin (low plasticity soil) with an almost constant strength profile, the NGI program used re-constituted marine clay (high plasticity soil) with a linearly increasing strength profile. In addition, the model pipe of the COFS tests was 7 times smaller than the NGI pipe. This chapter presents in detail the observations and the findings from the two test programs.

3.2. Model Tests of the Centre for Offshore Foundation Systems (COFS)

Model tests were conducted to corroborate previous tests and to develop a P-y model similar to that used for laterally loaded piles, where P is net soil force per pipe unit length (F/L) and y is vertical deflection. A model pipe with diameter of 25 mm and length of 125 mm was tested on kaolin bed 220 mm deep in a test basin with internal dimensions of 650 mm by 390 mm by 325 mm deep. The actuator could be controlled electronically to allow displacement or force controlled loading.

The soil strength of kaolin was measured by T-bar (Stewart and Randolph. 1994) with dimensions of 5 mm in diameter by 20 mm in length. T-bar factor was 10.5 for a penetration rate of 1 mm/sec. Figure 3 shows a soil strength profile to a depth of 170 mm. To the exclusion of the top 20 mm due to free surface effects, the linear regression analysis draws a strength intercept of 3.7 kPa with a strength gradient of -0.0029 kPa/mm (Fig.16). Although the slightly negative strength gradient results from a likely consequence of incomplete consolidation in the test bed, it may safely be assumed that soil strength is constant.

The test program consists of three tests: a reference test and two cyclic loading tests. The reference test was conducted to establish the backbone curve and stiffness relationships to be used as a basis for evaluating cyclic test data. A small amplitude cyclic loading test was performed under sufficiently small magnitude load such that no reversal of direction occurs in the net soil force acting on the pipe. Finally, a large amplitude cyclic loading test was carried out, in which the pipe undergoes a large (1D) upward displacement during each load cycle and a reversal of the net soil force on the pipe occurs.

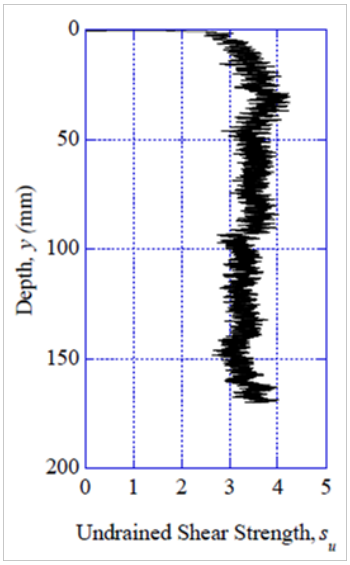

Fig. 16. Soil Strength Profile

3.2.1. Reference Test

The reference test was conducted to investigate the ultimate boundaries in both soil resistance and breakout force for a vertically penetrated and uplifted pipe. Figure 17 shows the P-y relationship in the reference test. After the model pipe was embedded to 21 mm (0.8D), reloads were applied at depths 72 mm ($\sim$2.8D) and 122 mm ($\sim$6D). During the test, the penetration rate was 0.1 mm/sec to keep undrained conditions. While the model pipe in the first unload was uplifted until it detached from the soil, full separation did not occur in the second unload. This explains the difference in curve shape between the first and second reload. As penetration depth increases, soil resistance gets larger along with breakout force. The ratio of soil resistance over breakout force for each cycle load is 0.55, 0.75, and 0.8, respectively.

Figure 18 presents the dimensionless from of load-displacement curve in Figure 17. Load was normalized by the product of soil strength (S_u), pipe diameter (D), and pipe

length (L) and displacement also was non-dimensionalized by pipe diameter. The bearing factor predictions by FE simulation for penetrating pipe in a trench having a width equal to the pipe diameter (Aubeny et al., 2005) is shown in figure 18:

$$N_p = a(y/D)^b \tag{3.1}$$

where the coefficients a and b vary according to pipe surface roughness, soil profile, and penetration depth. Although coefficients for a rough pipe are a=6.73 and b=0.29, the back-bone curve presented herein used a=6.4 and b=0.23 for better fitting. The match between the predictions and the measurements seems to be reasonable, although the FE calculations were based on a somewhat simplistic analysis.

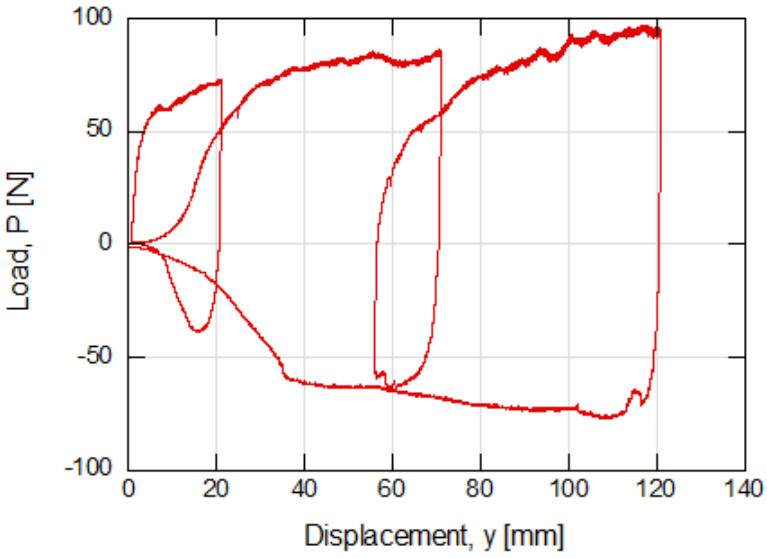

Fig. 17. Measured Load vs. Displacement in Reference Test

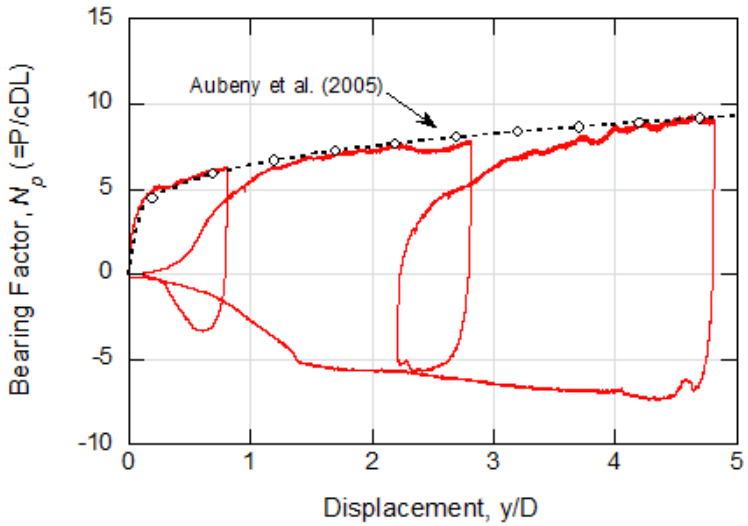

Fig. 18. Normalized Force vs. Penetration in Reference Test

a. Unload-Reload Stiffness

Previous works (Bridge et al., 2004; Clukey et al., 2008) stated that most of SCR analyses codes adapt either a rigid or a linear-elastic model to simulate the soil-riser interaction since it was preferred by designers. Hence, soil response is most often expressed by a value of soil stiffness. Their paper focuses on soil stiffness variation with either load cycles or displacement from reversal points. Secant stiffness (k_{sec}) can be defined as the slope between current point and past reversal point on P-y curve.

$$k_{sec} = |P - P_{rev}|/|y - y_{rev}| \tag{3.2}$$

where P_{rev} $[F/L]$ is the load corresponding to the reversal point and y_{rev} $[L]$ is the penetration depth corresponding to the reversal point. The secant modulus is often used in its non-dimension form:

$$K = k_{sec}D/P_1 \tag{3.3}$$

where P_1, force per unit length of pipe, refers to the point on the compression backbone curve corresponding to the initial load reversal. The scaling by P_1 provides a simple basis for estimating secant stiffness for different levels of pipe penetration provided that the pipe is not uplifted beyond the suction limit.

Figure 19 presents dimensionless secant stiffness versus displacement from reversal point for all cycles. The trend of the normalized secant stiffness in unloading shows a similar K-$\Delta y/D$ relationship in the range of $\Delta y/D$ ¡ 0.25. Whereas the reload secant stiffness is about 40-45% less than unload stiffness at a given level of displacement from the point of reversal. Accordingly, the reload curve is a somewhat softened reflection of the unload curve. Unlike the other curves, the first reload curve in this figure shows a unique shape caused by the full detachment between pipe and soil.

Previous researchers (Bridge et al., 2004) have proposed a hyperbolic model to characterize P-y data resulting in a normalized secant stiffness K.

$$K = \frac{fK_{max}}{f + K_{max}\Delta y/D} \tag{3.4}$$

where K_{max} and f are fitting parameters. The hyperbolic model (Eq. 3.5) with K_{max} = 250 and f = 1.55 shows good agreement with the measured data under unloading conditions (no soil-pipe separation) for the entire range of displacements in the following unload stages excluding $\Delta y/D > 0.25$ in the first unload stage.

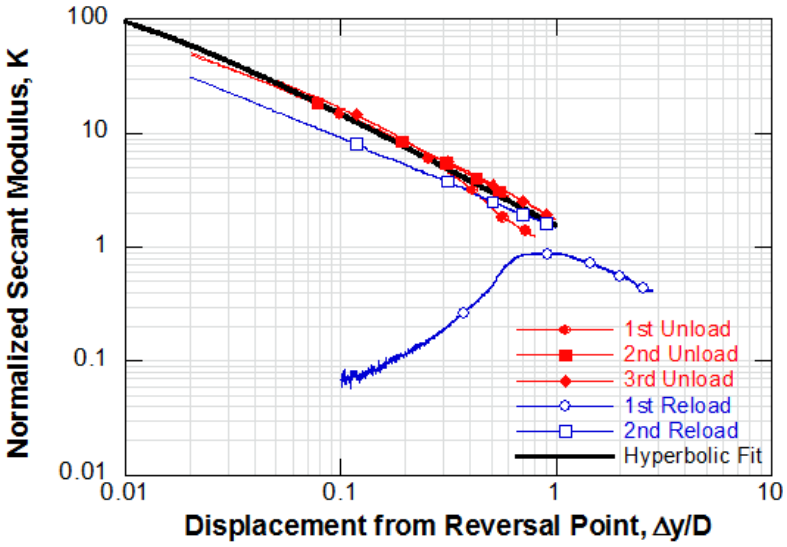

Fig. 19. Secant Modulus Measured in Reference Test

3.2.2. Force Controlled Small Amplitude Cyclic Tests

The small amplitude cyclic test program (Table 4), in which the reversal load is larger than zero, consists of the following stages: initial penetration, the first cyclic loading sequence, re-penetration, the second cyclic loading sequence, and extraction. Figure 20 indicates the entire stages in small amplitude cyclic test. In the initial stage, the model pipe was embedded to 48 mm ($\sim$2D) with displacement rate of 0.1 mm/sec resulting load of 68 N in a maximum. Next, the first cyclic loading sequence with three different force ranges (ΔP=20 N, 40 N, and 60 N) was applied with load frequency of 0.2 Hz. After re-penetration to 110 mm ($\sim$4.5D), at which the load was 88 N, the same cyclic force amplitudes used in the first cyclic loading sequence were applied to the model pipe.

Table 4. Details for Small Amplitude Cyclic Test (Test 8)

Stage	Description	Details
A	Initial penetration to 2D	0.1 mm/s
B	Cyclic loading	10 cycles +68/+48 N at 0.2 Hz
C	Cyclic loading	10 cycles +68/+28 N at 0.2 Hz
D	Cyclic loading	100 cycles +68/+8 N at 0.2 Hz
E	Penetration to 4.5D	0.1 mm/s
F	Cyclic loading	10 cycles +88/+68 N at 0.2 Hz
G	Cyclic loading	10 cycles +88/+48 N at 0.2 Hz
H	Cyclic loading	65 cycles +88/+28 N at 0.2 Hz
I	Extraction	0.1 mm/s

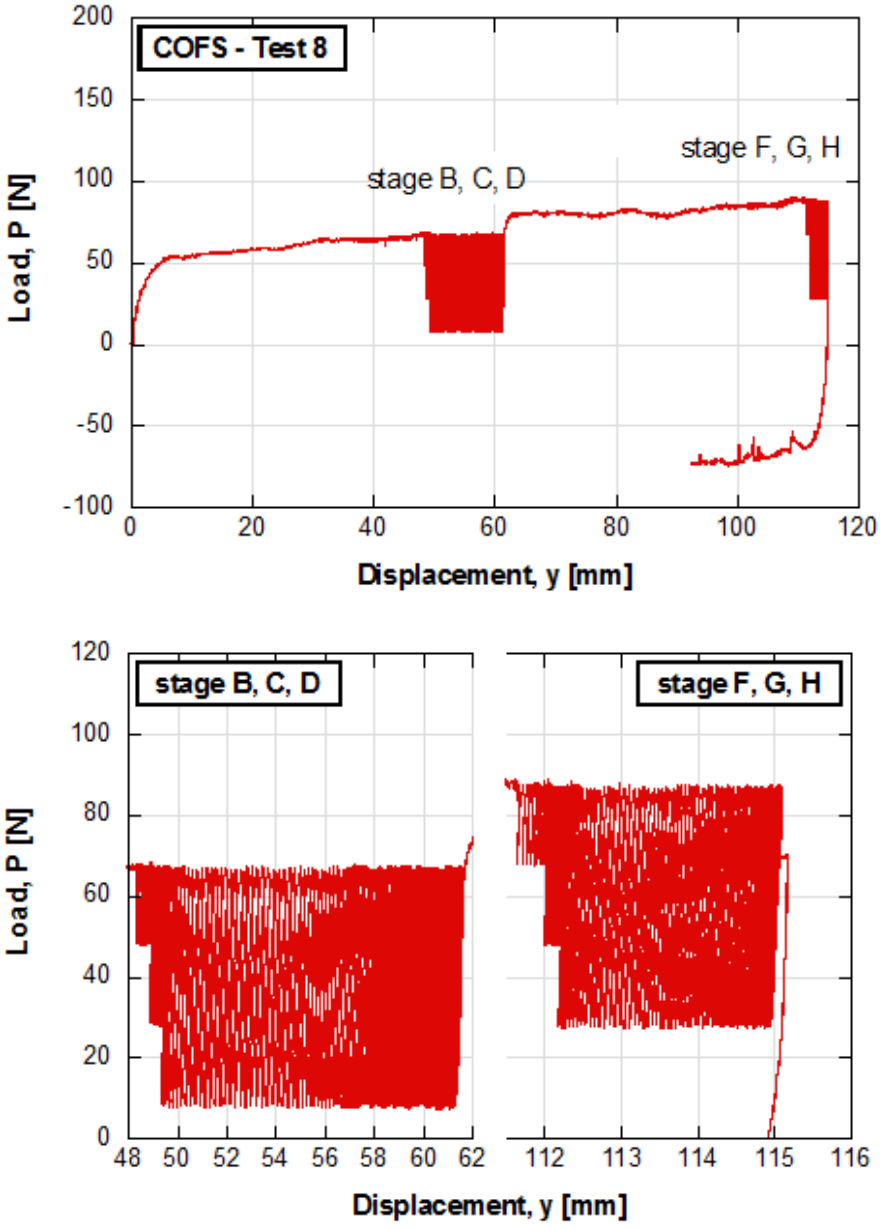

Fig. 20. Load-Displacement in Small Amplitude Cyclic Test

a. Stiffness Variation

Figure 21 shows the relationship between normalized secant stiffness (K) and displacement from reversal point for the stage D (ΔP_{cyc}=60N) and secant modulus variation at displacement Δy/D=0.005 with increasing load cycles. Unload stiffness is also larger than reload stiffness, in this case by a factor of about 50-100% in the range except for small displacement (Δy/D$<$0.001). The data shows a general tendency of stiffness reduction with increasing load cycles. Figure 21 (b) more clearly presents the stiffness degradation effect. Both unload and reload stiffnesses degrade with load cycles at a rate 0.16% per cycle for the unload stiffness and 0.07% per cycle for the reload stiffness. The secant stiffness variation for stage H shows a similar trend as in the stage D (Figure 22); however, soil resistance (stage D) is larger by a factor of about 50%.

Figure 23 shows the variation of normalized secant modulus at the reversal points for each cycle with increasing number of cycles for both unload and reload cases. In these figures, the unload stiffness is much larger than reload stiffness. The difference between unload-reload stiffness at stage B and F is about 300%. It may be said that the larger stiffness degrading occurs in the smaller amplitude cyclic load. The soil stiffness at deeper point (ΔP=20 N) also is greater in both cases of unloading and reloading by a factor of about 100%. Indeed, it seems that the secant stiffness in stage D and H is mostly constant. Thus, the equivalent secant moduli (K) for unload and reload are 120 and 100 at stage D and 65 and 50 at stage H.

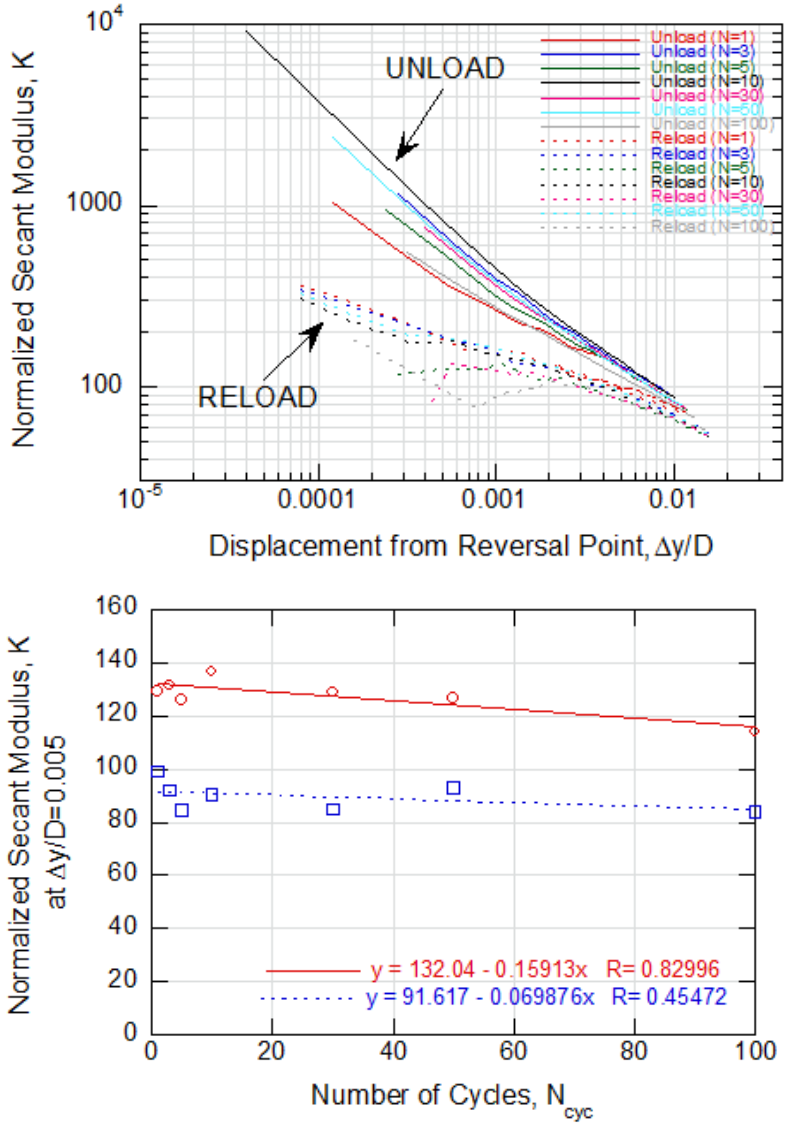

Fig. 21. Secant Stiffness from Stage D in Small Amplitude Test (COFS-Test8)

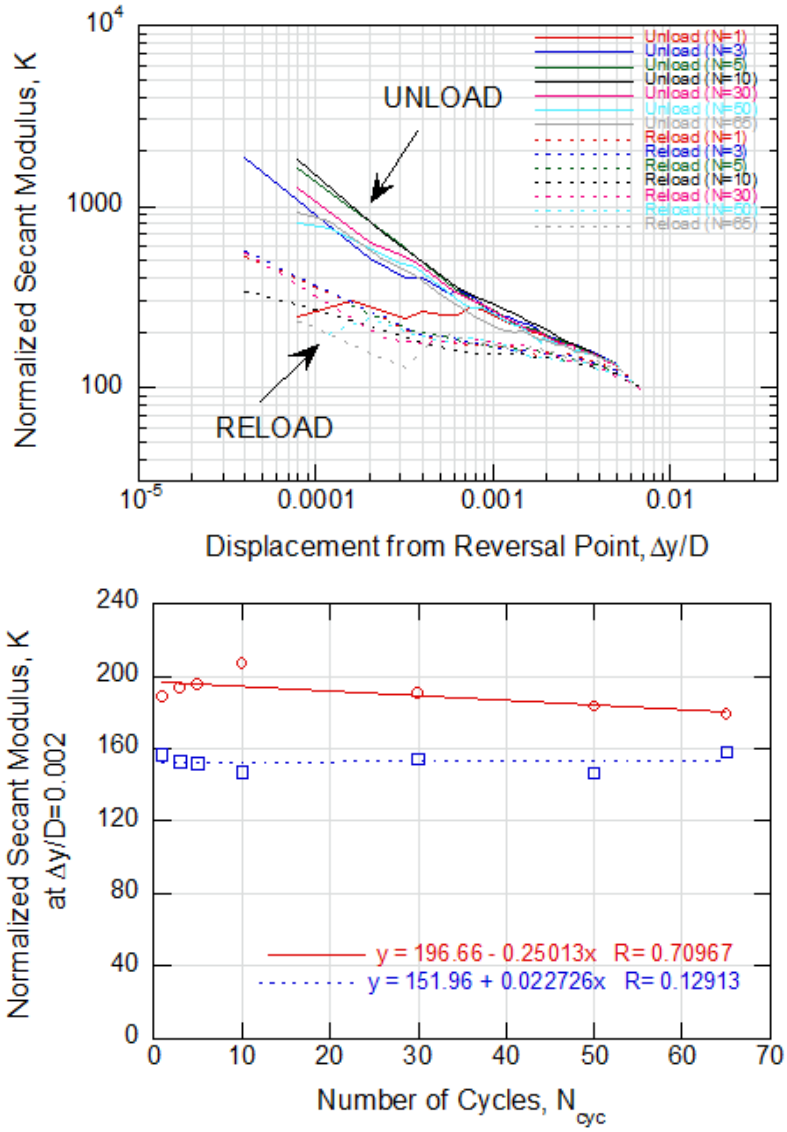

Fig. 22. Secant Stiffness from Stage H in Small Amplitude Test (COFS-Test8)

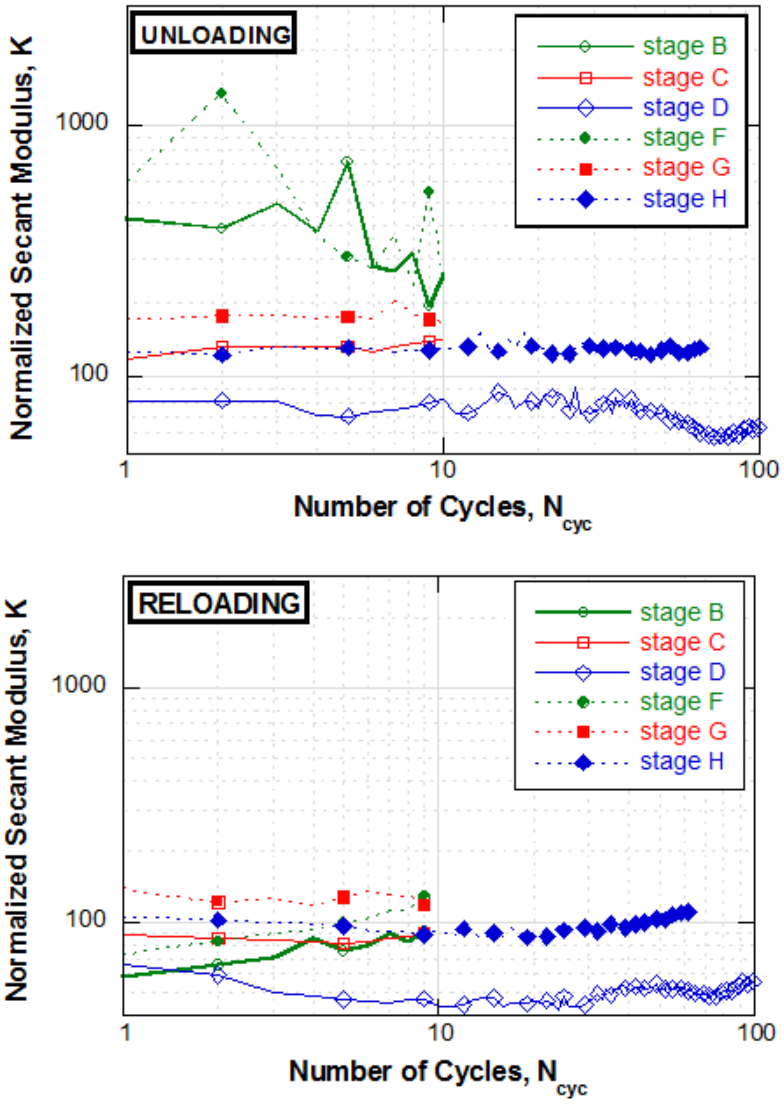

Fig. 23. Normalized Secant Modulus from Small Amplitude Cyclic Test (COFS)

b. Permanent Displacements

Figure 24 shows the accumulated vertical displacements at the end of each load cycle. When comparing stage D and H, the permanent displacement in stage D is much larger than the one in stage H. Previous cyclic loads (stage D) applied at relatively shallow depth (low soil strength) result in more penetration depth by a factor up to 370% within the cycles performed. In particular, normalized permanent displacement increases with same rate after 20 cycles. The two trend lines for stage D and H can be described my following equation:

$$\Delta y/D = a \log N_c - b \tag{3.5}$$

The fitting parameters a and b for stage D and stage H are 0.48 and 0.13, respectively. Figure 25 indicates the difference between reversal displacements for each cycle. In this test, the loop width variation is generally constant excluding stage D in which the soil strength seems to be more affected by cyclic loads although the number of tests is insufficient. The width variation during the second load sequence is smaller than the one during the first load sequence by a factor of about 50% due to higher soil strength.

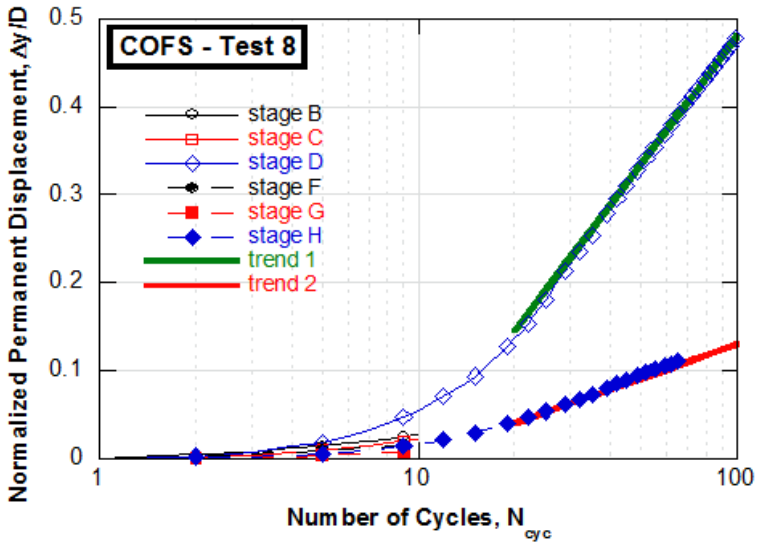

Fig. 24. Permanent Displacement from Small Amplitude Test (COFS-Test8)

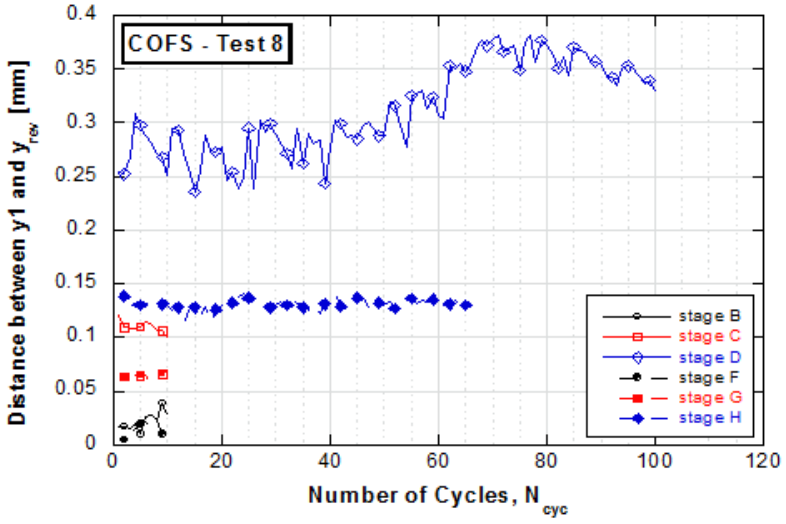

Fig. 25. Variation of Displacement Range

Table 5. Details for Large Amplitude Cyclic Loading Test (Test 9)

Stage	Description	Details
A	Initial penetration to 2D	0.1 mm/s
B	Cyclic loading	30 cycles +60/-40 N at 0.002 Hz
C	Penetration to 4.5D / Extraction	0.1 mm/s

3.2.3. Force Controlled Large Amplitude Cyclic Tests

Unlike the small amplitude test, this test applied a lager magnitude of cyclic load to ensure a reversal of direction in the soil response P acting on the pipe (Table 5). Figure 26 shows the force-displacement curve for the entire sequence in the large amplitude test. The model pipe was penetrated monotonically to a depth 51 mm ($\sim$2.0D), at which a soil resistance of 78 N developed. The pipe was then uplifted 26 mm ($\sim$1.0D) and re-penetrated into the soil until the soil resistance reached to 65 N. After this sequence was repeated 30 times in stage B, the pipe was again monotonically embedded to 141 mm and then extracted. All of stages were conducted at a displacement rate of 0.1 mm/s and the frequency of the cyclic loading was 0.002 Hz.

a. Stiffness Variation

Figure 27 shows the dependency of unload-reload stiffness on displacement from the reversal point for the first and the last cycles. Reload stiffness was initially about 25% of unload stiffness, while reload stiffness reached to approximately 80% of unload stiffness in the last cycle. In contrast to what was observed for the small amplitude loading (Fig. 23), the data show a general trend of increasing stiffness with increasing number of load cycles.

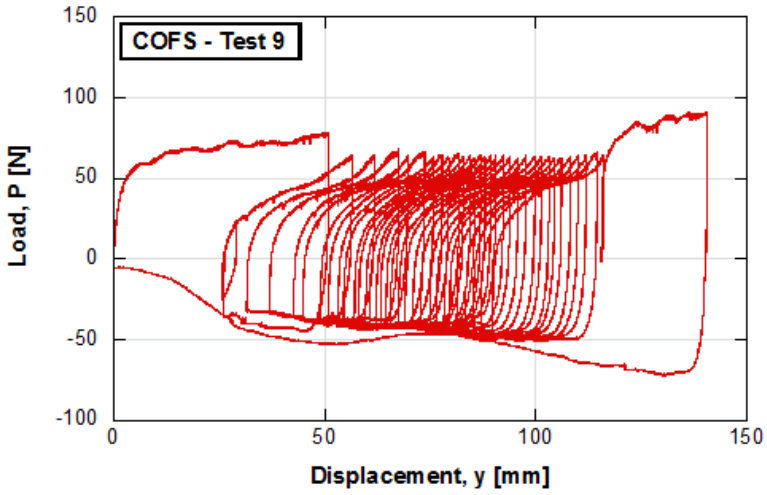

Fig. 26. Load-Displacement in Large Cycle Penetration Test

A possible explanation for this conflict is the differences in the time durations of the small and large amplitude tests. The duration of the small amplitude cyclic loading sequence was 10 minutes, while that of the large amplitude loading sequence was 271 minutes. It seems that the long duration of the latter test was probably sufficient for significant dissipation of excess pore pressures to occur. Hence, the effects of reconsolidation appear to have offset those of soil remolding. Figure 28 presents the variation of unload-reload stiffness at reversal points as cyclic loading progresses. Although unload stiffness is 5∼20% larger than reload one, both of unload-reload stiffness increase as load cycle increases by the reason mentioned before.

b. Permanent Displacements

Figure 29 shows permanent penetration depth in large amplitude cyclic test. Permanent displacements in the large amplitude test are much larger than those in the small amplitude test. The accumulated displacements in both tests follow a similar pattern in that they

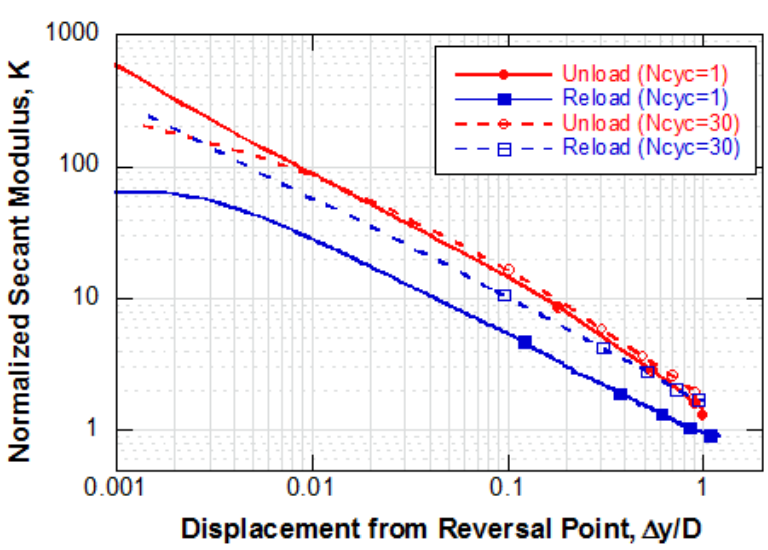

Fig. 27. Secant Modulus Variation from Large Cycle Penetration Test (COFS-Test9)

increase rapidly under the initial 20 cycles and then grow gradually. It appears likely to show the trend of Eq. 3.5 for the range of N_{cyc} ¿ 20 (a=4.5 and b=4.0) though the number of load cycles is not enough to make a clear determination.

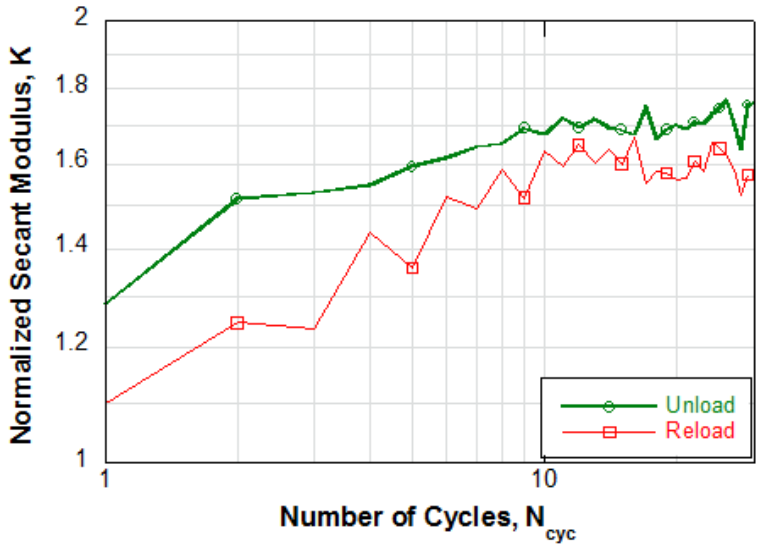

Fig. 28. Secant Modulus Variation at Reversal Points from Large Amplitude Cyclic Test (COFS-Test9)

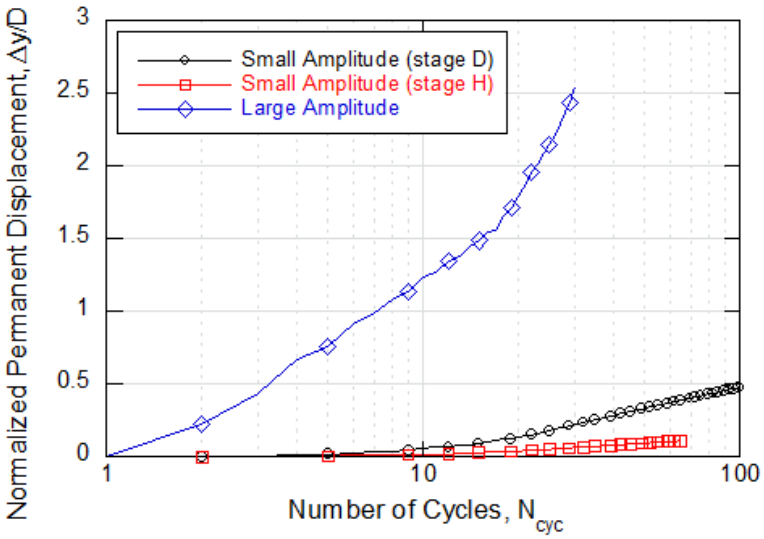

Fig. 29. Permanent Vertical Displacements from Large Amplitude Test (COFS)

3.3. Model Tests at the Norwegian Geotechnical Institute (NGI)

The tests performed at NGI were large-scale physical model tests to investigate seafloor-riser interaction in touchdown area. Unlike previous model tests, these tests were carried out in re-constituted high plastic marine clay, since the characteristics of cyclic behavior depend on plasticity index and overconsolidation ratio (Andersen, 2004). Four tests were arranged within a test bed of dimensions 3.6 x 1.7 m (Figure 30). Figure 31 shows a hydraulically-powered biaxial test system used for the tests. In this system, the vertical actuator had 1000 mm in the maximum test stroke. The model pipe was a roughly coated element with length of 1300 mm and diameter of 174 mm.

The marine clay was obtained from offshore using a box corer and transported to Norway in bags. The natural water content was around 150%, but water content reached 340% after water was to the clay for improvement of workability. The clay was consolidated by using dead weights and vacuum applied within a rubber membrane. Finally, the consolidation stress reached 9.5 kPa. After consolidation and a 1 month swelling period, the final height of the clay for testing was just 240 mm from the bottom of the test bed. Figure show soil strength profile measured at points (Figure 30) by mini T-bar tests with 25 mm in diameter and 120 mm in length. All T-bar test probes kept a constant penetration rate of 20 mm/sec (N=10.5). From the plotted data, the soil profile was defined increasing from 2 kPa at the seabed with a strength gradient of 13 kPa/m. However, it should be noticed that the T-bar factor change with depth has uncertainties; thus, the shear strength at the surface may be somewhat underestimated.

Tests 1 and 4 were single-stage cyclic tests used to investigate the effect of penetration rate on bounding curves for penetration and uplift, while tests 2 and 3 were multi-stage cyclic tests where each stage featured a different specified load or displacement sequence including time delay between the stages after initial embedment to 0.3D in depth. These

multi-stage small cyclic tests were used to investigate the variation of unload-reload stiffness within the bounding curve. The key information is in Table 6.

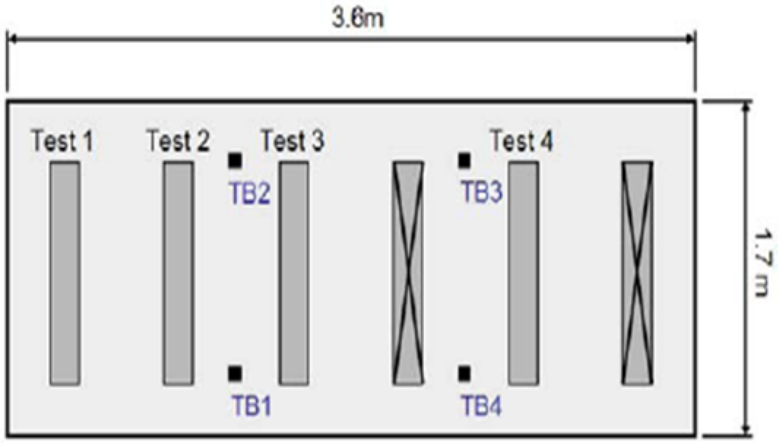

Fig. 30. Test Arrangement in Plan View (Langford and Aubeny, 2008)

Table 6. Summary of Test Programs (Langford and Aubeny, 2008)

Test	Control Method	Penetration Velocity	Description	Cyclic Stages
1	Displacement	0.05 mm/s	Cyclic penetration/extraction	1
2	Load	0.05 mm/s	Small-cyclic loading	6
3	Displacement	0.05 mm/s	Small-cyclic loading	13
4	Displacement	0.50 mm/s	Cyclic penetration/extraction	1

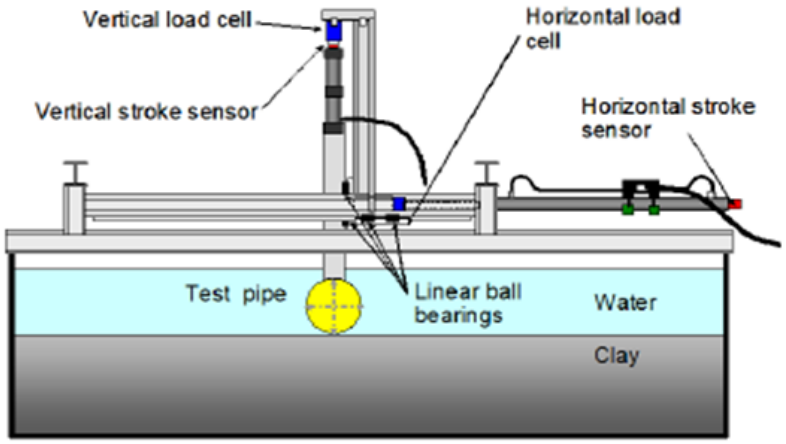

Fig. 31. NGI Test Bin and Instrumentation (Langford and Aubeny, 2008)

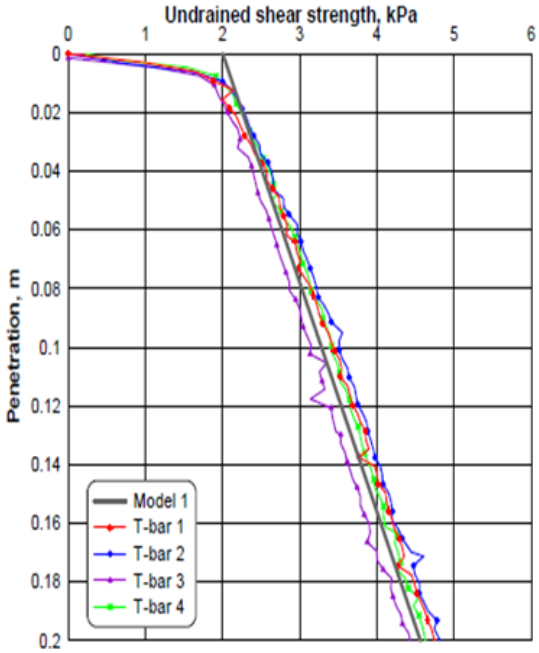

Fig. 32. Soil Strength Profile (NGI) (Langford and Aubeny, 2008)

3.3.1. Penetration Test

a. Penetration Rate Effect

Figure 33 shows soil resistance versus penetration depth for large cyclic penetration tests (Test 1 and 4). The pipe was initially penetrated to a depth of 52 mm ($\sim$0.3D) at a constant rate of displacement. The first test was penetrated at 0.05 mm/s, whereas fourth test was penetrated at a faster rate of 0.5 mm/s. The soil resistance developed in Test 4 was consequently about 20% higher than that in Test 1. In each cycle of the tests, the pipe was penetrated to a constant level of soil resistance about 9.5 kPa in Test 1 and 11 kPa in Test 4, and the pipe then was lifted to the point of full soil-pipe separation in order to obtain a complete picture of the suction plateau.

Figure 33 also includes the effect of penetration rate on compression resistance on the order of 15 to 20 % and the maximum breakout force was much more sensitive to displacement rate. The peak mobilized breakout force for Test 4 (conducted at the higher rate) was generally over twice that for Test 1. The width of the suction area (ΔP <0) was also much wider in the test conducted at the higher displacement rate. Indeed, bearing factor on penetration depth declines under same magnitude of cyclic load.

b. Unload-Reload Stiffness

Figure 34 and 35 show dimensionless secant stiffness on displacements from reversal point for test 1 and 4, respectively. The unload stiffness in both tests shows a remarkable insensitivity to load cycle and penetration rate. Besides, the unload stiffness follows well the hyperbolic relationship (Eq. 3.5) with the same fitting parameters, K=250 and f=1.55. For reload stiffness, the same trend appears because of complete separation between clay and model pipe.

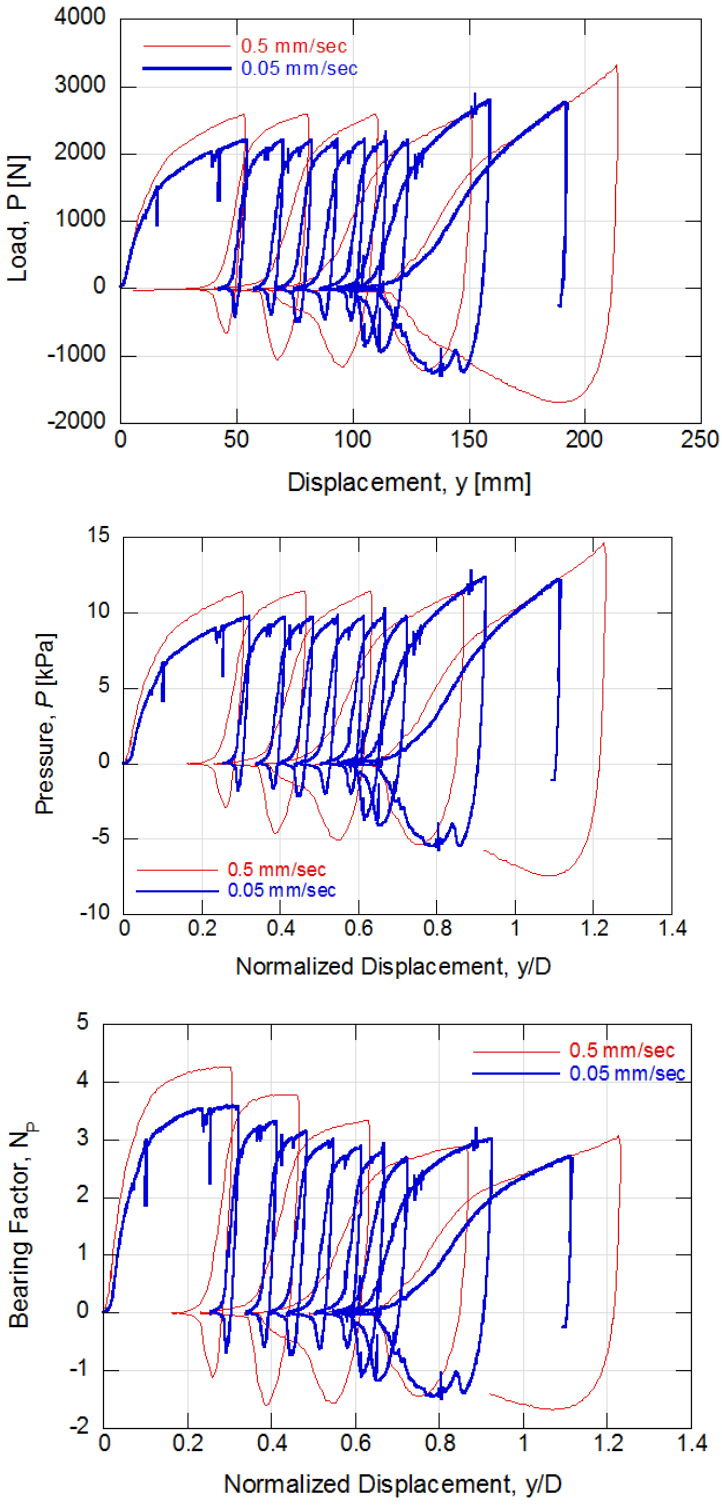

Fig. 33. Soil Resistance vs. Penetration (Tests 1 & 4)

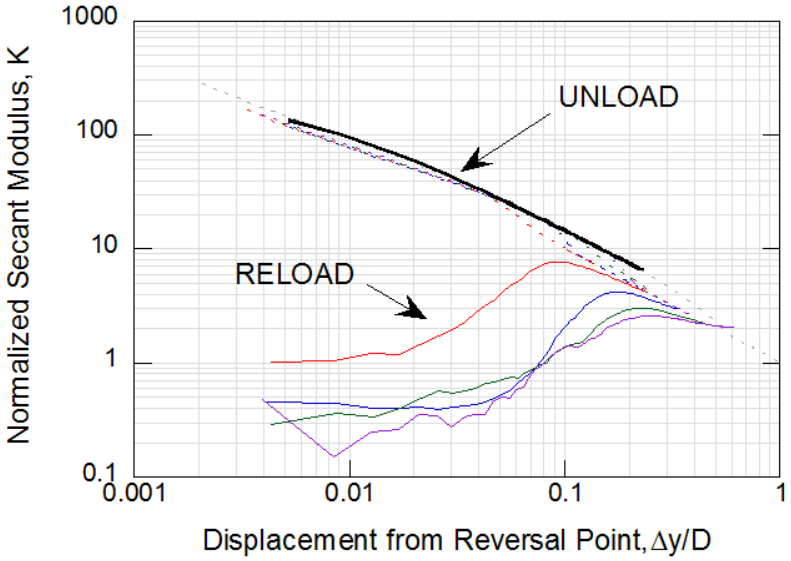

Fig. 34. Secant Stiffness from Test 1 (0.05 mm/sec)

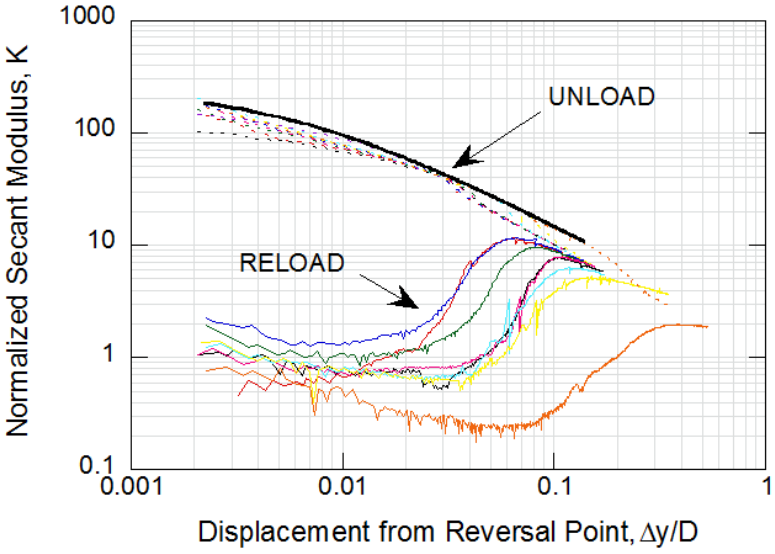

Fig. 35. Secant Stiffness from Test 4 (0.5 mm/sec)

3.3.2. Force Controlled Cyclic Tests

A force controlled test (Test 2) investigated penetration behavior of the riser under varying cyclic loads at frequency of 0.005 Hz and 0.05 Hz. This test applied a sequence of cyclic loads in which load reversal occurred in the soil resistance P acting on the pipe, but the reversal point did not reach the maximum breakout force (P_2 in Figure 15). Figure 36 shows the entire load-displacement plots related to Test 2. On the first day, the pipe was penetrated monotonically to 55mm ($\sim$0.3D) at rate of 0.05 mm/s, at which soil resistance developed to 2000 N. Thirty cycles were then applied with a cyclic load of ΔP=2200 N. After a 72 hours pause, the loading sequence was applied at a frequency of 0.005 Hz in order to evaluate the effect of consolidation (or thixotropy) and frequency. Next, a short series of cyclic loads was applied at more embedded depth (0.8D). The detail information is in Table 7.

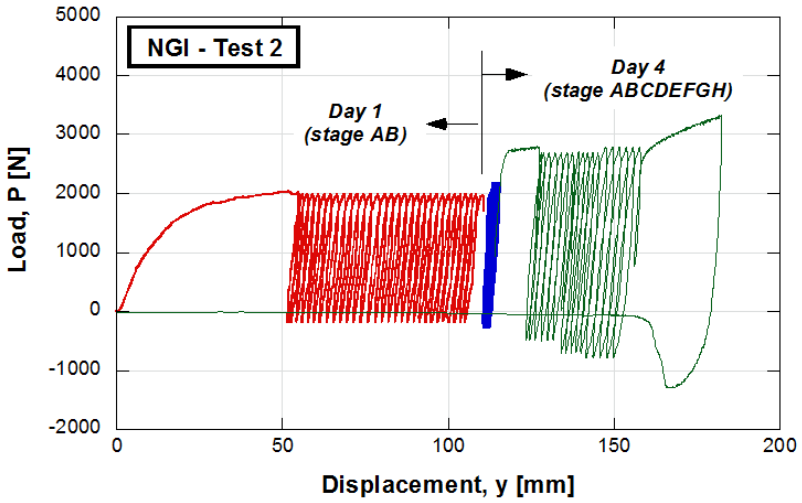

Fig. 36. Load-Displacement from Force Controlled Test (NGI-Test 2)

Table 7. Details for Small Amplitude Cyclic Test

Test Day	Stage	Description (Time)	Details
1	A	Initial penetration to 0.3D	0.05 mm/s
	B	Cyclic loading (102 min)	30 cycles +2000/-200 N at 0.05 Hz
4	A	Hold 72 hours	Stroke held constant
	B	Cyclic loading (1600 min)	50 cycles +1900/-200 N at 0.005 Hz
	C	Cyclic loading (1660 min)	50 cycles +2200/-300 N at 0.005 Hz
	D	Penetration to 0.8D	0.05 mm/s
	E	Cyclic loading (25 min)	6 cycles +2700/-500 N at 0.005 Hz
	F	Cyclic loading (21 min)	5 cycles +2700/-700 N at 0.005 Hz
	G	Cyclic loading (21 min)	5 cycles +2800/-800 N at 0.005 Hz
	H	Penetration to 1D	0.05 mm/s
	I	Extraction	0.05 mm/s

a. Permanent Displacements

Figure 37 shows the hysteresis loops for the first and the last cycle of the load-displacement plot. For easy comparison of stage B (0.05 Hz) from day 1 and stage B (0.005 Hz) from day 4, in which similar cyclic loading was applied, the center of two loops has been shifted on the y axis. All hysteresis loops look like a convex lens in shape. The loops of stage B (day 1) are the thicker and wider than those of stage B (day 4). In addition, there is no stiffness difference between the two loops in stage B (day 1), unlike those in stage B (day 4) in which the final cycle is rotated clockwise. These shape difference in two stages are related with the increased soil strength by combination effect of load frequency and consolidation caused by the long rest period (72 hrs) between the two stages. Figure 38 indicates the variation of cyclic loop width for each cycle. The higher amplitude load results in more rotated hysteresis loop excluding stage B and C on day 4 which show clearly cyclic reduction in soil strength under same magnitude of load.

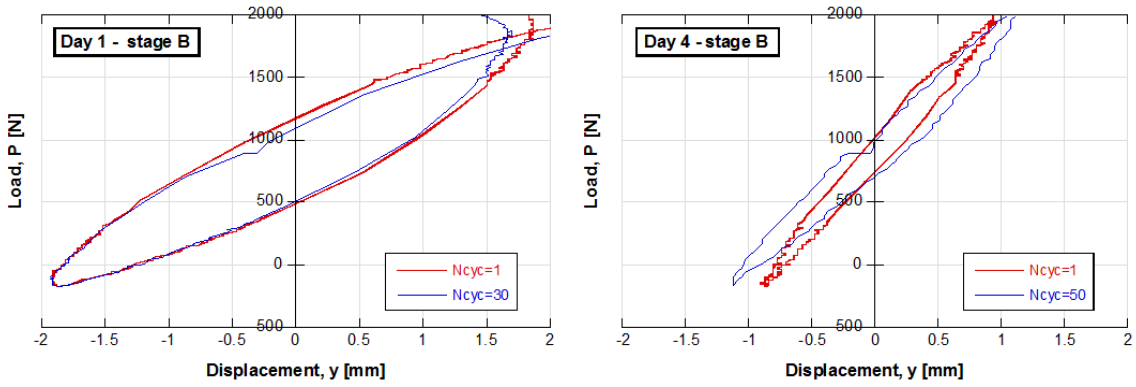

Fig. 37. Hysteresis Loop for the First and the Last Cycle in Stages of Day1-B (0.05Hz) and Day4-B (0.005 Hz)

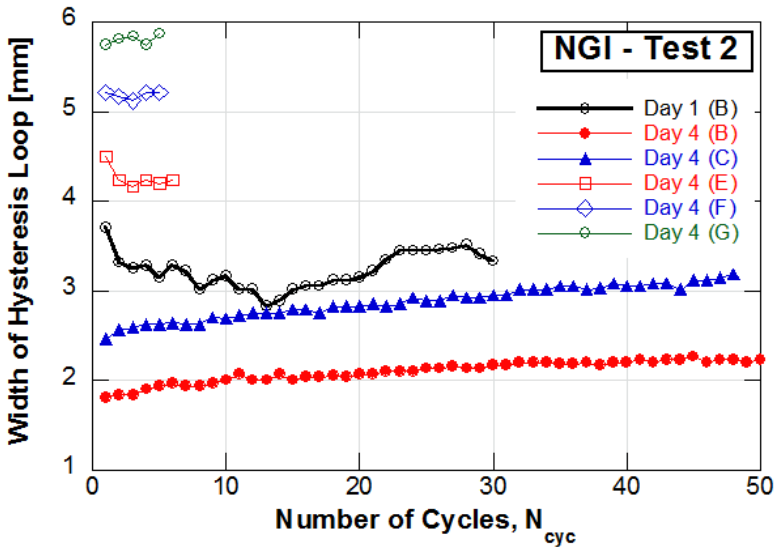

Fig. 38. Width Variation of Hysteresis Loop on Load Cycle in Force Controlled Test (NGI-Test2)

Figure 39 presents the permanent displacement relative to the start of each stage with increasing number of load cycles. The permanent penetration for stage B (day 1), D, E, and F are values of similar level, whereas those for stages B and C (day 4) exhibit much lower levels. This suggests that the effect of a very long pause causes the soil to become significantly stiffer and low load frequency also results in less penetration depth. In contrast, the larger magnitude cyclic load results in more penetration; however, influence of load magnitude seems to be relatively smaller than the effect of consolidation or load frequency.

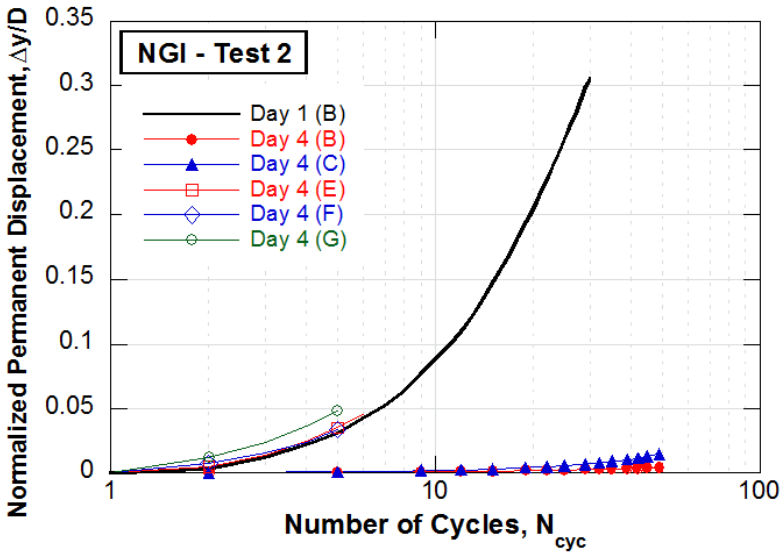

Fig. 39. Normalized Permanent Displacement vs. Number of Cycles

b. Stiffness Variation

Figure 40 shows the variation of secant modulus at reversal points. As load cycles increase, both the unload and reload secant stiffnesses (k_{sec}) decline. While a large reduction in soil stiffness occurs in stage B and C on day 4, k_{sec} in other stages decreases gradually. Large amplitude cyclic loads also lead to higher secant modulus. Unlike stage B and C on day 4, the unload secant modulus is larger than the reload secant modulus by a factor of about 30∼40%.

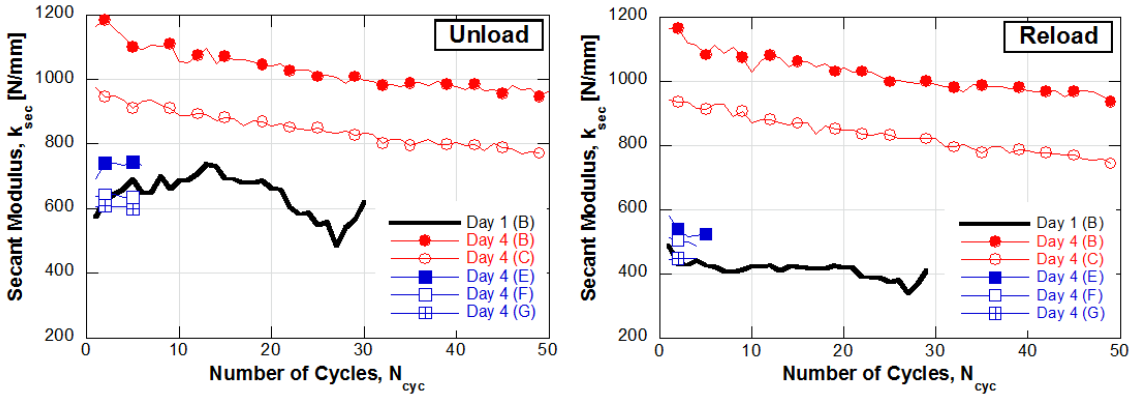

Fig. 40. Secant Modulus vs. Number of Cycles

Figure 41 presents the change of secant stiffness with displacement from reversal point for stage B on day 1 and stage B on day 4. Cyclic loads of similar amplitude are applied in two stages, but stiffness variation show different trends because of the rest times and different frequencies. While the secant stiffness in stage B (day 1) is larger than that in stage B (day 4) in the range of $\Delta y/D < 0.005$, the stiffness in stage B (day 1) rapidly declines when $\Delta y/D > 0.005$; finally, the modulus in stage B (day 4) is larger. The reload stiffness in stage B (day 1) is approximately 65% of the reload stiffness in stage B (day

4). Figure 42 and 43 show the modulus variation for various amplitudes of cyclic loading, following the general trend that large amplitude load results in higher modulus.

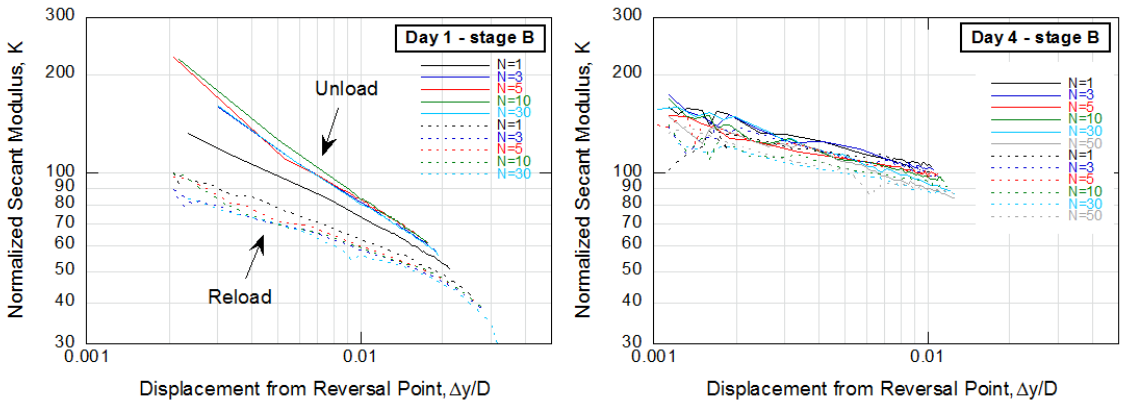

Fig. 41. Secant Modulus Comparison between Day 1 - Stage B (0.05 Hz) and Day 4 - Stage B (0.005 Hz)

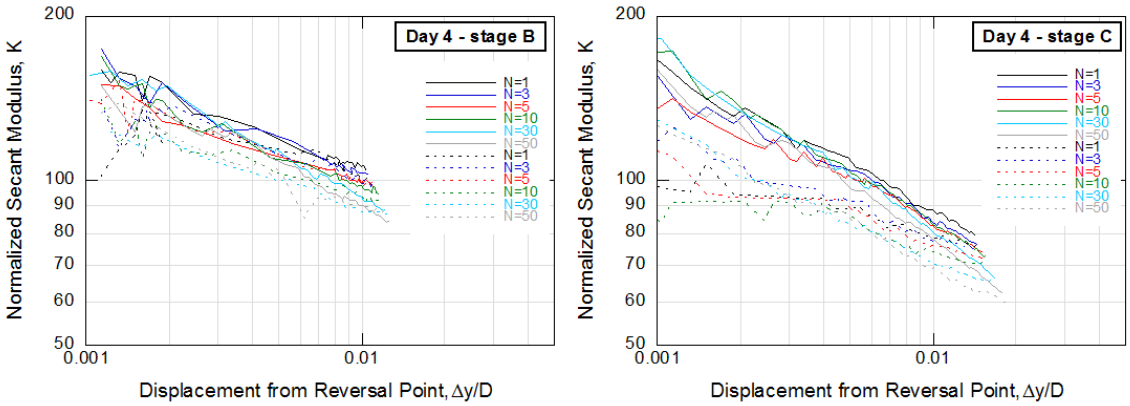

Fig. 42. Secant Modulus Comparison between Stage B and C on Day 4

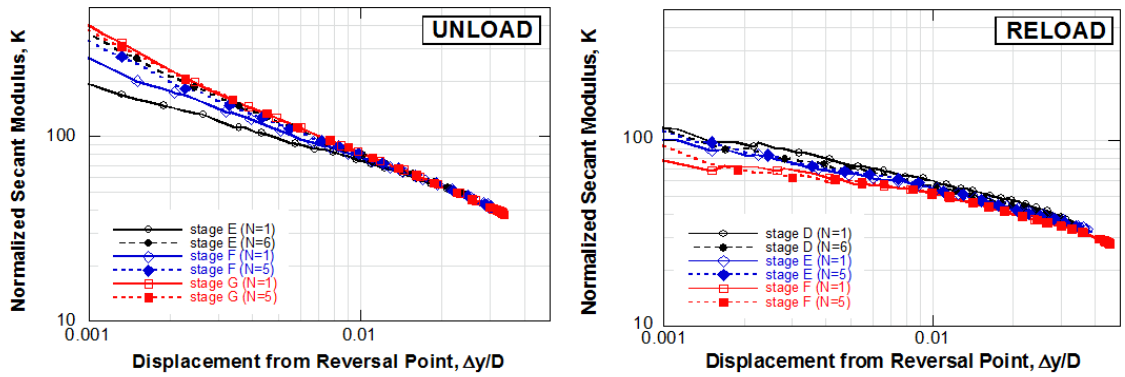

Fig. 43. Unload-Reload Secant Modulus for Stage E, F, and G

3.3.3. Displacement-Controlled Test

Figure 44 reports together all the stages of the displacement controlled test as a force-displacement plot. In first day test, following initial penetration (stage A) the pipe was subjected to a series of 100 load cycles (stages C, E, G, and I) and a 1,000 load cycles (stage K). The cyclic displacement during each load cycle was approximately 4 mm (0.02D). At the end of stage C, E, G, and I, the loading was interrupted to allow rest periods of 0.5 to 4 hours. On the second day, larger cyclic loads were applied at different depths (Figure 45). All cyclic tests controlled by displacement had a load frequency of 0.1 Hz. Table 8 includes details about test program.

Figure 46 and Figure 47 show the first and last hysteresis loops in each stage on the first and second day, respectively. In Figure 46, reversal direction in load occurs in all cyclic loading stages except stage B, in which the loop just shifted down with increments in load cycles and the cyclic loads do not reach the maximum breakout force. From stage E, the breakout force begins to reduce with increasing cycles. Indeed, the loop gets more bent in shape at loads smaller than 1,000 N until it is almost flat. Due to the pause between each stage, the soil resistance of each first loop is larger than that of the last loop in the previous stage.

Table 8. Details for Displacement-Controlled Test (Test 3)

Day	stage	Description	Details
1	A	Penetration to 0.3D	0.05 mm/s
	B	Cyclic loading	5 cycles -281 +/- 1mm 0.005 Hz
	C	Cyclic loading	100 cycles -281 +/- 2mm 0.1 Hz
	D	Wait 0.5 Hrs	
	E	Cyclic loading	100 cycles -281 +/- 2mm 0.1 Hz
	F	Wait 1.0 Hrs	
	G	Cyclic loading	100 cycles -281 +/- 2mm 0.1 Hz
	H	Wait 2.0 Hrs	
	I	Cyclic loading	100 cycles -281 +/- 2mm 0.1 Hz
	J	Wait 4.0 Hrs	
	K	Cyclic loading	1000 cycles -281 +/- 2mm 0.1 Hz
2	A	Cyclic loading	721 cycles -281 +/- 2mm 0.1 Hz
	B	Cyclic loading	100 cycles -281 +/- 5.75mm 0.1 Hz
	C	Re-penetration to 0.5D	0.05 mm/s
	D	Cyclic loading	100 cycles -249.3 +/- 5.75mm 0.1 Hz
	E	Cyclic loading	100 cycles -249.9 +/- 14.96mm 0.1 Hz
	F	Wait 0.5 Hrs	
	G	Cyclic loading	35 cycles -249.9 +/- 14.96mm 0.1 Hz
	H	Re-penetration to 0.75D	0.05 mm/s
	I	Cyclic loading	100 cycles -204.5 +/- 5.75mm 0.1 Hz
	J	Cyclic loading	70 + 30 cycles -205.2 +/- 14.96mm 0.1 Hz
	K	Re-penetration to 1.0D & Extraction	0.05 mm/s

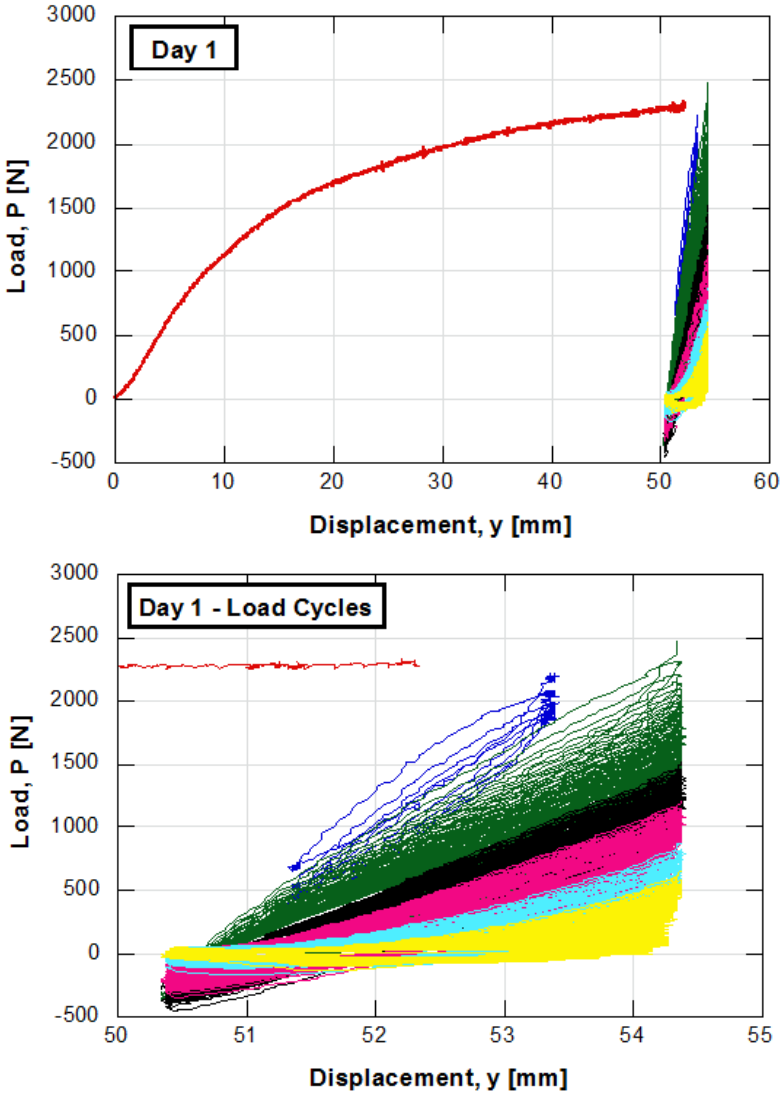

Fig. 44. Load-Displacement on Day 1 (NGI-Test 3)

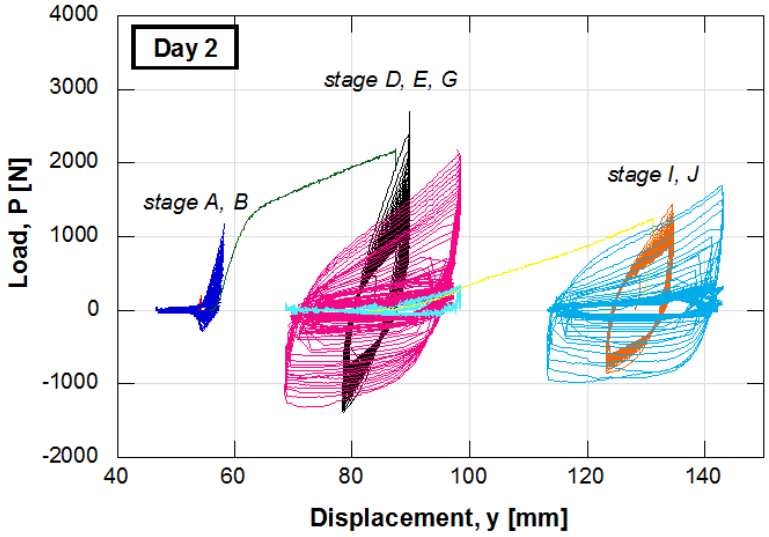

Fig. 45. Load-Displacement on Day 2 (NGI-Test 3)

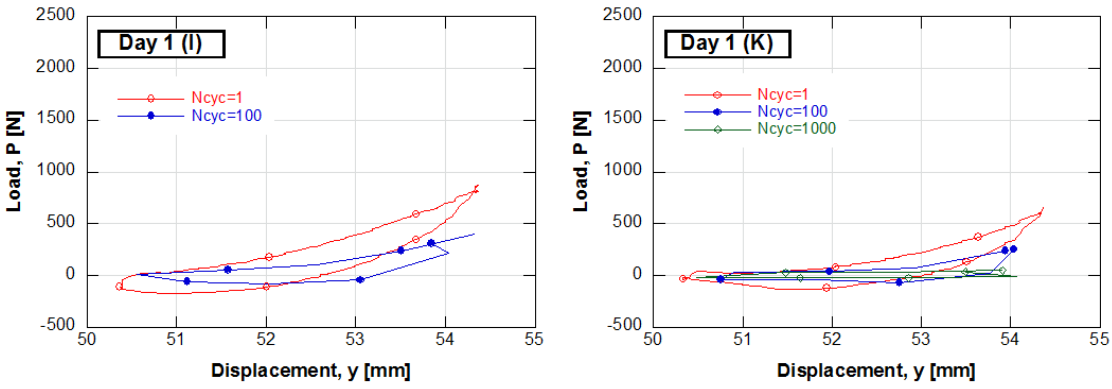

Fig. 46. Load-Displacement Curves for First and Last Cycle in Each Stage (Day 1)

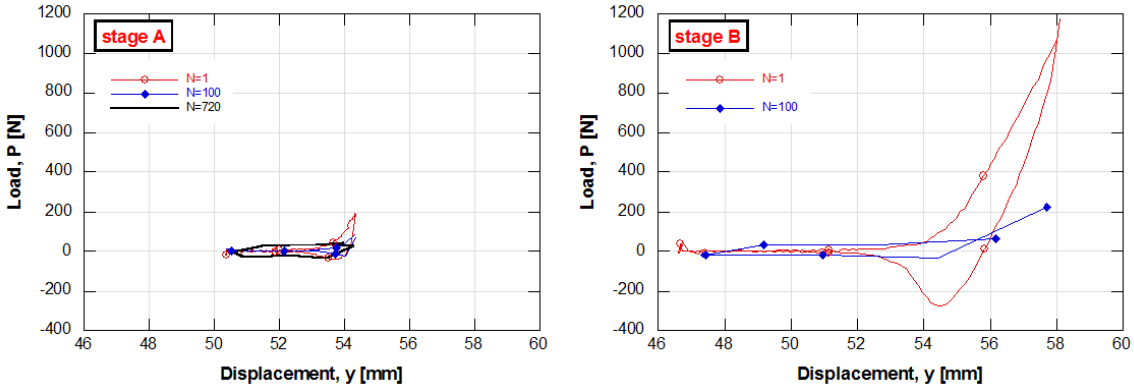

Fig. 47. Load-Displacement Curves for First and Last Cycle in Each Stage (Day 2)

a. Stiffness Variation

Figure 48 shows envelope values of measured soil resistance in compression and uplift. After a 1-hr rest period, some gain in soil resistance occurs, with about a 20% increase in compression resistance occurring between stage C and E in Figure 48. The secant stiffness again increases in a similar fashion over the rest period, although the stiffness does not appear to increase in exact direct proportion to the increase in maximum compression resistance. With continued cyclic loading in load stage E, compression resistance continues to degrade and actually degrades at an accelerated rate during the early load cycles after the resumption of loading. For short rest periods, the cyclic degradation throughout the different load stages shows a clear trend for both compression and tension resistance; the 'positive' effects of the waiting periods between each stage are relatively small compared to the degradation. For longer rest periods, e.g., the 4-hr rest period at the end of the 300th load cycle in Figure 48, the recovery of soil resistance is grater than for the shorter rest periods, although the soil resistance at the end of the 4-hr rest period (about 800 kPa) still falls well short of the maximum mobilized compression resistance (stage C) at the start of the test. Nevertheless, a roughly 50% increase in maximum compression resistance (550 to 800 kPa) did occur over the 4-hr rest period, so the time-related soil resistance recovery could be significant under certain circumstances. Figure 49 shows soil stiffness variation on load cycles. The trend of both of unload and reload stiffness is similar.

Figure 50 shows the corresponding normalized unloading secant stiffness versus cyclic displacement magnitude for selected load cycles. As cyclic loading progresses the compression resistance declines by about half after 100 cycles (stage C in Figure 48). Figure 50 shows the secant stiffness degrading in a commensurate fashion, with the stiffness for stage E being about 60% of that for stage C. It can be inferred that loading appears to both decrease the overall magnitude of secant stiffness, as well as alter the characteristics

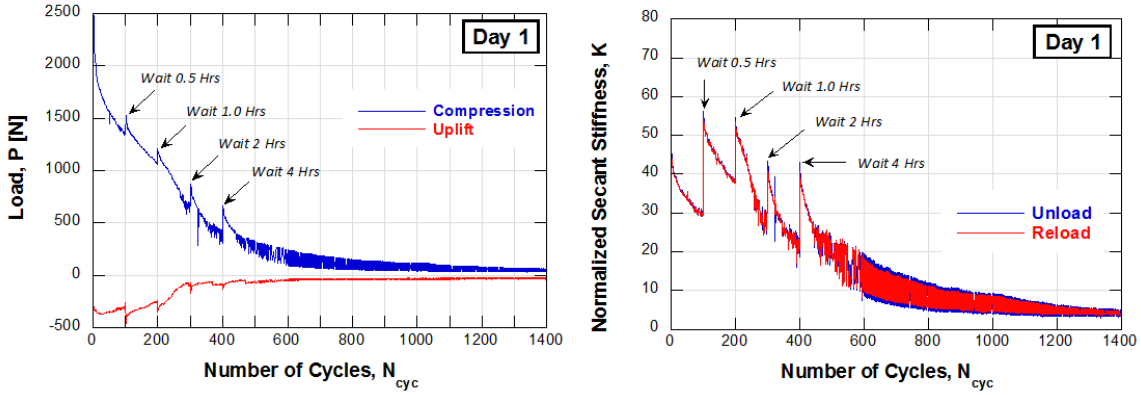

Fig. 48. Variation of Load and Secant Stiffness on Load Cycle (Day 1)

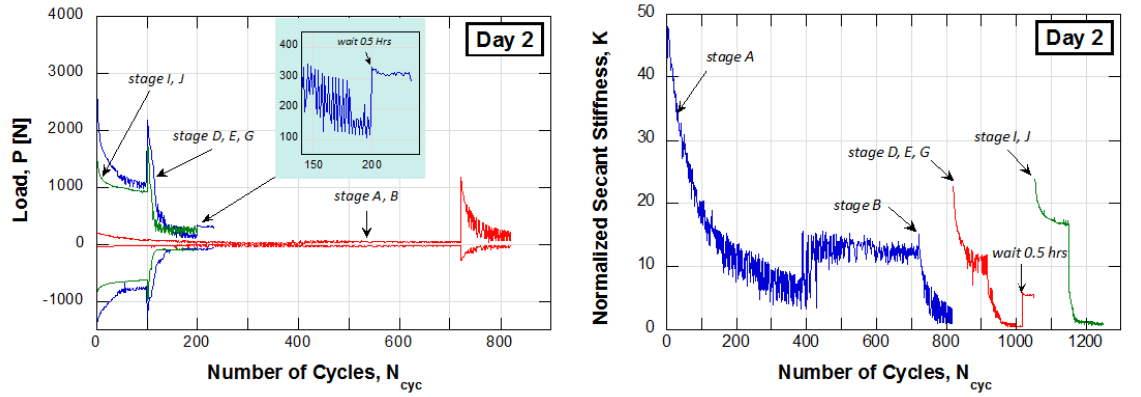

Fig. 49. Variation of Load and Secant Stiffness on Load Cycle (Day 1 - Stage C, E, G, I, K)

of the stiffness-displacement curve; i.e., in addition to an overall softening, the K-Δ y/D relationship shows a steeper downward trend with increasing displacement.

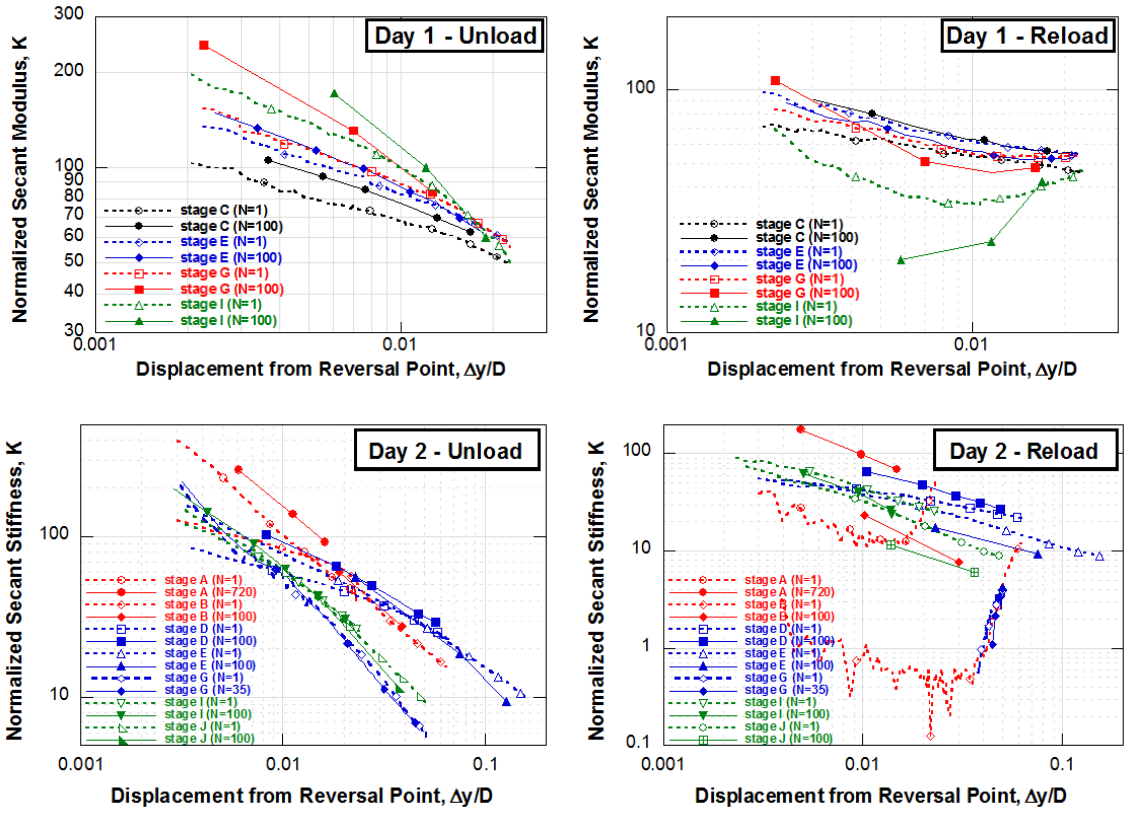

Fig. 50. Normalized Secant Stiffness

CHAPTER IV

NONLINEAR SEABED MODEL

4.1. Introduction

As mentioned in the previous chapter, the model tests (Clukey et al., 2005; Aubeny et al., 2008; Langford and Aubeny, 2008) illustrate well the complex pipe-soil behavior under vertically repeated loading. The distinctive features of the seabed behavior from experiments are as follows. First of all, load-displacement (P-y) curves contain separate segments corresponding to penetration, elastic rebound, partial detachment, full separation, and re-penetration. Secondly, the loading force depends on pipe diameter, soil strength profile, and penetration rate. Next, as the cycling progresses soil resistance at the maximum penetration reduces. Finally, the reloading force after resting on the seabed increases due to regained soil resistance by the consolidation effect. Consequently, the rest time is a major factor to determine the recovered soil strength.

Numerical modeling (Aubeny et al., 2006; Randolph and Quiggin, 2009) of the P-y relationship based on experimental outcomes, can describe all phases such as embedment, suction generation and release, and reloading-unloading conditions a riser may be subjected to. However, previous P-y models do not account for the reduction in soil stiffness due to repeated uplift and lay-down motions of the riser pipe, as well as the penetration rate and the soil consolidation effects on soil strength.

This work develops a non-linear degrading P-y model to describe seafloor-riser interaction with a mathematical formulation. The degrading model incorporates soil strength reduction by cyclic loading and penetration rate effects on soil strength into the non-degrading model (Aubeny and Biscontin, 2008) to better predict the P-y relationship. Figure 51 presents a schematic of the various modes in the degrading model arising during the

Table 9. Mathematical Equation for Bounding Loop

Path	Condition	Mode	Formulation
O-A	Loading	Initial Penetration	Power Law (4.1)
A-B	Unloading	Elastic Rebound	Parabola (4.20)
B-C	Unloading	Partial Separation	Cubic Polynomial (4.22)
C-D	Loading	Re-penetration (y$< y_1$)	Cubic Polynomial (4.23)
D-E	Loading	Re-penetration (y$> y_1$)	Power Law (4.24)

soil degrading process. Each mode links to the others by mathematical equations. Solid lines and dotted lines (Fig. 51) mean loading and unloading, respectively. Initially, the riser pipe is in contact with the surface of the seafloor (Initial Condition). After applying the initial load, the response about a certain displacement following the s-shaped backbone curve (Initial Penetration). If the riser unloads, the load rapidly decreases and it finally reaches the maximum suction force (Elastic Rebound). After the peak, it gradually converges to zero (Partial Separation) until perfect detachment (Full Separation). If the riser pushes into the preformed trench again, the P-y curve traces a cubic or hyperbolic path and will rejoin the backbone curve for further loading (Re-penetration).

Figure 52 illustrates the typical P-y behavior. The load term P designates the soil resistance in units of force per unit length, and y refers to the vertical displacement of the riser pipe. As noted earlier, upon experiencing a sufficiently large unload-reloading cycle from the backbone curve, the P-y curve will follow a 'bounding loop' characterized by a sequence of elastic rebound, partial and full separation of the riser from seafloor, re-contact and re-loading. Table 9 shows in detail the path corresponding to mathematical equations comprising the bounding loop.

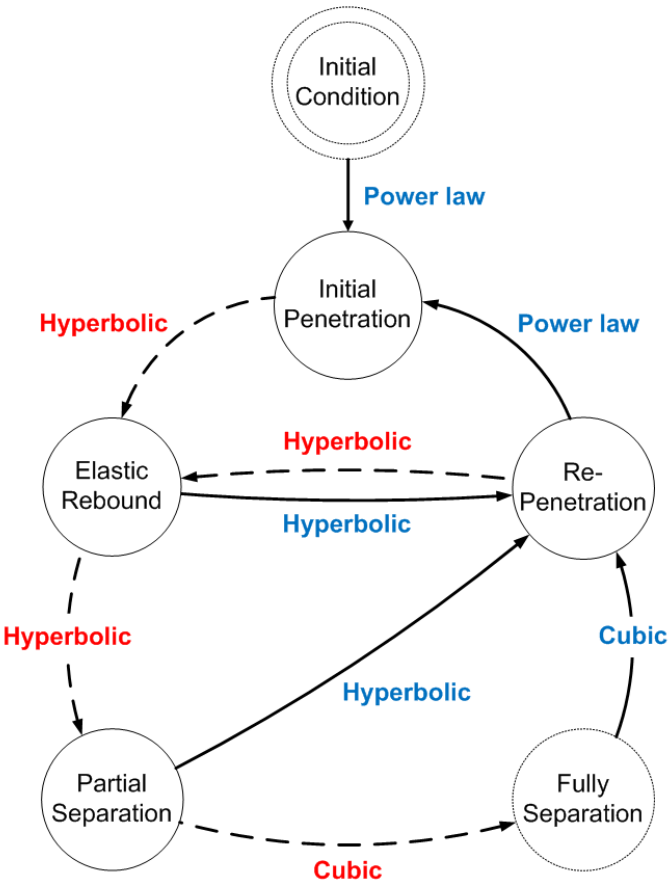

Fig. 51. Epitome of Riser-Seabed Interaction

In addition, a complete description of the bounding loop includes the following components in terms of fixed points in the P-y space (Fig. 52). From the described geometry of the bounding loop, point A on the backbone curve marks the maximum apparent penetration (y_1) and load (P_1) which control the loading-unloading-reloading loop, by changing the location of the points delimiting the various components of the P-y model. Points B and C are defined based on the apparent maximum penetration and load (Point A) for each loading step. Each point describes the maximum level of tension (suction) mobilized

during uplift and the depth at which the riser pipe becomes completely detached from the seafloor, respectively. Points D and E control the soil strength degradation set by the degradation rules. Point D represents the degraded force when compared with the previous force (P_1) at same maximum penetration (y_1). The dotted lines indicate unloading and reloading curves starting from reversals on the bounding loop. Those bounding curves started at the reversals truncating the bounding loop under the condition that the displacement did not exceed the maximum penetration (y_1). If a riser penetrates over the maximum previous depth, the reloading curve exceeds the bounding loop.

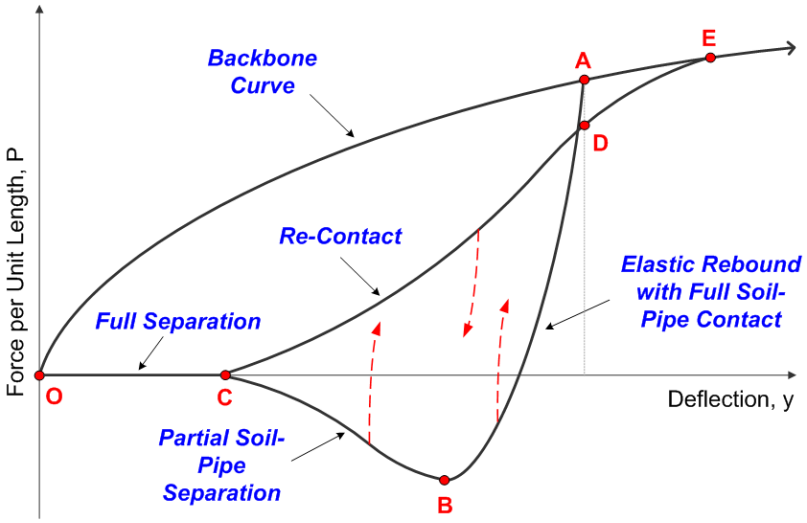

Fig. 52. Degrading P-y Loop

4.2. Bounding Loop

4.2.1. Backbone Curve

The proposed model establishes the backbone curve based on collapse load computations for a horizontal pipe. Figure 53 shows an idealized schematic of a typical trench cross section formed by an embedded pipe. For a pipe of diameter D penetrated in a trench of depth y_e, the collapse load P_b per unit length is expressed with a dimensionless bearing factor N_p and soil strength S_u as follows:

$$P_b = N_p S_u D \tag{4.1}$$

Normalized resistance P_b by soil strength at the bottom of the pipe and pipe diameter yields a bearing factor N_p that is insensitive to the details of the strength profile (Aubeny et al., 2005). Therefore, the measured soil strength from the seabed surface to the bottom of the pipe (y_e) is accepted as the most appropriate strength to be used in the backbone resistance P_b. For the linearly varying soil strength conditions with shear strength at the seafloor surface S_{uo} and strength gradient S_g with respect to depth y (Fig. 53), the undrained shear strength S_u at depth y_e can be characterized by the following equation:

$$S_u = S_{uo} + S_g y_e \tag{4.2}$$

T-bar is the widely used tool to examine the seabed strength profile. The measured shear strength by T-bar varies depending on penetration velocity because of strain rate effects (Biscontin and Pestana, 2001; Lunne and Andersen, 2007). To incorporate the rate effect into the backbone curve, the measured soil strength $S_{u\cdot m}$ by T-bar is calibrated by the following rate factor:

$$f_r = 1 + \lambda_{ref} \log(V/V_{ref}) \qquad \text{where} \quad V = v/D \tag{4.3}$$

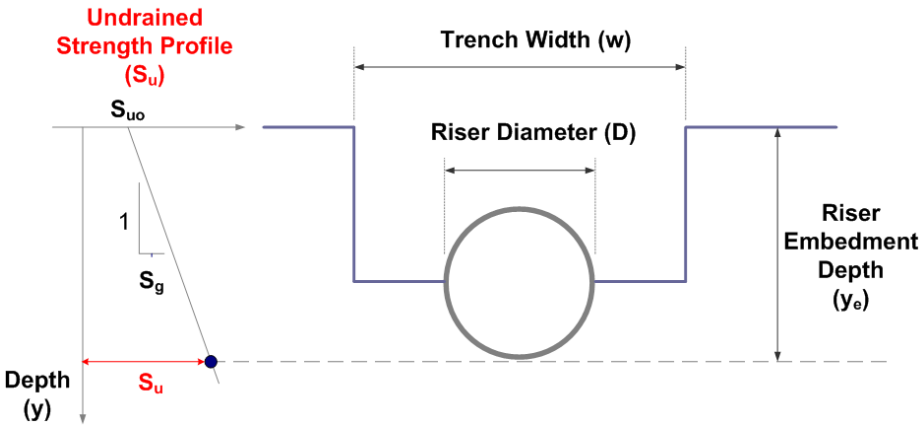

Fig. 53. Riser Trench and Seafloor Characteristics

The parameter λ_{ref} is a strain rate multiplier corresponding to reference velocity V_{ref}, the penetration rate of test probe (T-bar) normalized by the diameter and V is the penetration velocity of riser. The adjusted shear strength S_u for rate effect is expressed as:

$$S_u = f_r \cdot S_{u \cdot m} = [1 + \lambda_{ref} \log(V/V_{ref})] \cdot (S_{uo} + S_g y) \tag{4.4}$$

Previous studies (Murff et al., 1989; Bridge et al., 2004; Aubeny et al., 2005) proposed the analytical estimates on the bearing factor N_p. Based on finite element and method of characteristics solutions, the power-law empirical fit for normalized trench width by diameter, w/D=1 (Aubeny et al., 2005), show effective agreement with bearing factor N_p in the entire depth except for the normalized displacement by diameter (y_n) less than 0.1. The proposed model uses the following functions for estimating the bearing factor:

$$N_p = a(y_n)^b \qquad \text{where} \quad y_n = y/D \tag{4.5}$$

where a and b are fitting constants. Table 1 (Ch.2) proposed by Aubeny et al. (2005)

shows values for the fitting constants a and b for various conditions of penetration and pipe roughness. In the range of y_n less than 0.1, the estimating bearing factor is corrected to the following expression to improve fit with measured data:

$$N_p = f_p \cdot N_{p(y_n=0.1)} = \left[\frac{2(y_n/0.1)}{(y_n/0.1)+1}\right] \cdot a(0.1)^b \tag{4.6}$$

Finally, the soil resistance P_b, including rate effect, is the following:

$$P_b = N_p S_u D = N_p(f_r \cdot S_{u\cdot m})D \tag{4.7}$$

Equation 4.7 is extended as:

$$P_b = \begin{cases} \left[\frac{2(y_n/0.1)}{(y_n/0.1)+1} \cdot a(0.1)^b\right]\left[1+\lambda_{ref}\log\left(\frac{V}{V_{ref}}\right)\right][S_{uo}+S_g y]\,D & \text{for } y_n < 0.1 \\ \left[a(y_n)^b\right]\left[1+\lambda_{ref}\log\left(\frac{V}{V_{ref}}\right)\right][S_{uo}+S_g y]\,D & \text{for } y_n \geq 0.1 \end{cases} \tag{4.8}$$

It should be noted that Equation 4.5 and Table 1 (Ch.2) consider only the conditions where the trench width equals trench diameter, w/D=1. As visual observations (Bridge and Howells, 2007) showed that the width of a trench formed by riser motion can be substantially greater than one pipe diameter, this study extends the finite element solution for collapse load up to w/D=4.

Figures 54 summarizes the calculations for two boundary roughness conditions. The studies shows that the effect of a widened trench is a reduction in the maximum bearing resistance, $N_{p\cdot max}$, that develops at large y/D. Figure 55 illustrates the degree of the reduction in $N_{p\cdot max}$ with increasing w/D. Further, at sufficiently large w/D the collapse load behavior essentially follows that of a shallowly embedded pipe on a level ground surface; i.e., the shearing resistance from the soil mass adjacent to the side walls of the trench becomes negligible. Based on the finite element calculations, the trench width at which side wall resistance effects become negligible (Fig. 55) is about w/D=2.75 for rough pipes and

w/D=2 for smooth pipes.

Hence, N_p values predicted from Equation 4.5 are capped to account for trench width effects according to the following relationships:

$$\textit{Rough Pipes}: \quad N_p = \begin{cases} 7.74 - 1.22(w/D - 1) & \text{for } w/D < 2.75 \\ 5.60 & \text{for } w/D > 2.75 \end{cases} \tag{4.9}$$

$$\textit{Smooth Pipes}: \quad N_p = \begin{cases} 6.73 - 2.33(w/D - 1) & \text{for } w/D < 2 \\ 5.60 & \text{for } w/D > 2 \end{cases} \tag{4.10}$$

Although trench width is also a major factor for the bearing factor, the proposed model focuses on the vertical displacement due to vertical riser motion only.

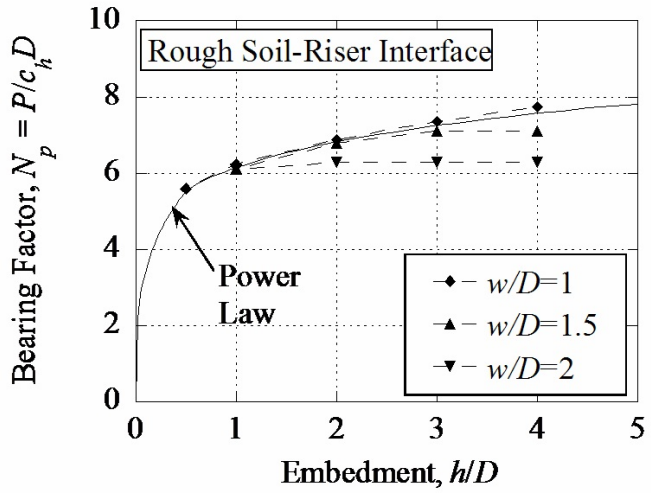

(a) rough

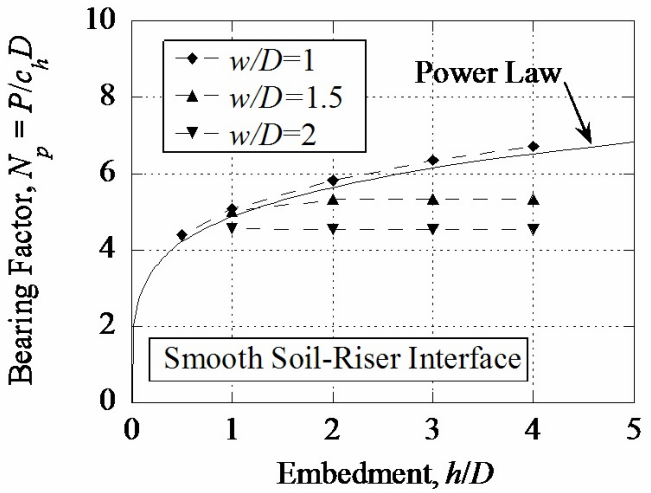

(b) smooth

Fig. 54. Backbone Curves for Rough (a) and Smooth (b) Pipes (Aubeny and Biscontin, 2009)

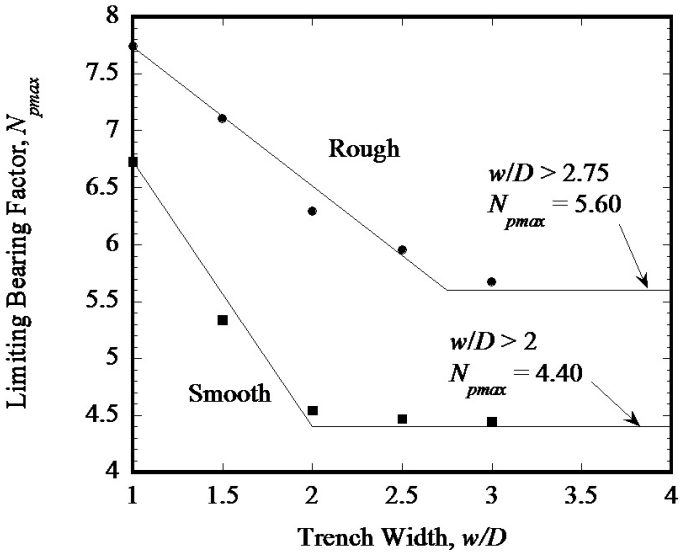

Fig. 55. Effect of Trench Width on Maximum Soil Resistance (Aubeny and Biscontin, 2009)

4.2.2. Degrading Rule

The model includes two control points (D and E in Fig 56) to describe soil strength reduction. For each incremental loading step, the normalized apparent maximum penetration ($y_{c\cdot n}$) controlling further penetration depth is defined as a function of the accumulated displacement (λ_n) and the parameters α and β.

$$y_{c\cdot n} = y_{1\cdot n} + \alpha(\lambda_n)^{\beta} \tag{4.11}$$

where $y_{1\cdot n}$ is dimensionless previous maximum penetration depth. The accumulated displacement (λ_n) only for unloading serves as a measure of energy dissipation. It is defined as:

$$\lambda_n = \sum_{i=1}^{N} \mid \Delta y \mid \tag{4.12}$$

where Δy is the incremental deflection and N is the current increment. Under the condition of y larger than y_1, both of λ_n and N are set to re-zero and then the summation is started again for the following loading steps at further penetration depth. The controlling force (P_c) corresponding to y_c is computed by power law (Eq.4.1).

Although the same loading force is applied, the riser is penetrated to deeper trench depth due to soil strength reduction near the trench after unloading. Degrading control point D predicts this strength reduction (P_d) at previous maximum penetration (y_1). Model test results indicates that most strength reduction occurs within a few cycles. Therefore, the reduced force due to repeated loading is defined as

$$\Delta P_{N_c} = f_d \cdot \Delta P_{(N_c=1)} \tag{4.13}$$

where ΔP_{N_c} is difference between resistance reduction at current cycle (P_{N_c}) and previous cycle (P_{N_c-1}) and $\Delta P_{(N_c=1)}$ is maximum resistance reduction (usually occurring in the first cycle). As number of cycles increases, the reduction rate is defined by a degrading rate

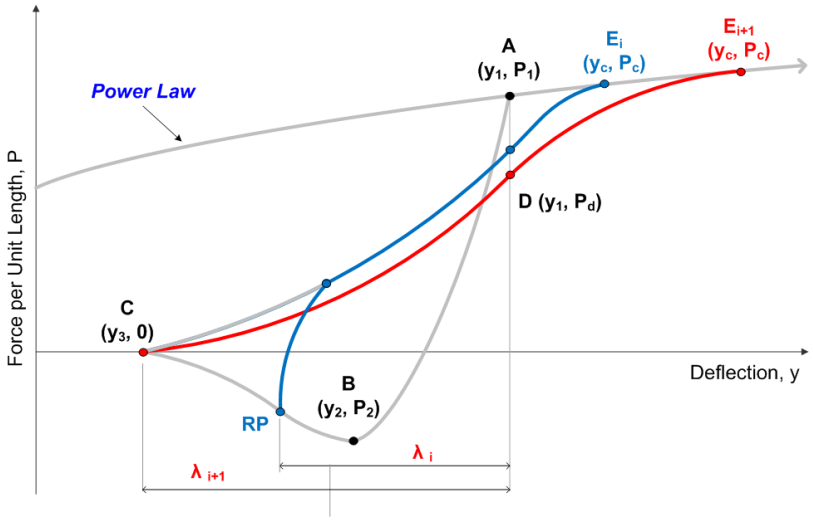

Fig. 56. Degrading Rule

function, f_d is:

$$f_d = \mu + (1 - \mu)e^{\epsilon(1-N_c)} \tag{4.14}$$

where N_c is number of cycles, μ and ϵ are degrading parameters. While parameter μ determines the residual ratio of decreased resistance per cycle for maximum cyclic strength reduction, ϵ controls strength reduction rate per cycle (Fig. 57).

In particular, maximum penetration load for first cycle, $\Delta P_{(N_c=1)}$ can be written as:

$$\Delta P_{(N_c=1)} = f_y \cdot \Omega P_1 \tag{4.15}$$

where f_y is ratio of unloading distance for maximum unloading distance when the riser is fully separated from the seabed from previous depth, and parameter Ω determines the magnitude of force reduction occurring in the first cycle. The unloading displacement

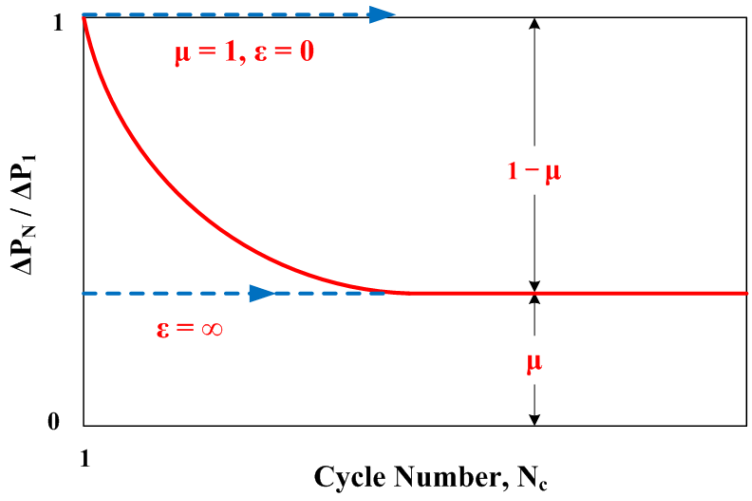

Fig. 57. Degrading Function

ratio, f_y, is defined as

$$f_y = \begin{cases} \zeta t + (1-\zeta)\eta(1-(1-\frac{t}{\eta})^3) - \eta\frac{y_1-y}{y_1-y_2} & \text{for } y \geq y_2 \\ \zeta t + (1-\zeta)(\eta + (1-\eta)(\frac{t-\eta}{1-\eta})^3) - \eta + (1-\eta)\frac{y_2-y}{y_2-y_3} & \text{for } y < y_2 \end{cases} \tag{4.16}$$

where y_2 is depth of maximum uplift resistance within the current cycle and scale factor, t, responding to y is computed by equation 4.16. The scale function of f_y ranges from 0 to 1. If y_{rev} is less than y_3, then y_{rev} is y_3. This work uses 0.3 and 0.7 for ζ and η, respectively. Figure 58 shows the shape of function f_y. Therefore, P_{N_c} is expressed as:

$$P_{N_c} = P_{N_c-1} - f_d \cdot (f_y \cdot \Omega P_1) \tag{4.17}$$

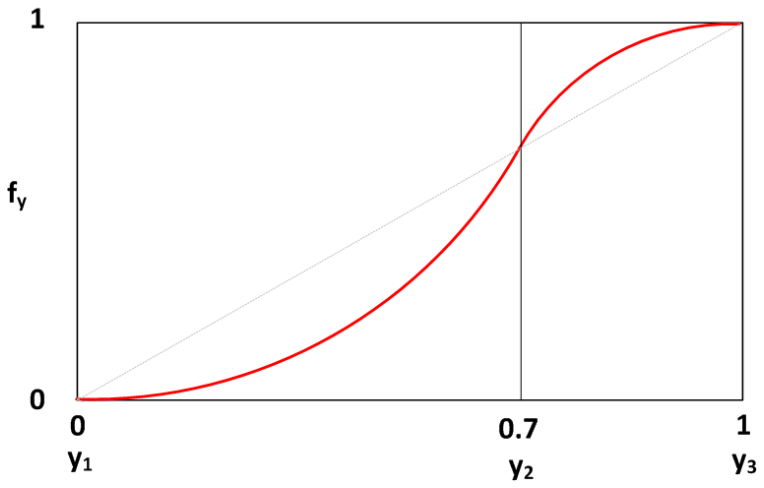

Fig. 58. Scale Function for Reloading Curve

4.2.3. Unloading Curve

Figure 59 shows the typical bounding loop in P-y space. Point A (Fig. 59) is a state variable determined by the maximum previous plastic penetration of the riser into the seafloor. Point B (Fig. 59) indicates the maximum uplift resistance (suction force) defined as:

$$P_2 = -\phi P_1 \tag{4.18}$$

where ϕ is the model parameter to control the uplift force. Point C (Fig. 59) is the depth of full detachment (y_3) calculated by the following equation:

$$(y_2 - y_3) = \psi(y_1 - y_2) \tag{4.19}$$

The model parameter ψ is related with the ratio of the displacement differences between path A-B and B-C. A hyperbolic relationship defines the elastic rebound P-y curve

on path A-B (Fig. 59) as follows:

$$P = P_1 + \frac{y - y_1}{\frac{1}{k_0} - \frac{y - y_1}{P_{ult}}} \qquad \text{where} \quad P_{ult} = (1 + \omega)P_1 \tag{4.20}$$

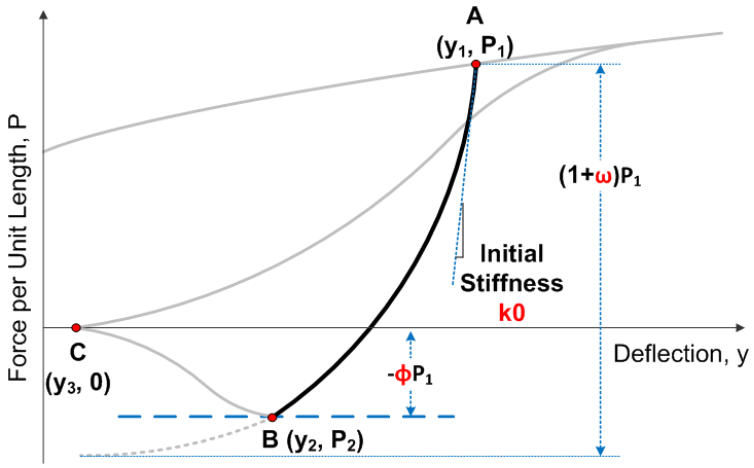

Fig. 59. Hyperbolic Unloading Curve

where k_0 defines the initial slope of the hyperbola and the model parameter ω controls the asymptote of the hyperbola. The parameter k_0 is ideally estimated from laboratory tests. The tension limit imposed by equation 4.18 truncates the hyperbola (Eq. 4.20) at Point B (Fig. 59). Therefore, the depth where maximum uplift force generates follows as:

$$y_2 = y_1 - \frac{P_1(1 + \phi)(1 + \omega)}{k_0(\omega - \phi)} \tag{4.21}$$

The partial detachment mode, represented by the segment between points B and C of the P-y curve in figure 60, is described by a polynomial curve. This curve basically describes how the peak force (P_2) generated during uplift gradually reduced to zero at the depth where riser completely detaches from the seabed as the normalized differential

displacement ratio y_r decreases from 1 to 0. The unloading curve is defined as follows:

$$P = P_2 \left(\frac{2y_r^n}{y_r^{n+3} + 1} \right) \qquad \text{where} \quad y_r = \frac{y - y_3}{y_2 - y_3} \tag{4.22}$$

where n is fitting parameters (usually n = 2 or 3).

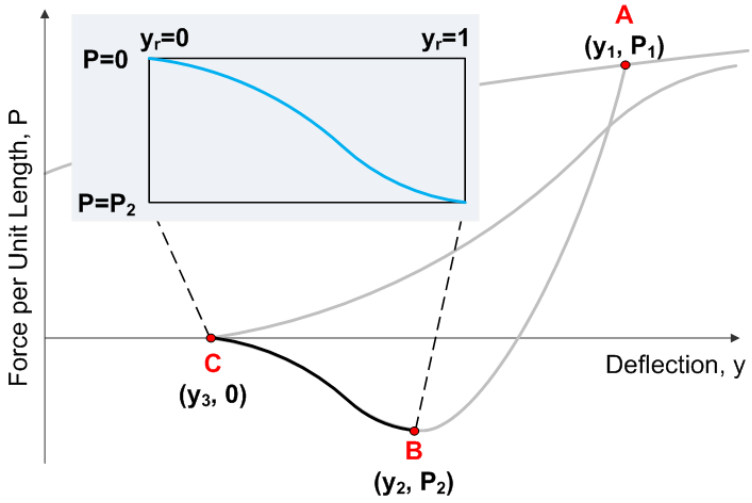

Fig. 60. Cubic Unloading Curve

4.2.4. Reloading Curve

Figure 61 represents the reloading curve of the bounding loop passing through three points: C, D, and E. Points C and D indicate re-contact after separation with seabed and strength reduction (P_d) at the previous maximum penetration (y_1), respectively. Point E (y_c, P_c) on the backbone curve controls the shape of the reloading curve in the range of $y > y_1$ (Path D-E). State variables P_d and y_c are computed by the degrading rules described in section 4.2.2. Path C-D is a polynomial similar to curve of Equation 4.22.

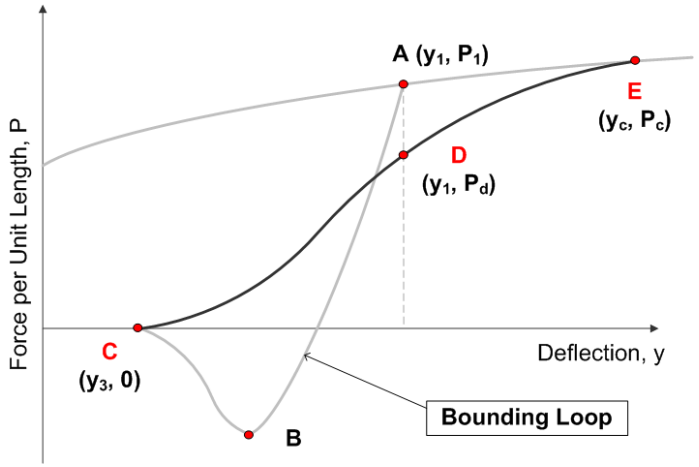

Fig. 61. Reloading Curves of Bounding Loop

For the range of $y < y_1$ (Path C-D), the reloading curve is

$$P = P_d \left(\frac{2y_r^{3.5}}{y_r^6 + 1} \right) \qquad \text{where} \quad y_r = \frac{y - y_3}{y_1 - y_3} \tag{4.23}$$

For the range of $y > y_1$ (Path D-E), the load P is computed by

$$P = P_b(y) \cdot ((1 - P_r) \cdot y_r^{0.5} + P_r)) \tag{4.24}$$

where $y_r = (y - y_1)/(y_c - y_1)$ and $P_r = P_d/P_b(y_1)$.

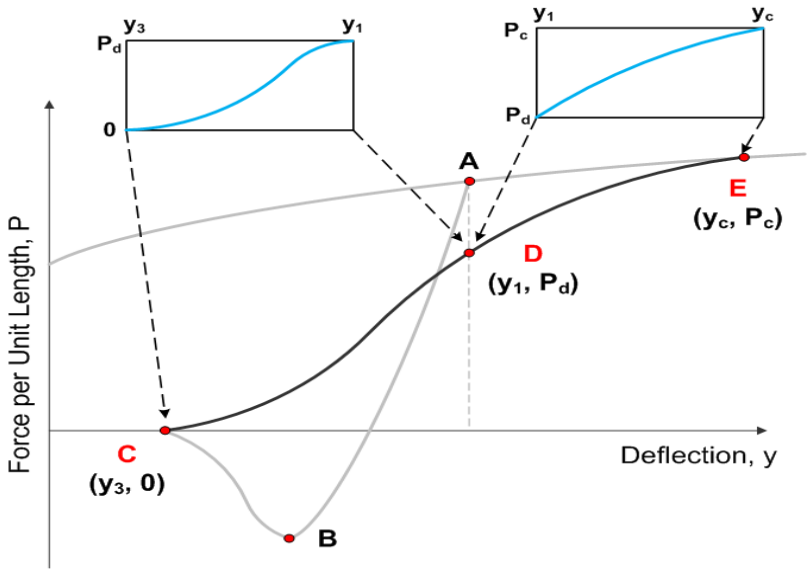

Fig. 62. Hermite Curve Application

4.3. Reversals from the Bounds of the Hysteretic Loop

The preceding section includes P-y relationships for the bounding loop developed by large riser motion; i.e., deflection reversal from maximum penetration depth (point A in fig. 61) and deflection reversal from point C (fig. 61) where a riser fully detaches and re-contacts. In addition, reversals within the bounding loop can generally occur from any arbitrary point, along the bounding loop. For reversals in the bounding loop, both unloading and reloading curves are modeled with modified hyperbola from equation 4.20 as follows:

$$P_{re} = P_{rev} + \frac{y - y_{rev}}{\frac{1}{k_0} + \frac{y - y_{rev}}{P_{ult}}} \tag{4.25}$$

Unlike the unloading hyperbola, the reloading curve starting from the bounding loop passes through point D (fig. 63) to describe strength degradation. So, undamaged reloading curve (Eq. 4.25) is modified by factor P_d/P_b. Therefore, the reduced reloading parabola is

$$P = \frac{P_d}{P_b} \cdot P_{re} \tag{4.26}$$

Figures 64 and 65 show an example of deflection reversals from the bounding loop. Within the bounding loop, unload/reload curves departing from any deflection reversals (RP in Fig. 64) on bounding loop segments A-B (elastic rebound) and B-C, the region of partial detachment, initially follow a hyperbola (eq. 4.25). However; if hyperbola load path for reversal from bounding loop segments B-C crosses the cubic bounding curve, the P-y relationship must follow the boundary (fig. 64(a)). For unloading after reversal from the bounding loop, the unloading curve (eq. 4.25) is truncated by the unloading bounding curves (eqn. 4.20 or 4.22) and tracks them (fig. 64(b)). Figures 65 show the load path starting from reversals on the cubic bounding curve. If the reversal penetration is less than y_1, the load path is truncated by the bounding curves. Otherwise, the unloading curve departing from reversal in the region of $y > y_1$ generates a new bounding loop (fig. 65(a)).

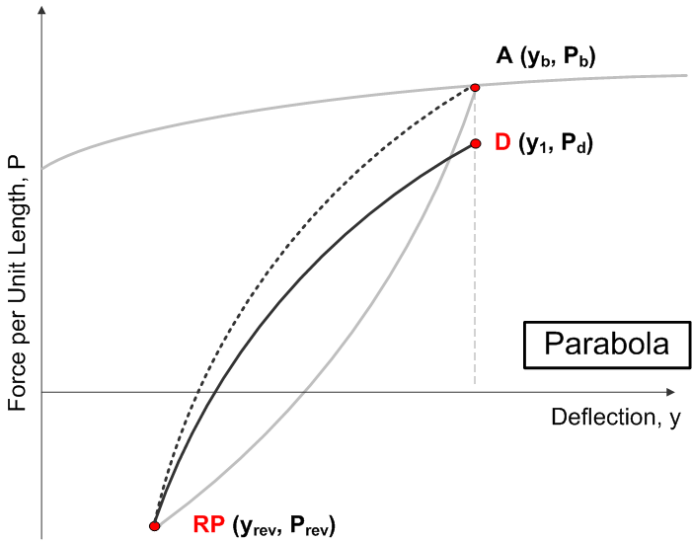

Fig. 63. Reloading Curves on Reversal Position

For continued reloading after reverse from cubic bounding curve, the load path is also truncated by the previous cubic bounding curve (fig. 65(b)).

In summary, the P-y behavior at any arbitrary location on or within the bounding loop is a path dependent process. Description of the path requires following state variables:

- Points consisting of bounding loop:

  Point A (y_1, P_1) - maximum advancement on the backbone curve.

  Point B (y_2, P_2) - maximum uplift force starting from point A.

  Point C (y_3, 0) - completely detached from seabed or re-contact

- Points describing degrading effect:

  Point D (y_1, P_d) - reduced strength at maximum penetration depth

  Point E (y_c, P_c) - non-disturbed seabed depth under cyclic loading

- Point of the last deflection reversal from the bounding loop: Point RP.

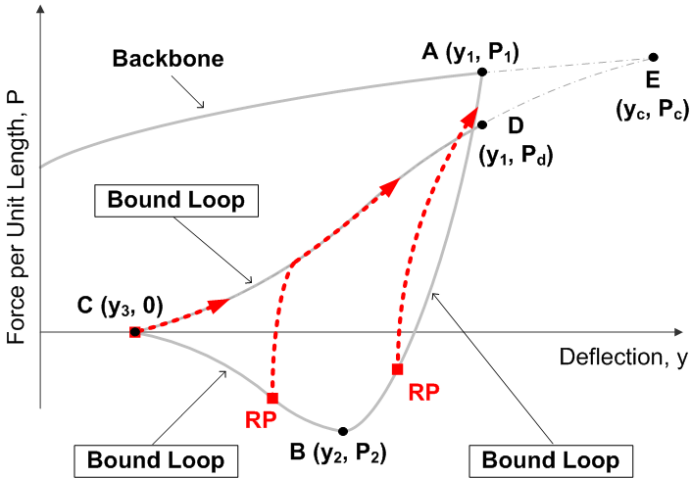

(a) Reload

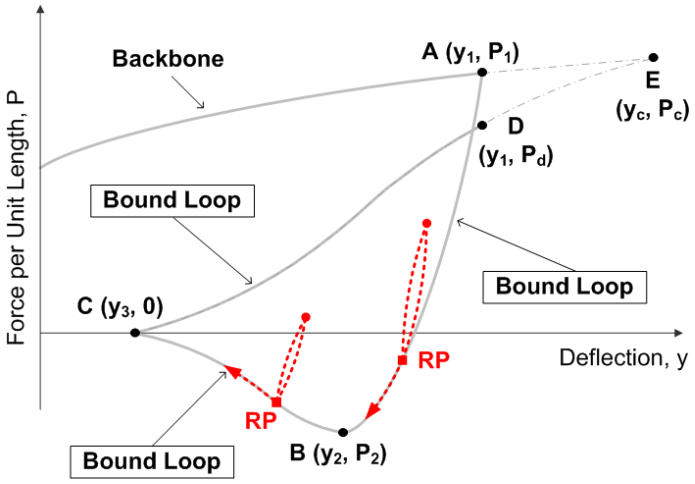

(b) Reload-Unload

Fig. 64. Load Path from Unload Boundary

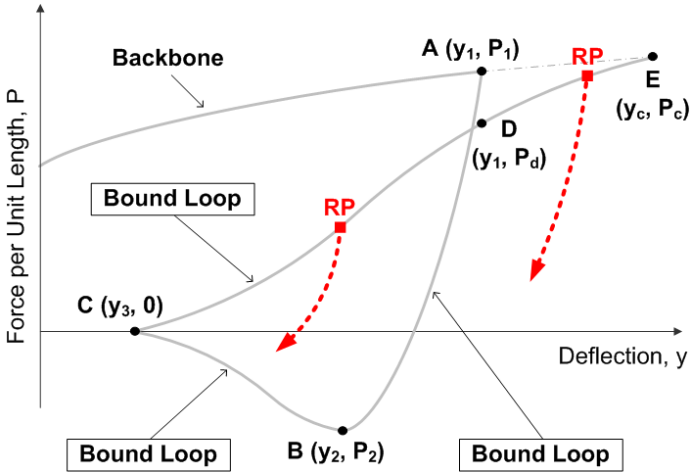

(a) Unload

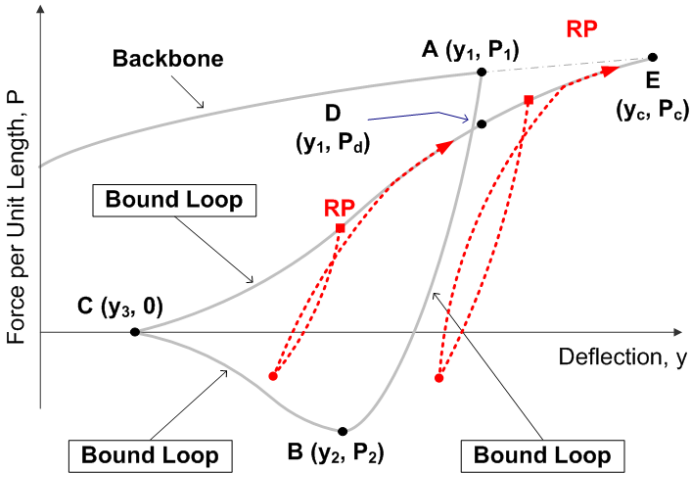

(b) Unload-Reload

Fig. 65. Load Path from Reload Boundary

4.4. Parametric Study

The objective of this parametric study is to examine the proposed non-linear P-y model response to determine model parameters associated with each mathematical curve. Assessing the impact that changing certain parameters can have on the proposed model allows to define reasonable parameter ranges, evaluate model limitations, and analyze the results of each parameter variation.

Model parameters are varied to show their effects on penetration depth, maximum uplift force, and degraded soil strength characteristics. Dependencies between the variables and characteristics established from the parametric analysis, as well as the magnitude of the effect, can be used as a guideline in selecting the most effective means to alter a particular mathematical curve configuration so that the desired characteristics can be obtained.

The developed P-y models will be simulated with specified parameter values that can be derived from laboratory model tests, including a cyclic loaded pipe in a clay test bed or that can be within the acceptable range. In particular, input parameters related with pipe property and soil strength should be derived from laboratory model tests. Generally, these parameters have limited range. In addition, it is important that all parameters be expressed in units of measure that are compatible.

Soil model parameters include initial stiffness, maximum uplift load, and uplift load limit for parabola, as well as coefficients a and b for backbone curve and breakout parameter (ψ) for cubic unloading curve. Degrading parameters control state variables P_d and y_c (Fig.61). While α and β determine y_c, μ and ϵ control degrading rate depend on number of cycles. Finally, Ω decides magnitude of initial strength reduction with normalized unloading displacement and load at maximum penetration.

Figure 66 shows the feature of the degrading non-linear model over a few arbitrary cycles of uplift and re-penetration. Example simulation includes displacement loading

with 10 cycles at penetration depth of $0.8D$ to specifically evaluate degrading effect. The default model parameters and input values implemented in this calculation are summarized in Table 10.

In the following sections, the parametric analysis will be carried using a sample input to illustrate the features of the model and the effects of the various parameters.

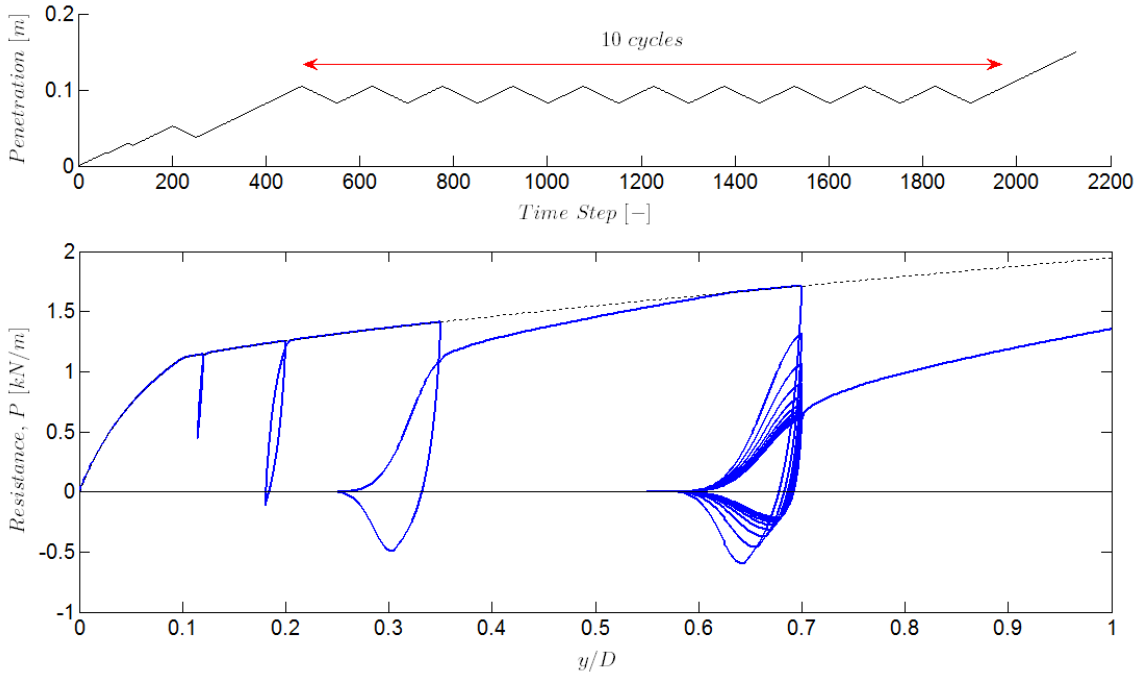

Fig. 66. Sample Simulation under Given Motion

Table 10. Model Parameters for Sample in Figure 66

Type	Parameter	Symbol	Value
Material	pipe diameter	D	$0.15\ m$
	mudline shear strength	S_{uo}	$2.0\ kPa$
	shear strength gradient	S_g	$5.0\ kPa/m$
	initial stiffness	k_0	1200
Bounding Loop	power law coefficient	a	6.8
	power law exponent	b	0.12
	maximum uplift load	ω	0.75
	uplift load limit	ϕ	0.35
	breakout	ψ	1.3
Degrading	re-penetration	α	0.7
	re-penetration	β	0.25
	degrading rate	μ	0.01
	degrading rate	ϵ	0.43
	Initial load drop	Ω	0.23

4.4.1. Material Parameters

Material parameters affecting the load-deflection relationship, especially backbone curve, are: riser outer diameter (D), soil strength profile (S_{uo}, S_g), and . Previous laboratory model tests (Howells, 1995; Hatton and Willis, 1998) used pipes with diameters ranging from 10 to 175 mm (Table 3 in Ch.3), and riser diameters currently applied in the field are from 203 to 762 mm (8$\sim$30 inches) (Howells, 1995; Hatton and Willis, 1998). For seabed strength, in-situ soil strength profiles measured at various seabed location were shown in Figure 5 (in Ch. 2). The general ranges of S_{uo} and S_g are from 0 to 4 kPa and from 0 to 20 kPa/m, respectively. The strength gradient is zero, the soil strength profile is constant with depth; otherwise, it is linearly increasing with depth. Figure 67 illustrates the P-y responses of risers with large and small diameters representing for field and model test cases. Using a larger diameter leads to a higher slope of the backbone curve which also effects the overall P-y curve since the response depends on the increased maximum penetration load, P_b. Figure 68 also shows the P-y relationship dependence on soil strength profile with S_{uo} = 2, 4 kPa and S_g = 0, 5, 10 kPa/m, respectively. Similarly to the effect of diameter, both soil strength at seabed surface and strength gradient change the size of the backbone curve and the bounding loop proportion to their magnitude. In addition, a ten fold increase of loading velocity leads to an increase of about 30 percent in the maximum bearing load at all penetration depths (Fig. 69).

In summary, parameters of D, Su, and v should be based on experimental data and are directly related with bearing factor calculation. Therefore, increased values of these parameters lead to larger resistance from backbone curve, but they also affects the uplift force and strength degradation.

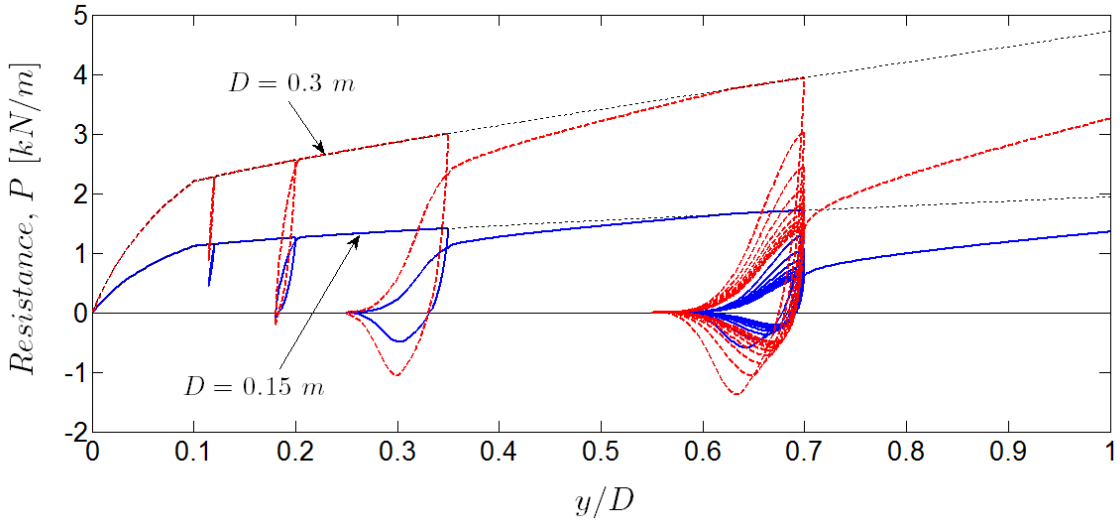

Fig. 67. Riser Diameter Influence

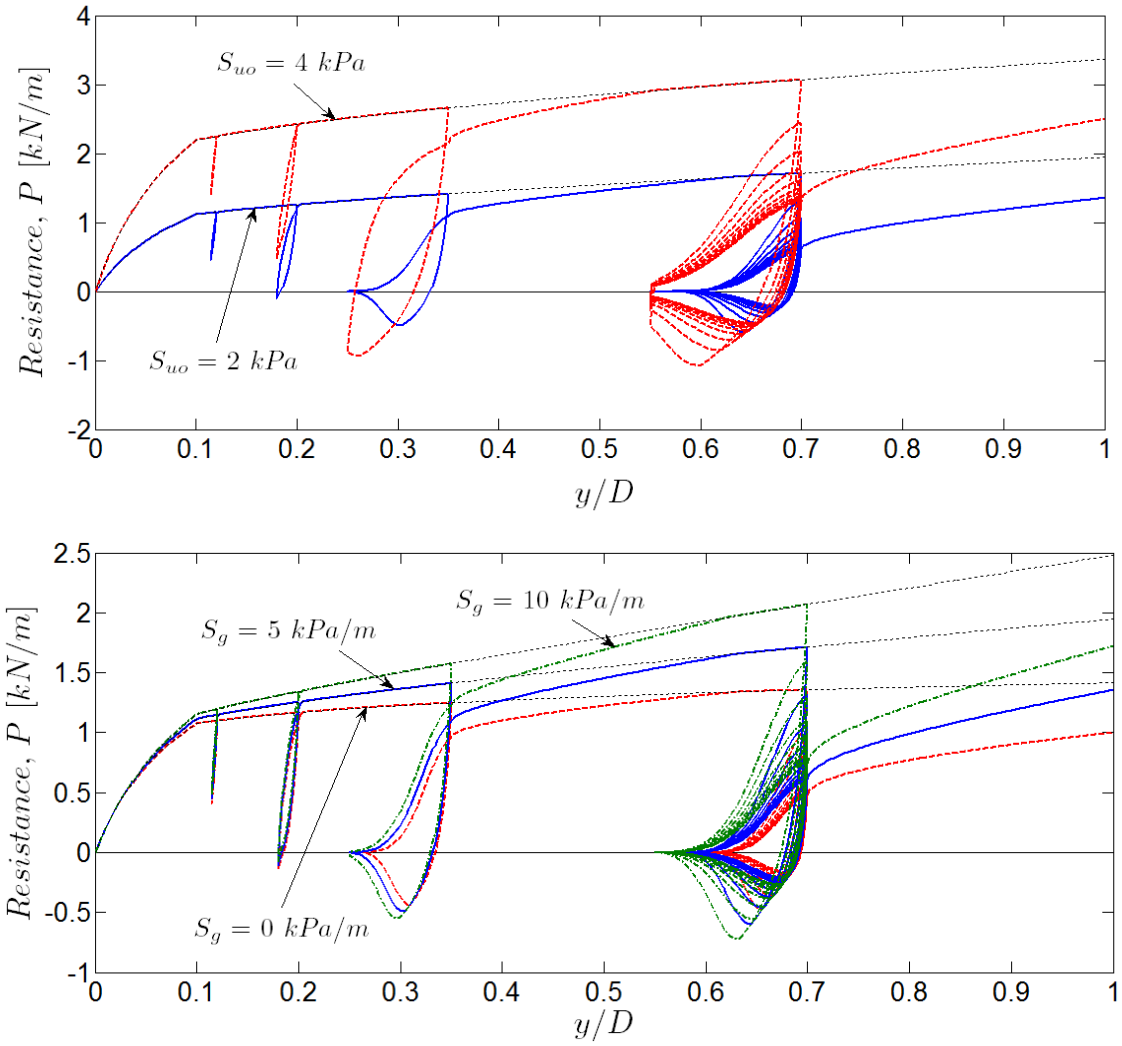

Fig. 68. Seabed Strength Influence

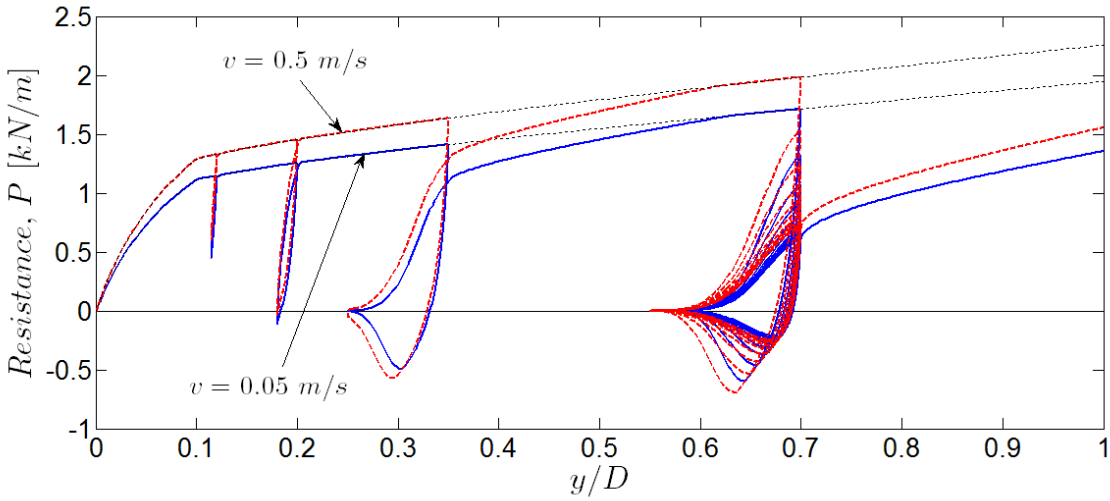

Fig. 69. Penetration Velocity Influence

4.4.2. Model Parameters

Parameter a and b govern the bearing factor (Eq. 4.5), derived from an empirical expression matched to finite element solutions by Aubeny et al. (2005). The selection of these parameters needs to take into account pipe roughness and dimensionless penetration depth as proposed in Table 1 (Ch. 2). To better predict P-y behavior, it is recommended those parameters are obtained from experimental results. Figure 70 presents measured bearing factors from NGI and COFS laboratory model tests as mentioned in Chapter 3. The bearing factor is the penetration load normalized by pipe diameter, pipe length, and modified undrained soil strength depending on penetration rate. It is usually then fitted with a power law (Eq. 4.5). The best fitting coefficients values in this work are a = 6.8 and b = 0.12. Figure 71 illustrates coefficients effect on P-y response. Maximum resistance is governed more by parameter a than b.

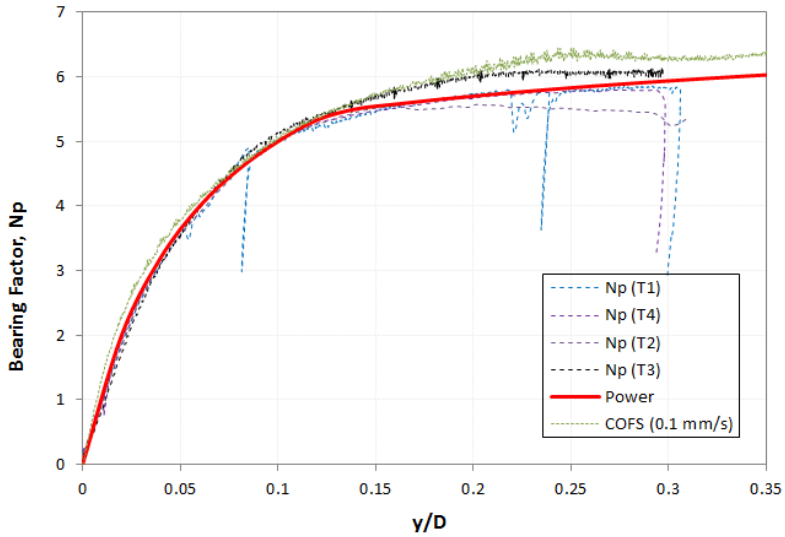

Fig. 70. Fitting Coefficients a and b for NGI

The unloading-reloading parabola depends on a combination of parameters such as

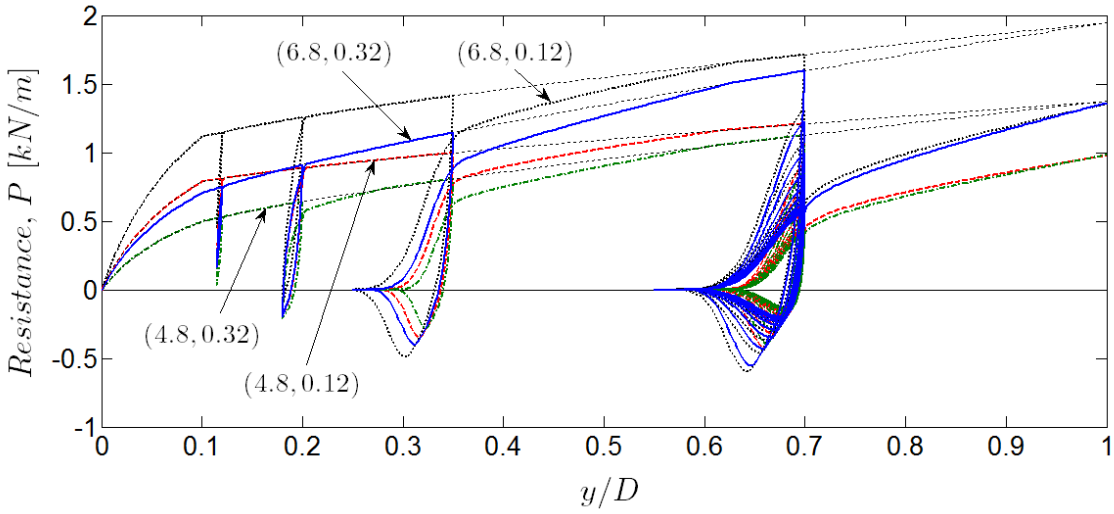

Fig. 71. Influence of Backbone Curve Coefficients

initial stiffness (k_0), maximum uplift load (ω), and uplift load limit (ϕ). These parameter values are also chosen from experimental data. Maximum uplift load ratio (ω) can never be less than the tension limit (ϕ) due to the characteristic of hyperbola (Eq. 4.20).

Figure 72 and 73 show model performance depending on various values of parameters k_0 and ω. During cyclic loading, smaller values of k_0 and ω result in wider bounding loops. Proposed model response is more sensitive on the variation of maximum uplift load parameter than on the initial stiffness parameter.

Figure 74 shows parameter ϕ effect on sample simulation. The suction limit parameter, ϕ, is the ratio of maximum uplift (or breakout) force and the previous maximum penetration force. The breakout force is strongly related to the loading rate at which the pipe is lifted up, the rest time, breakout time during which upward motion is sustained, as well as the recent history of cyclic motion (Bridge et al. 2004). When breakout time is shorter, suction

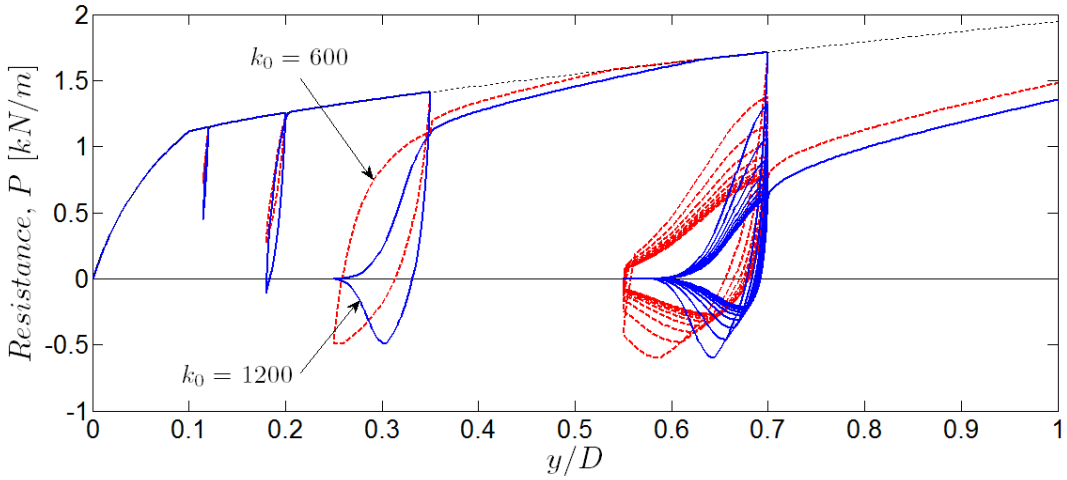

Fig. 72. Influence of k_0

forces is larger. In addition, longer rest time increases uplift force (Bouwmeester et al., 2009).

However, the proposed model does not account for the variation of suction force caused by break time and rest time effects due to limitations of experimental data currently available. Therefore, the suction limit parameter, ϕ, depends only on the previous maximum penetration force. In this study, the empirical coefficient (ϕ) depends on the subsoil type suggested by Poinc (1970). For the clayey seafloor, the range of ϕ is from 0.25 to 0.45.

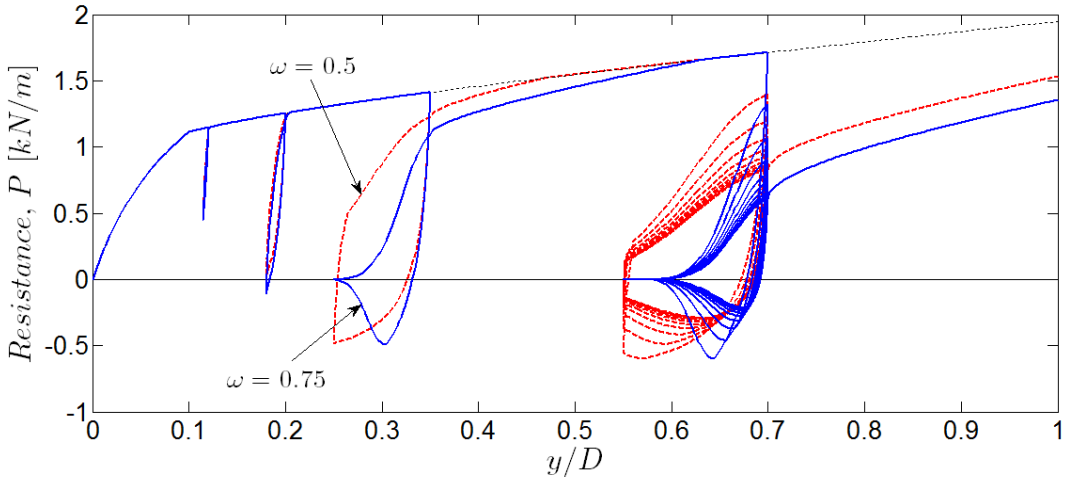

Fig. 73. Influence of ω

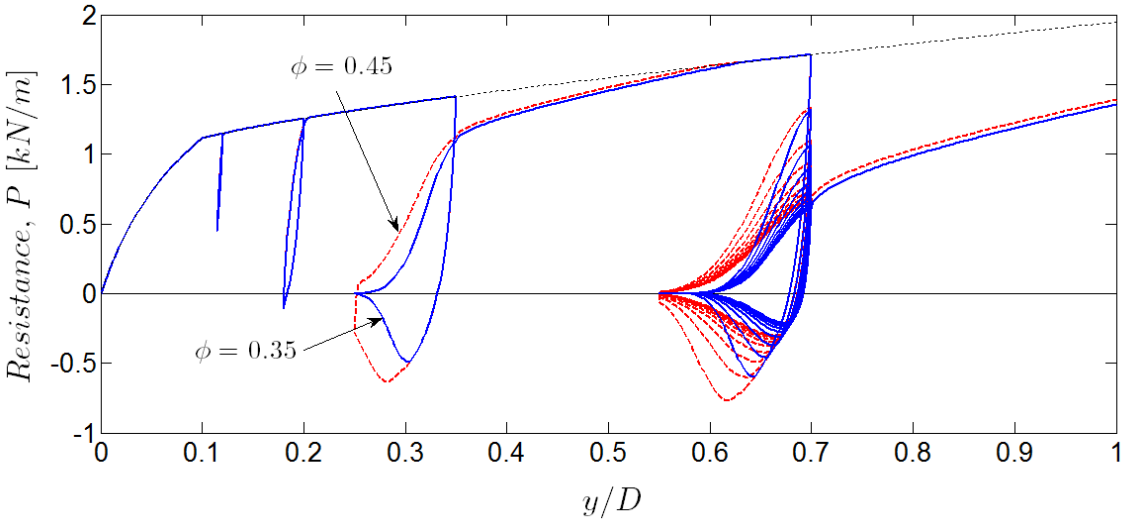

Fig. 74. Influence of ϕ

Figure 75 shows parameter ψ effect on model response under a given loading history. Parameter ψ determines y_3, the point where the pipe becomes completely detached from seabed; and, therefore controls how the uplift force decays. This is also related with debris generated by up-down riser motion and loading rate, but does not typically exceed a distance equal to the pipe diameter. Therefore, values in the range of 1.0 to 3.0 are investigated for this work.

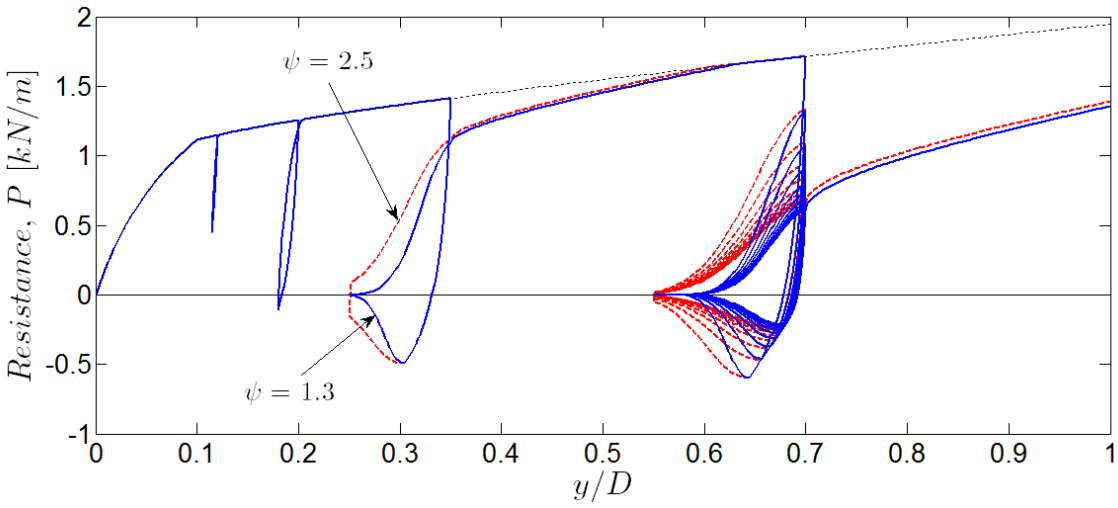

Fig. 75. Influence of ψ

Parameter n controls the unloading cubic curve shape. Figure 76 shows parameter n effect on model performance for n=3 and n=6 . Larger n releases suction force more rapidly.

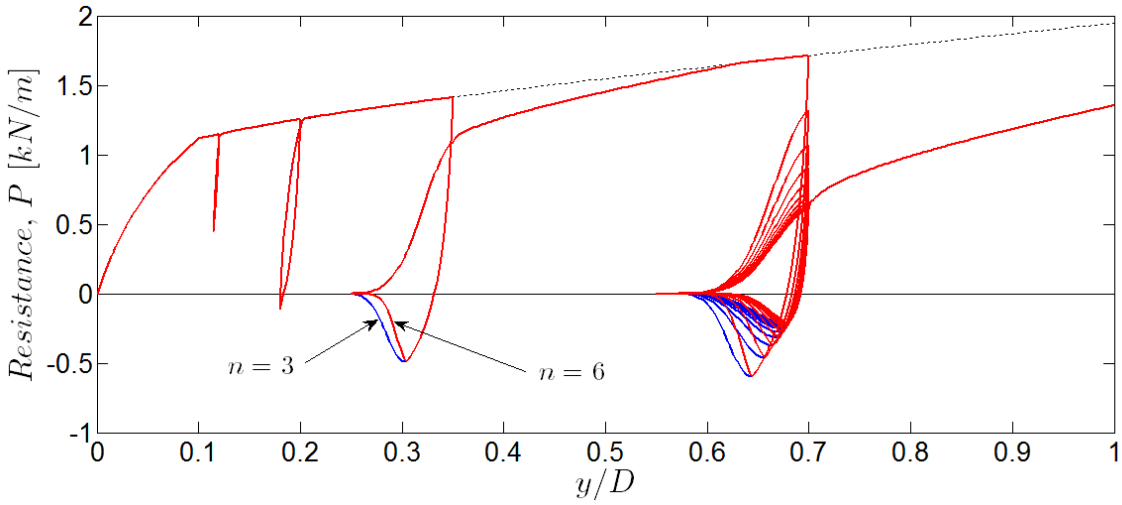

Fig. 76. Influence of n

In summary, parameters k_0, ω, and ϕ determine the size of the initial hyperbolic unloading path, while ψ and n describe the unloading cubic curves. Strength reduction is controlled by degrading parameters and also affects the shape and size of these curves. Wider bonding loops result from higher values of these parameters.

4.4.3. Degrading Parameters

Determination of reduced strength (P_d) at previous maximum penetration depth by cyclic loading is governed by parameters: μ, ϵ, and Ω. Parameters μ and ϵ in equation 4.14 control the rate of degradation, while Ω is the amount of strength reduction during the first cycle of loading.

Figure 77 shows the example simulation for various degrading parameters μ, ϵ, and Ω. Parameter μ controls the residual load difference P_d, and ϵ is relevant for strength reduction rate. Large value of ϵ results in rapidly decreasing load, so reduced load after 10 cycles is higher if a small value of ϵ. Initial strength reduction, Ω, is the most sensitive of the degrading parameters.

Figure 78 shows the effect of parameters α and β on y_c for the example simulation. The combination of parameter α and β controls re-penetration when exceeding the previous maximum depth.

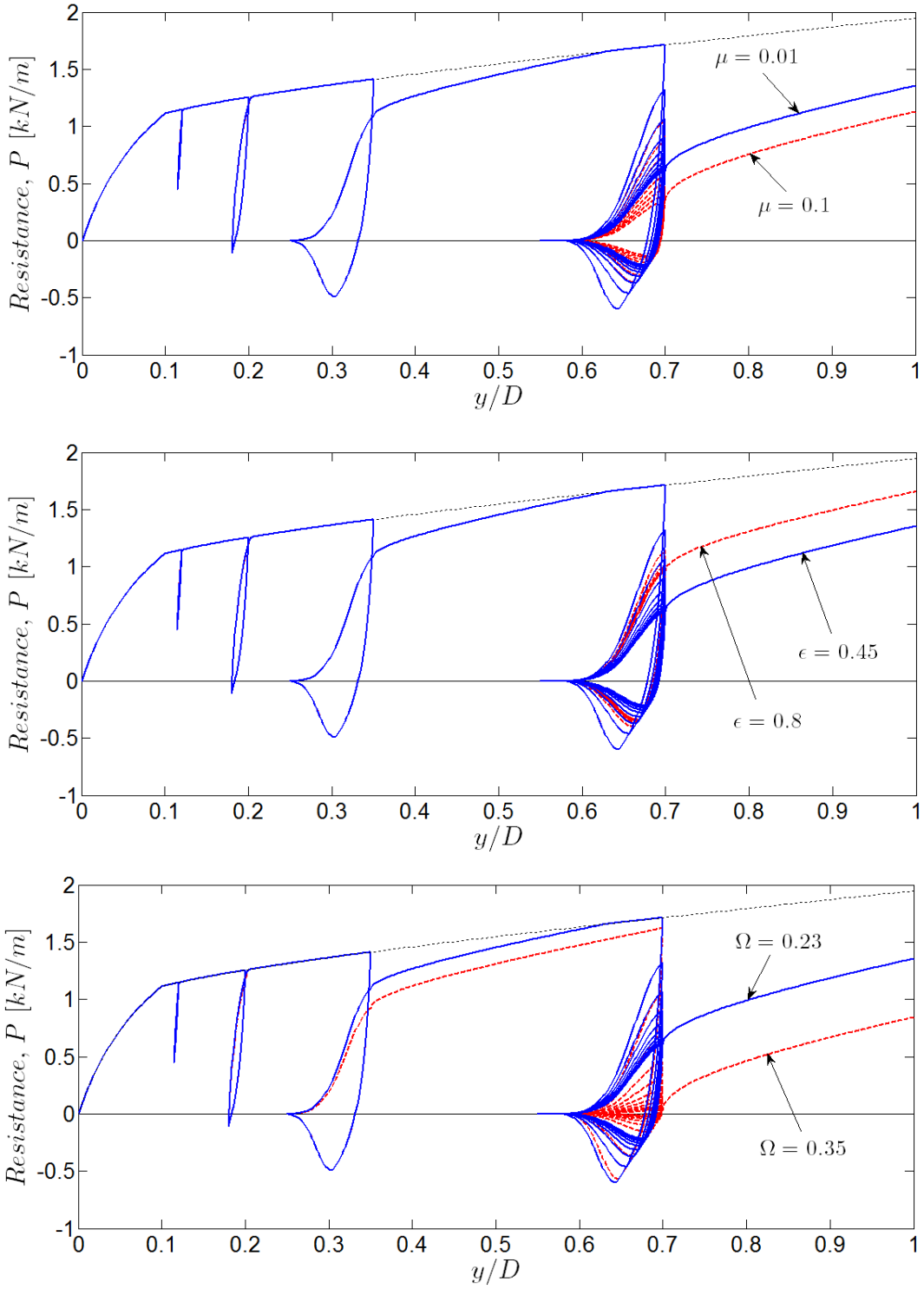

Fig. 77. Influence of Degrading Parameters μ, ϵ, and Ω

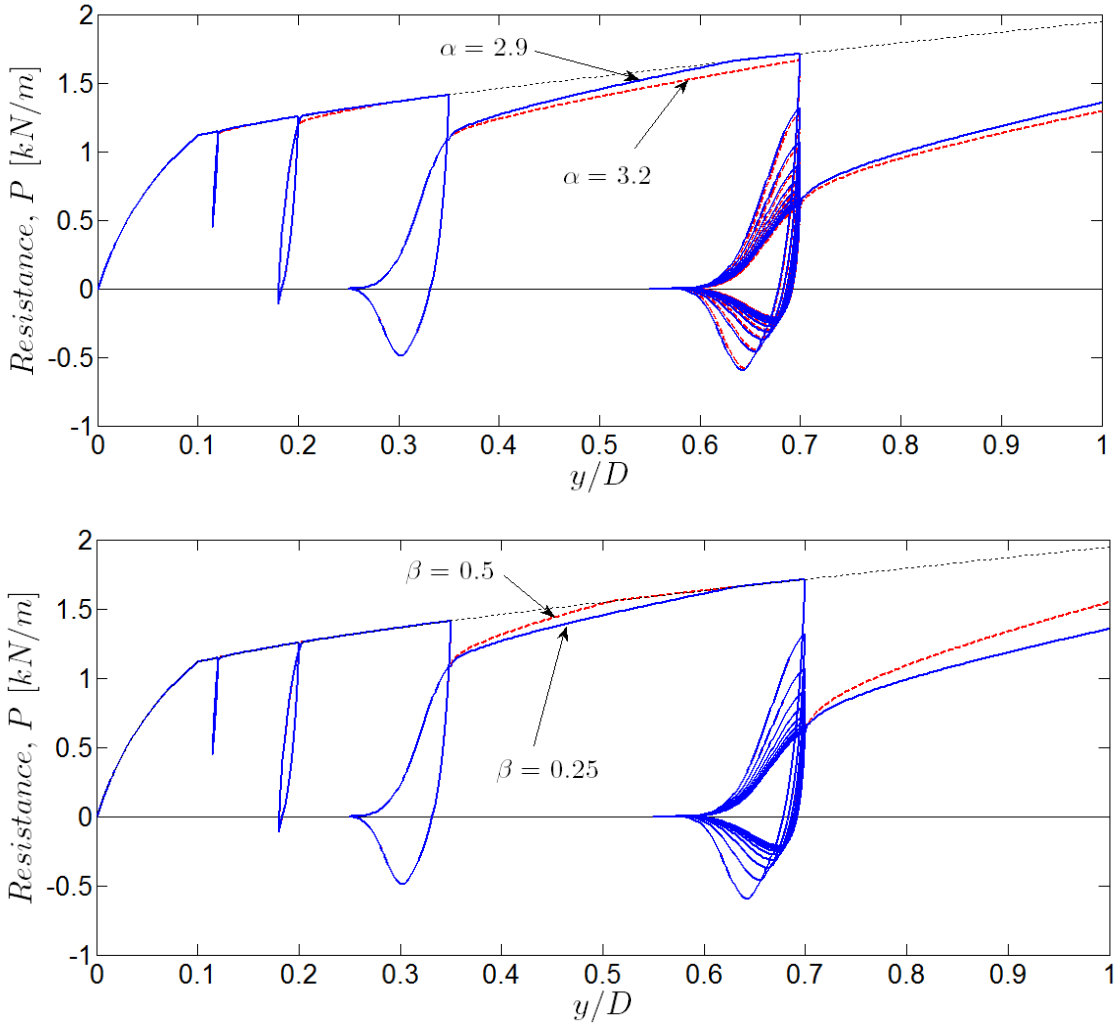

Fig. 78. Effect of Degrading Parameters α

4.5. Validation of Nonlinear Degrading Model (NGI)

4.5.1. NGI Test

The following work will validate the model framework by comparing model preditions with the existing experimental data. The advantages of the proposed model can also be highlighted. In particular, strength reduction caused by cyclic loading and variation of bounding loop will be discussed in this section. Simulations using the non-linear P-y model will adopt parameters as detailed in Table 11 to compare with NGI laboratory model test data.

a. Hybrid Tests

Figure 79 and 80 shows comparison of a simulation by the proposed model and NGI test 1 and 4, respectively. In both model tests, the pipe penetrated to a depth of 52 mm (0.3D) at constant rate of displacement of 0.05 mm/s for test 1 and 0.5 mm/s for test 4. Model simulations with input parameters in table 11 agree well with hybrid model test data executed by NGI except for maximum uplift load in case of normalized displacement (y/D) larger than half diameter. Additionally, model simulations at two different loading velocities in the two figures show the rate effect well.

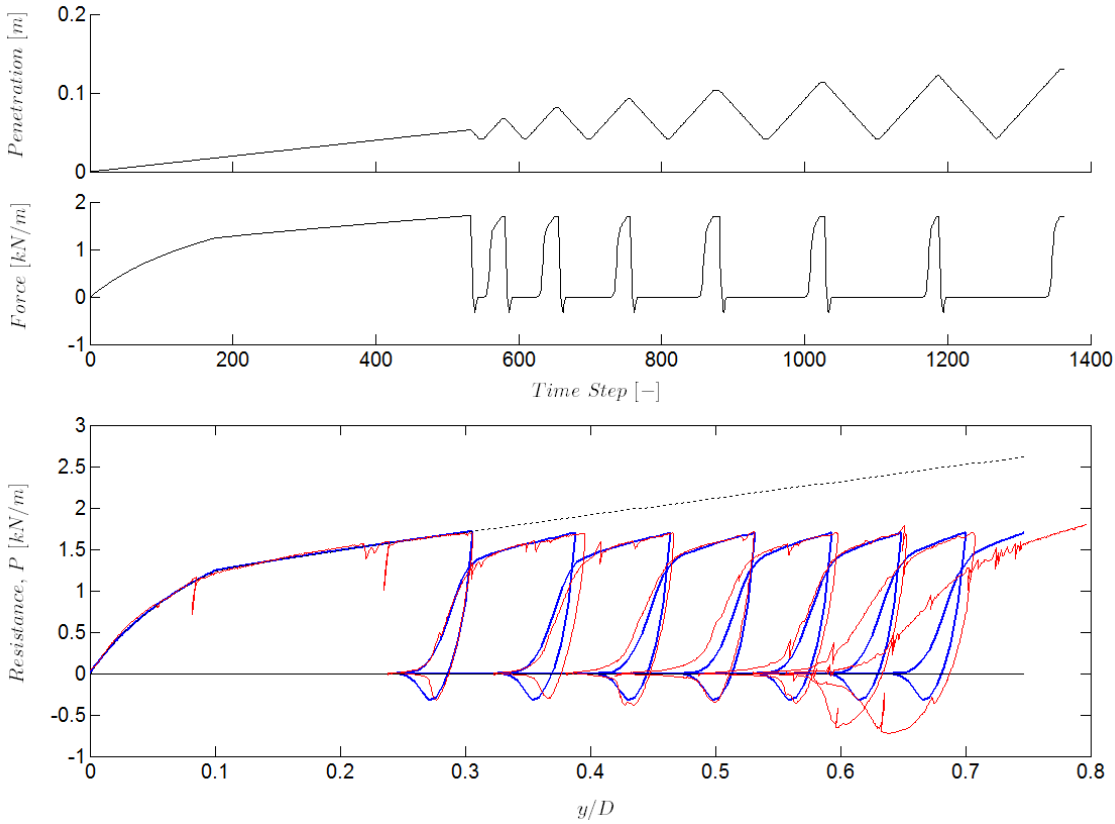

Fig. 79. Simulation for Hybrid Test (NGI-1)

Table 11. Model Parameters for NGI Test in Figures 79-82

Parameter	Symbol	Value for Test 1-3 (Test 4)
Pipe diameter [m]	D	0.174
Mudline shear strength [kPa]	S_{uo}	2
Shear strength gradient [kPa/m]	S_g	13
Loading velocity [mm/s]	v	0.05 (0.5)
Power law coefficient	a	6.8
Power law exponent	b	0.12
Initial stiffness	k_0	1200
Maximum uplift load	ω	0.75
Uplift load limit	ϕ	0.2 (0.4)
Breakout	ψ	1.0 (1.3)
Re-penetration	α	0.7 (1)
Re-penetration	β	0.25
Degrading rate	μ	0.01
Degrading rate	ϵ	0.45
Initial load drop	Ω	0.23

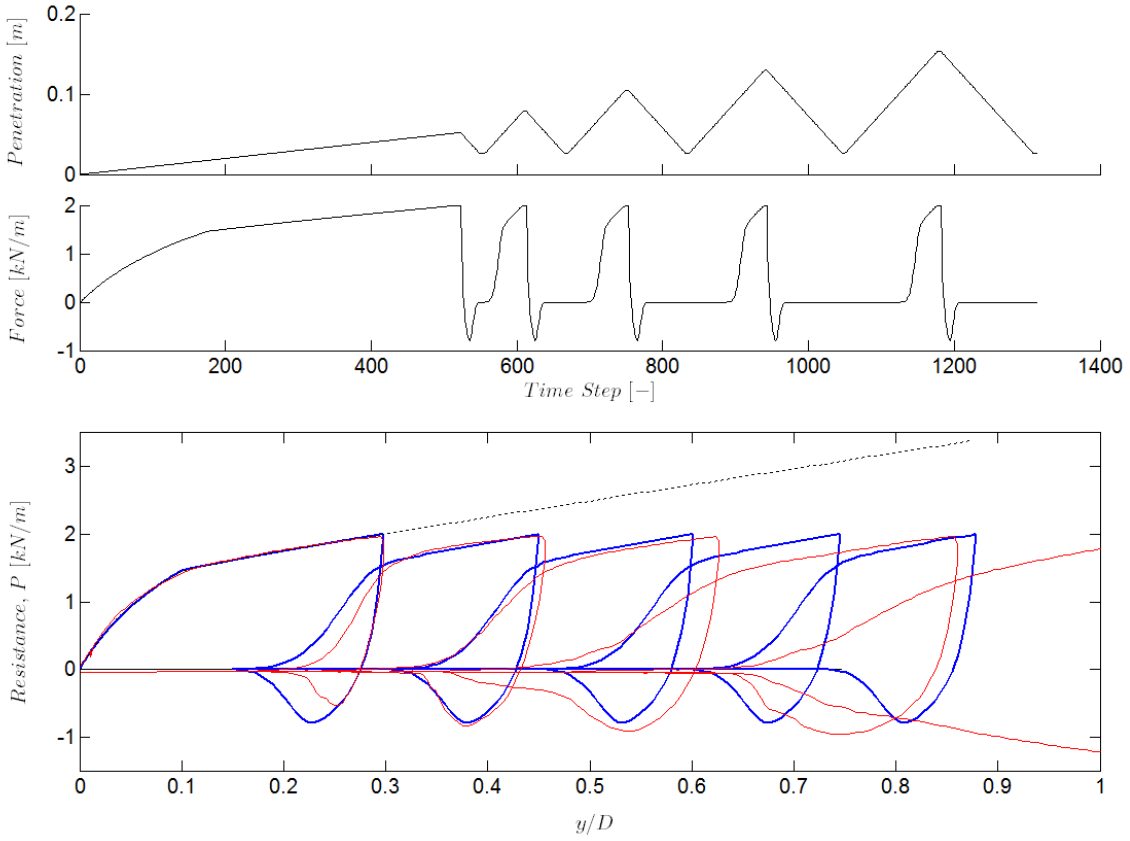

Fig. 80. Simulation for Hybrid Test (NGI-4)

b. Displacement Controlled Test

Figure 81 show model simulation under the same loading history as a displacement controlled test. After initial penetration to 0.3D, the pipe is subjected to a series of 100 cycles (stage C on day 1 in Table 8). The cyclic displacement amplitude is approximately 4 mm (0.02D). The simulation the same input parameters as earlier agree comparatively well with test data and shows degrading effects. Similarly to model test data, model simulation shows continuous force reduction during cyclic loading.

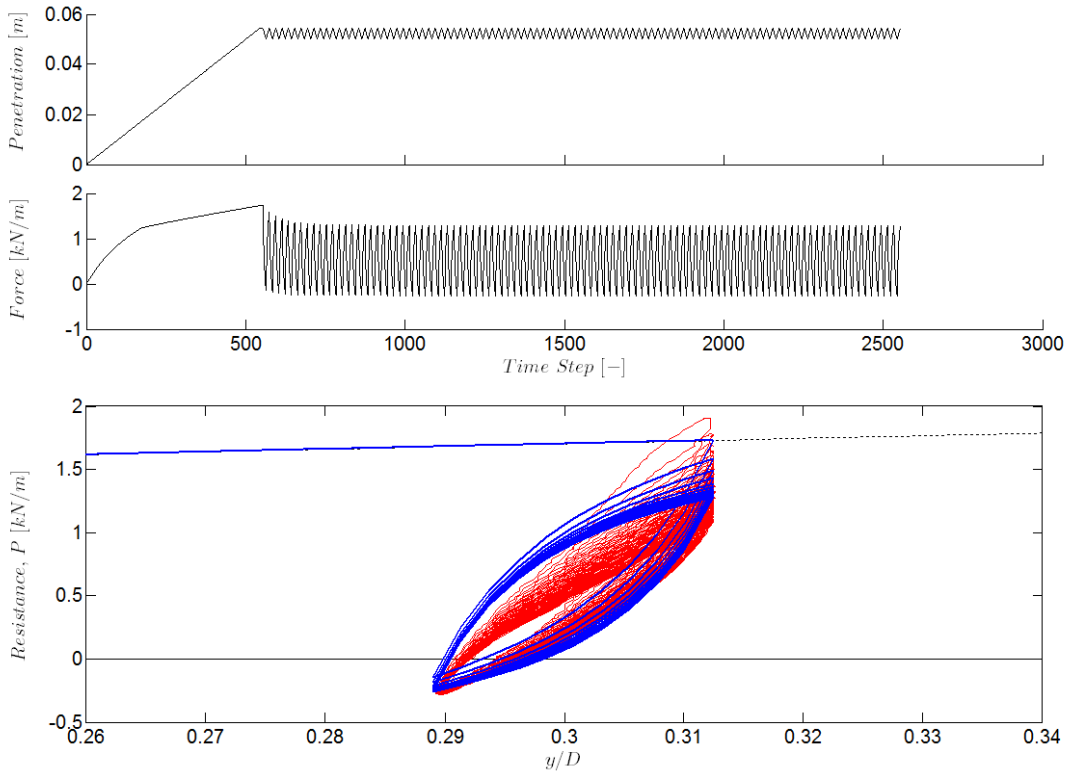

Fig. 81. Simulation for Displacement Controlled Test (NGI-3)

c. Load Controlled Test

Figure 82 illustrates model simulation under the loading history of a force controlled test (stage b on day 1 in Table 7). Initially, the pipe was penetrated monotonically to about 0.3D at a rate of 0.05 mm/s, at which soil resistance developed to 2000 N. Then, 30 cycles of loading were applied with load range of 2000N to -200N (ΔP=2200N). Model simulation shows acceptable results when comparing with test data. After 30 cycles of loading, the maximum penetration depth is almost same. Maximum penetration depth increases with number of cycles, however, the increased penetration per cycle decreases with cycles.

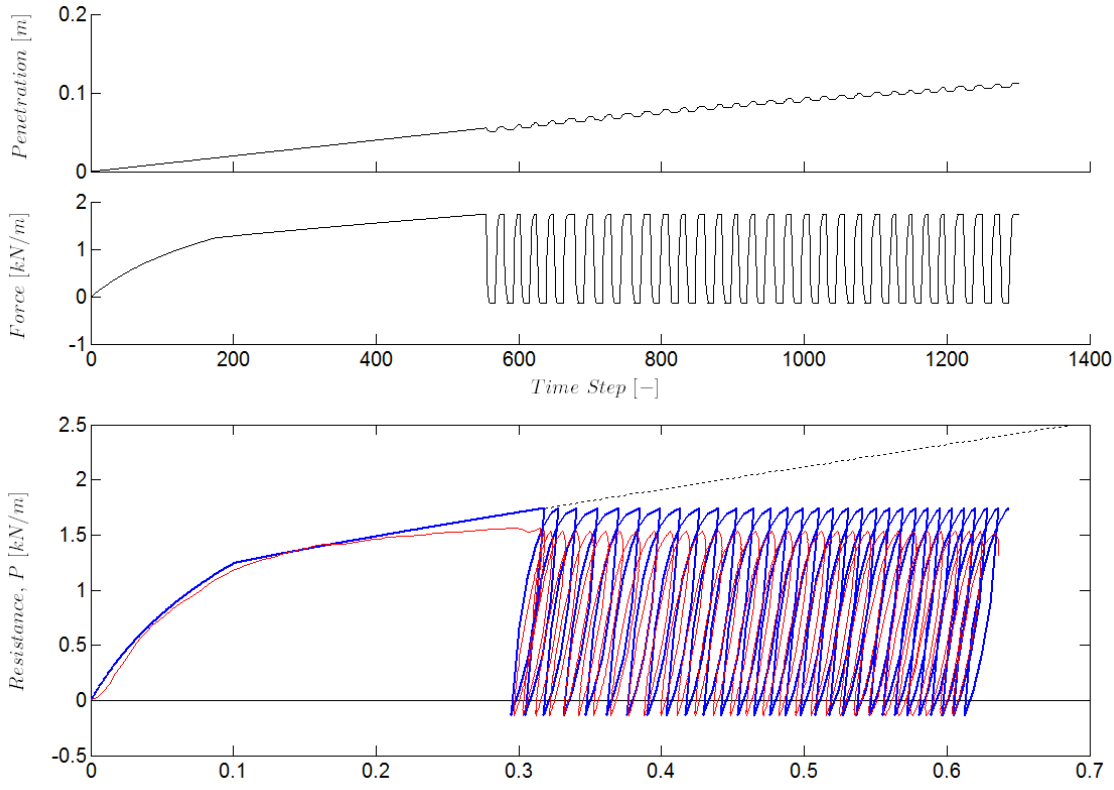

Fig. 82. Simulation for Force Controlled Test (NGI-2)

4.5.2. COFS Test

Figure 83 shows the comparison between the simulation by the proposed model and hybrid model test conducted at COFS. A model pipe with diameter of 25 mm and length of 125 mm was tested on kaolin with mudline strength of 3.7 kPa and a strength gradient of -0.0029 kPa/mm. After the model pipe was embedded to 21 mm ($\sim$0.8D), cyclic loads were applied at depths 72 mm ($\sim$2.8D) and 122 mm ($\sim$6D). During the test, the penetration rate was 0.1 mm/sec to maintain undrained conditions. While the model pipe in the first unload was uplifted until it became detached from the soil, the model pipe in the second unload did not fully separate.

Under input parameters detailed in table 12, model simulation show relatively good matching with test data. Maximum uplift load and suction release distance is not a fit with data. It is possible that the sidewall of the trench and debris on the pipe resulted in a higher maximum uplift force and longer suction release distance.

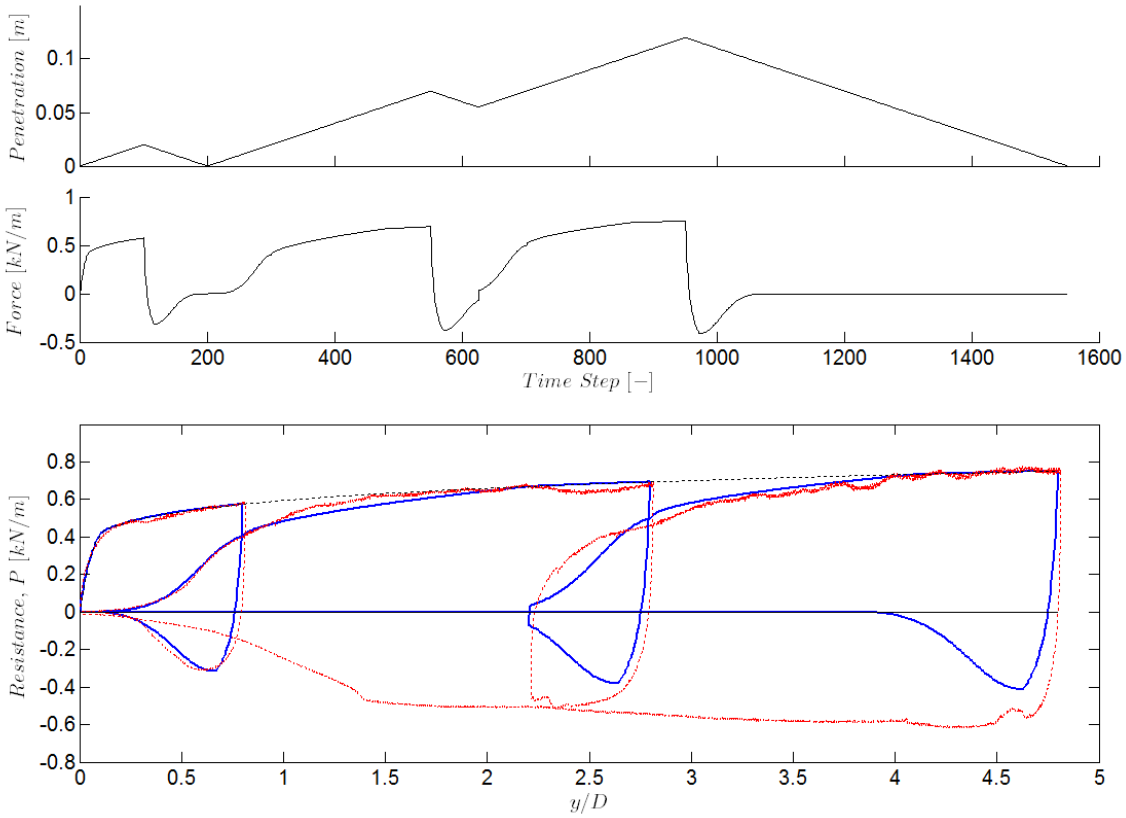

Fig. 83. Simulation for Force Controlled Test (NGI-2)

Table 12. Model Parameters for COFS Test in Figure 83

Parameter	Symbol	Value
Pipe diameter [m]	D	0.025
Mudline shear strength [kPa]	S_{uo}	3.7
Shear strength gradient [kPa/m]	S_g	0
Loading velocity [mm/s]	v	0.1
Power law coefficient	a	7.9
Power law exponent	b	0.15
Initial stiffness	k_0	1200
Maximum uplift load	ω	1.0
Uplift load limit	ϕ	0.55
Breakout	ψ	5.0
Re-penetration	α	1.5
Re-penetration	β	0.25
Degrading rate	μ	0.01
Degrading rate	ϵ	0.45
Initial load drop	Ω	0.3

CHAPTER V

SEABED-RISER INTERACTION MODEL

5.1. General

Two general approaches to the problem of soil-riser interaction are available. One idealization treats the soil as a continuum and uses various methods, boundary integrals, finite elements etc., to solve the governing equations. While this method seems to be the 'most correct' in principle, it has some drawbacks when it comes to design applications. If realistic soil models and complicated geometrics are incorporated, the approach quickly encounters mathematically intractable problem. It is useful for research studies and basic for substantive advancements in understand.

A simpler method involves dealing with the soil as uncoupled springs called a "Winkler Foundation". This method is so simple mathematically to handle significant complexities with ease. This approach relies heavily on development of empirical rules based on experimental and analytical studies. The latter method will be used in the seafloor-riser interaction problem. Thus the riser will be considered as an elastic beam-column with property (EI) and the shear deformation of riser will be neglected. Also, the seafloor will be assumed the soil to be uncoupled springs distributed along the length of the pipe.

Simple approach for solving riser-seabed interaction problem is using analysis method of beam on elastic foundation. Although many different techniques (Hetényi and of Michigan, 1946; Beaufait and Hoadley, 1980) has been applied to the analysis of a elastic beam supported on a linear elastic foundation and subjected to lateral loads, the basic differential equation describing the deflection curve of a beam is

$$\frac{d^2}{dx^2}\left[EI\frac{d^2y}{dx^2}\right] + T\frac{d^2y}{dx^2} + k_s y = w \tag{5.1}$$

where y defines the deflection of the beam, EI is the rigidity for the beam, T is the axial load applied to the beam, w is the applied distributed load on the beam and k_s is the foundation modulus. Note that w has units of F/L and represents the force per infinitesimal unit length dx. The parameter k_s is a proportionality constant relating w to the vertical displacement y, so k_s must have units of F/L^2.

The solution for this governing equation (5.1) of bending for a beam supported on an elastic foundation is complicated by the applied loads, both T and w and the foundation modulus k_s. This problem is more complicated if the foundation behavior is nonlinear. The problem is further complicated if the seafloor supporting the riser behaves nonlinearly. The nonlinear load-deflection relationship for seabed use the P-y model developed in chapter 4. Hence, the foundation modulus, k_s, of eqn 5.1 becomes a nonlinear coefficient.

This differential equation can be solved with boundary conditions specified at two different boundary values at each ends of numerical domain, x = 0 and L. One mean of solving two-point boundary value problems is the finite difference method, where the differential equations are approximated by finite differences at evenly spaced mesh points. As a consequence, a differential equation is transformed into set of simultaneous algebraic linear equations by the central difference equations with the given boundary constraints. For solving this nonlinear equations, iterative procedures need reasonably good starting values in order to converge to excessive computational effort.

This chapter includes the analytical framework of the numerical model considering the riser-seabed interaction problem. The interaction model involves the limited domain, from touchdown zone to riser anchor.

5.2. Governing Differential Equation

The analytical framework utilized in this study considers the riser-seafloor interaction problem in terms of a pipe resting on seabed. The following non-linear, fourth-order ordinary differential equation 5.2 governs this system:

$$EI\frac{d^4y}{dx^4} + T\frac{d^2y}{dx^2} = w - P_s \tag{5.2}$$

where E, I and T are elastic modulus, moment of inertia, and axial tension of the pipe, respectively. w and P_s are riser self-weight and reaction force of soil response to external force. The term y denotes an displacement from a starting reference configuration. Although the tension T in the riser is also a function of x, the proposed interaction model considers the tension as constant, effectively assuming that the soil exerts no resistance to motion parallel to the length of the riser.

In most numerical analysis on foundation model, soil reaction is expressed by series of elastic springs (Fig. 85). The soil stiffness $k_s(x)$ is characterized by non-linear load-deflection (P-y) model which involves degradation due to repeated vertical loading. Therefore, the Eq. 5.2 is rewritten as:

$$EI\frac{d^4y}{dx^4} + T\frac{d^2y}{dx^2} = w - (P + k_s\Delta y) \tag{5.3}$$

where P is current soil reaction force and Δy is difference between riser deflection and current soil depth deformed by previous loading, $(y - y_s)$. Again, arranged expression on eq. 5.3 is

$$EI\frac{d^4y}{dx^4} + T\frac{d^2y}{dx^2} + k_s y = w - P_s + k_s y_s \tag{5.4}$$

The complete riser problem, extending from the seafloor to the platform at the water

surface, is inherently a large deformation problem. However, within the touchdown zone, vertical deflections on the order of 3 to 4 pipe diameters occur over a horizontal distance of several hundred diameters (**?**Willis and West, 2001). The relative magnitude of horizontal to vertical deflection is sufficiently small to justify the use of small-strain, small-deflection beam theory implicit in eqn 5.2 when evaluating riser interaction effects within the touchdown zone.

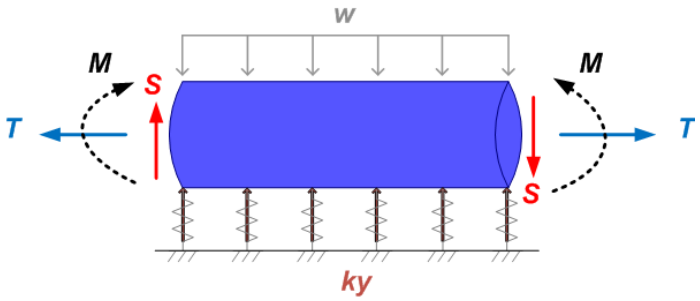

Fig. 84. Sign Conventions

Figure 84 illustrates the sign conventions for deflection, shear force and bending moment used in this chapter. The beam is assumed to be positioned in the frame of a set of right-handed, orthogonal axes with the x-axis defining the longitudinal axis of the beam. Both applied loads and internal actions are shown in their assumed positive sense.

Fig. 85 illustrates the boundary conditions for the riser-seafloor interaction model. In the far field (B in Fig. 85), the specified boundary conditions are no displacement and a horizontal tangent, or no slope:

$$\begin{aligned} y(L) &= y_{sw} \\ y'(L) &= 0 \end{aligned} \tag{5.5}$$

where L is the length of pipe. For Eq. 5.5 to be valid, the length L used in the analysis must be sufficiently large for the shear $V(L)$ and moment $M(L)$ to become negligible. At the touchdown point (A in Fig. 85), a specified vertical (uplift or lay-down) displacement, u_{yA}, is applied and a moment is also mobilized due to the tension in the pipe. Therefore, the two remaining conditions required for the solution of Eq. 5.2 are:

$$\begin{aligned} y(0) &= u_{yA} \\ y''(0) &= -\frac{u_{yA}T}{EI} \end{aligned} \tag{5.6}$$

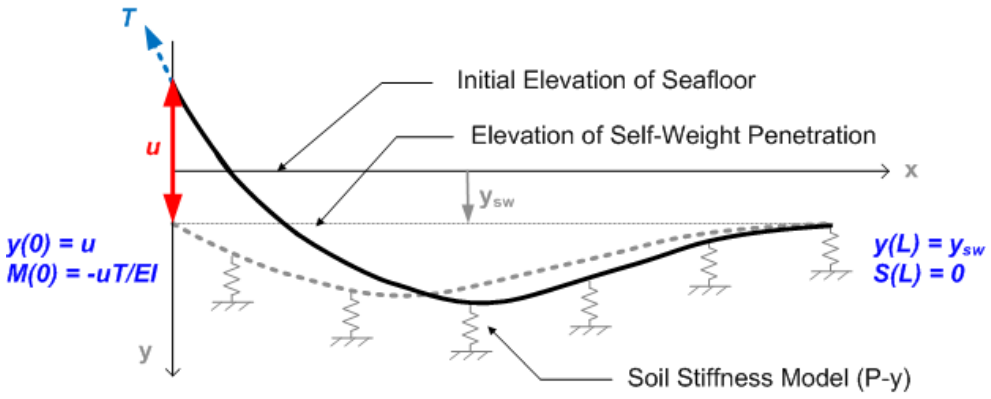

Fig. 85. Seafloor-Riser Interaction Model

5.3. Numerical Solution for the Fourth-Order Differential Equation

The governing equation (Eq. 5.2) is a non-linear, fourth-order ordinary differential equation. The soil stiffness (k_s) is described by the load-deflection (P-y) curves. The solution domain is divided into N-1 intervals of length h each. In terms of central differences, substitution of the derivatives of y given by equation 5.2 gives

$$(y_{i-2} - 4y_{i-1} + 6y_i - 4y_{i+1} + y_{i+2}) + \frac{Th^2}{EI}(y_{i-1} - 2y_i + y_{i+1}) + \frac{k_{si}h^4}{EI}(y_i - y_{si}) = \frac{(w_i - P_{si})h^4}{EI} \tag{5.7}$$

We can rearrange this expression to read

$$y_{i-2} + (\alpha - 4)y_{i-1} + (6 - 2\alpha + \beta_i)y_i + (\alpha - 4)y_{i+1} + y_{i+2} = \gamma_i \tag{5.8}$$

Where $\alpha = \frac{Th^2}{EI}$, $\beta_i = \frac{k_{si}h^4}{EI}$, $\gamma = (w_i - P_{si} + k_{si}y_{si})\frac{h^4}{EI}$ and $i = 1, 2, \cdots, n$ (include two boundary points). It is more revealing to write these equations as

$$\begin{aligned}
y_{-1} + (\alpha - 4)y_0 + (6 - 2\alpha + \beta_1)y_1 + (\alpha - 4)y_2 + y_3 &= \gamma_1 \\
y_0 + (\alpha - 4)y_1 + (6 - 2\alpha + \beta_2)y_2 + (\alpha - 4)y_3 + y_4 &= \gamma_2 \\
\vdots \qquad\qquad\qquad\qquad\qquad\qquad &= \vdots \\
y_{n-3} + (\alpha - 4)y_{n-2} + (6 - 2\alpha + \beta_{n-1})y_{n-1} + (\alpha - 4)y_n + y_{n+1} &= \gamma_{n-1} \\
y_{n-2} + (\alpha - 4)y_{n-1} + (6 - 2\alpha + \beta_n)y_n + (\alpha - 4)y_{n+1} + y_{n+2} &= \gamma_n
\end{aligned} \tag{5.9}$$

We now see that there are four unknowns that lie outside the solution domain: y_{-1}, y_0, y_{n+1} and y_{n+2}. These can be eliminated by applying the two boundary conditions prescribed at each end of the solution domain, a task that is facilitated by Table 13. The

finite difference expressions of the boundary conditions at the near field (TDP) are

(Rotation)

$$\begin{aligned} y(0) = y_{sw} \quad &\rightarrow \quad y_1 = y_{sw} \\ y'(0) = \theta \quad &\rightarrow \quad y_0 = y_2 + 2h\theta \end{aligned} \tag{5.10}$$

(Displacement)

$$\begin{aligned} y(0) = u \quad &\rightarrow \quad y_1 = u \\ y''(0) = -\frac{uT}{EI} \quad &\rightarrow \quad y_0 = (2-\alpha)u - y_2 \end{aligned} \tag{5.11}$$

Also, the boundary conditions for the far field can be expressed as

$$\begin{aligned} y(L) = y_{sw} \quad &\rightarrow \quad y_n = y_{sw} \\ y'(L) = 0 \quad &\rightarrow \quad y_{n+1} = y_{n-1} \end{aligned} \tag{5.12}$$

Table 13. Equivalent Finite Difference Expression on BC

Boundary Condition	Equivalent finite difference expression
$y(a) = \alpha$	$y_1 = \alpha$
$y'(a) = \alpha$	$y_0 = y_2 + 2h\alpha$
$y''(a) = \alpha$	$y_0 = 2y_1 - y_2 + h^2\alpha$
$y'''(a) = \alpha$	$y_{-1} = 2y_0 - 2y_2 + y_3 + 2h^3\alpha$
$y(b) = \beta$	$y_n = \beta$
$y'(b) = \beta$	$y_{n+1} = y_{n-1} + 2h\beta$
$y''(b) = \beta$	$y_{n+1} = 2y_n - y_{n-1} + h^2\beta$
$y'''(b) = \beta$	$y_{n+2} = 2y_{n+1} - 2y_{n-1} + y_{n-1} + 2h^3\beta$

Considering again the finite difference expression of the boundary conditions gives the following nonlinear system (for rotational).

$$\begin{aligned}
y_1 &= y_{sw} \\
(\alpha-4)y_1 + (7-2\alpha+\beta_2)y_2 + (\alpha-4)y_3 + y_4 &= \gamma_2 - 2h\theta \\
y_1 + (\alpha-4)y_2 + (6-2\alpha+\beta_3)y_3 + (\alpha-4)y_4 + y_5 &= \gamma_3 \\
\vdots &= \quad \vdots \\
y_{n-3} + (\alpha-4)y_{n-2} + (6-2\alpha+\beta_{n-1})y_{n-1} + (\alpha-4)y_n &= \gamma_{n-1} \\
y_n &= y_{sw}
\end{aligned} \tag{5.13}$$

And (for Displacement)

$$\begin{aligned}
y_1 &= u \\
(5-2\alpha+\beta_2)y_2 + (\alpha-4)y_3 + y_4 &= \gamma_2 + (\alpha-2)u \\
\vdots &= \quad \vdots \\
y_{n-3} + (\alpha-4)y_{n-2} + (6-2\alpha+\beta_{n-1})y_{n-1} + (\alpha-4)y_n &= \gamma_{n-1} \\
y_n &= y_{sw}
\end{aligned} \tag{5.14}$$

The remaining n points in solution domain can be recast as a matrix problem,

$$[K][Y] = [R] \tag{5.15}$$

For rotational loading,

$$\begin{bmatrix} 1 & 0 & 0 & \dots & & & & \\ \alpha-4 & 7-2\alpha+\beta_2 & \alpha-4 & 1 & & & & \\ 1 & \alpha-4 & 6-2\alpha+\beta_3 & \alpha-4 & 1 & & & \\ & \ddots & \ddots & \ddots & & & & \\ & & 1 & \alpha-4 & 6-2\alpha+\beta_{n-2} & \alpha-4 & 1 & \\ & & & 1 & \alpha-4 & 7-2\alpha+\beta_{n-1} & \alpha-4 & \\ & & \dots & 0 & 0 & 0 & 1 & \end{bmatrix} \begin{bmatrix} y_1 \\ y_2 \\ y_3 \\ \vdots \\ y_{n-2} \\ y_{n-1} \\ y_n \end{bmatrix} = \begin{bmatrix} y_{sw} \\ \gamma_2-2\theta \\ \gamma_3 \\ \vdots \\ \gamma_{n-2} \\ \gamma_{n-1} \\ y_{sw} \end{bmatrix} \tag{5.16}$$

and displacement loading

$$\begin{bmatrix} 1 & 0 & 0 & \dots & & & & \\ \alpha-2 & 5-2\alpha+\beta_2 & \alpha-4 & 1 & & & & \\ 1 & \alpha-4 & 6-2\alpha+\beta_3 & \alpha-4 & 1 & & & \\ & \ddots & \ddots & \ddots & & & & \\ & & 1 & \alpha-4 & 6-2\alpha+\beta_{n-2} & \alpha-4 & 1 & \\ & & & 1 & \alpha-4 & 7-2\alpha+\beta_{n-1} & \alpha-4 & \\ & & \dots & 0 & 0 & 0 & 1 & \end{bmatrix} \begin{bmatrix} y_1 \\ y_2 \\ y_3 \\ \vdots \\ y_{n-2} \\ y_{n-1} \\ y_n \end{bmatrix} = \begin{bmatrix} u \\ \gamma_2+\alpha u \\ \gamma_3 \\ \vdots \\ \gamma_{n-2} \\ \gamma_{n-1} \\ y_{sw} \end{bmatrix} \tag{5.17}$$

We encounter penta-diagonal (bandwidth=5) coefficient matrices in the solution of fourth-order, ordinary differential equations by finite differences. Thus the solution of matrix [Y] can be found by a direct solution of the linear system of equations.

5.4. Numeric Algorithm

The flow chart (Fig. 86) summarizes the process used for the simulation of the seafloor-riser interaction by solving Eq. 5.3 iteratively for each loading increment. The first step of the analysis is the computation of the self-weight penetration (y_{sw}) of the undeformed riser. The initial self-weight penetration calculation proceeds by simply equating pipe weight w to the collapse load of a pipe embedded in a trench (Aubeny et al., 2005). The self-weight penetration depth effectively established the far-field vertical coordinate of the pipe. The pipe configuration at the touchdown point to initiate an analysis is a matter of some uncertainty at this point in time. However, existing observational data do provide a basis for establishing initial conditions. For example, observations have shown maximum riser pipe embedment within the touchdown zone to be in the range of about 3-4 pipe diameters (Willis and West, 2001; **?**). Solution of governing equation with an imposed contact angle θ at the touchdown point to achieve a target maximum trench depth appears to provide a reasonable basis for establishing an initial riser configuration. For both the self-weight penetration and the initial pipe configuration calculations are based on a purely plastic model of soil resistance shown in figure 87.

The uplift-laydown movements (Fig. 88), the second step of the sequence described above, impose subsequent motions at the touchdown point. The governing differential equation (Eq. 5.2) is solved using nonlinear finite difference analysis given the boundary conditions in Eqns. 5.5-5.6. The derivative terms in equations 5.2 and 5.5-5.6 are approximated using first order central differences.

Solution for the approximating set of nonlinear algebraic equations (Eq. **??**) require iterative process. The deflected shape of the riser is a function of the load acting on the riser and the load is a nonlinear function of the deflection of riser and the supporting seabed. A solution to this nonlinear problem is sought through a systematic modification of the seabed

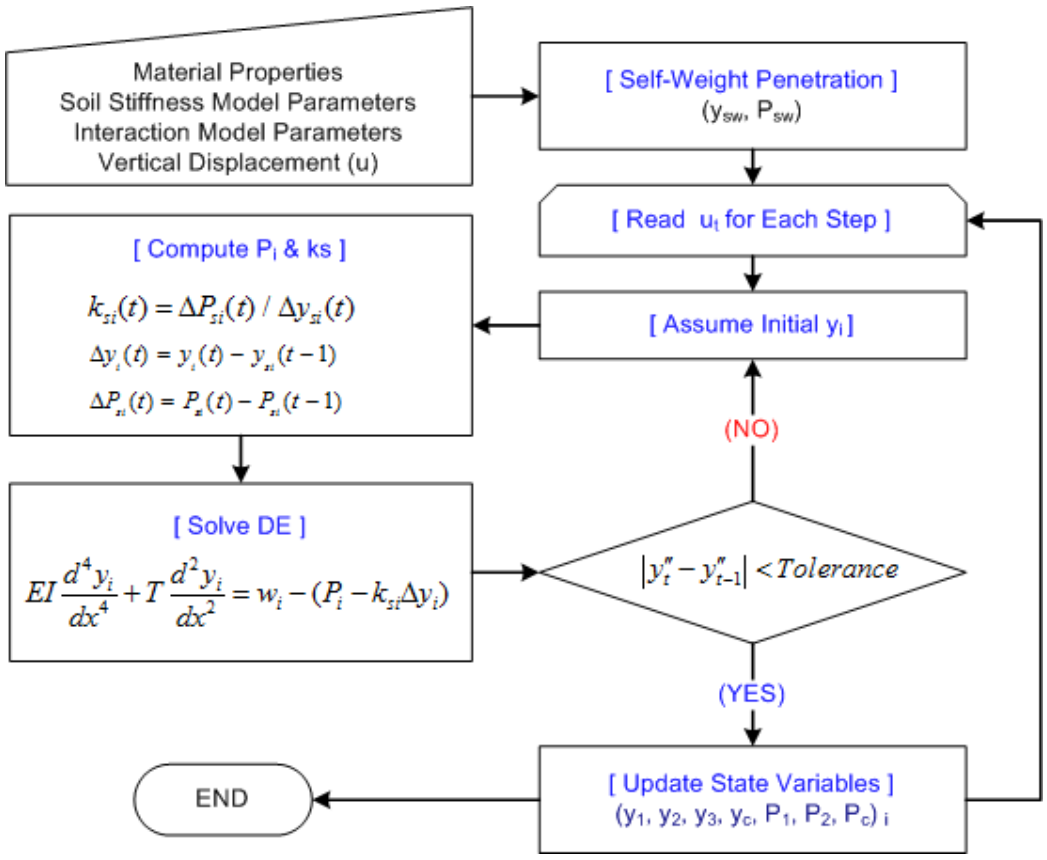

Fig. 86. Flow Chart for the Solution Procedure for the Seafloor-Riser Interaction Simulation

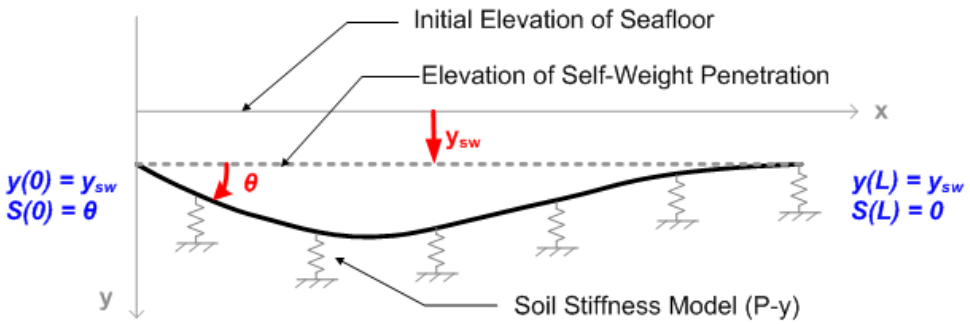

Fig. 87. Initial Penetration

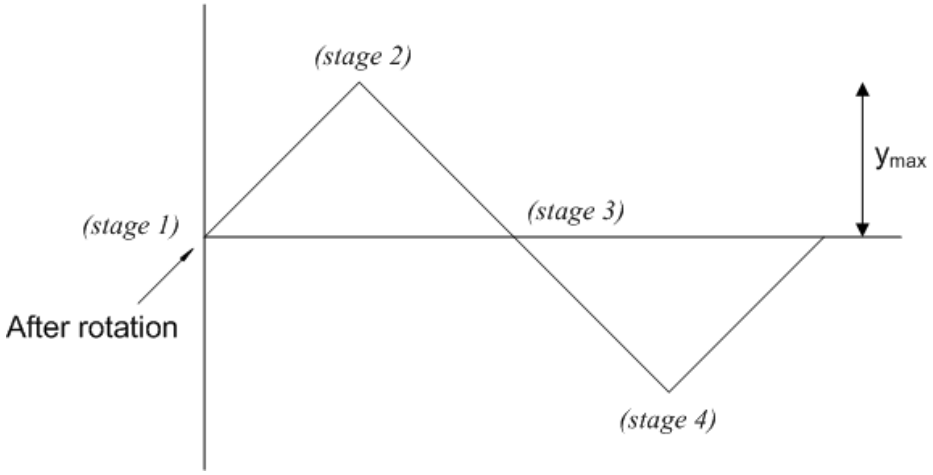

Fig. 88. Vertical Displacement Imposed at the Touchdown Point

modulus, using the familiar secant approach, until both compatibility and equilibrium are satisfied. In utilizing the difference method to analyze the beam, the supporting seabed can be modeled as a spring of stiffness k_s.

The stiffness of the spring is a function of the displacement of the node. The nonlinear nature of the problem requires that an iterative approach be taken. Using the developed P-y curve in Chapter IV to model the load-displacement response of the seabed, all seabed springs are assumed to be initially active by self-weight penetration of riser and to have a stiffness equal to the slope, k_s, of the first node of the load-displacement relationship in the first iteration of the analysis. Once the beam has been analyzed, the next increment of riser displacement at touchdown point is applied to the governing equation, and the displacement of the point of each real node attached to a seabed spring is checked to determine if the spring is in tension (negative deflection) or in compression. This process is repeated until moment difference between current and previous steps is less than given tolerance. Because of the non-linearity of the soil response, the current linearized stiffness, k_s, must be estimated iteratively until the newly computed displacements y are sufficiently close to the value of y assumed at the beginning of the iteration. From the standpoint of fatigue life, a primary consideration is the bending moment. Hence, the computed curvature (y'') is used as the convergence criterion:

$$|y''_t - y''_{t-1}|_{max} < \text{Tolerance} \tag{5.18}$$

In this study, 10^{-5} was adopted as tolerance. Most convergence is typically achieved in less than 20 iterations.

5.5. Validation of Formulation

The following sections briefly describe a series of simulations to illustrate the capabilities of the seafloor-riser interaction model with the new degrading non-linear soil springs. The examples are not trying to replicate an existing site or observed conditions. Rather, the material parameters are selected to represent a generic soil with realistic properties for illustration purposes to highlight the capabilities of the model.

Analyses were performed for the test case of a hypothetical soft seafloor site having a soil mudline strength S_{uo} = 3 kPa and strength gradient S_{ug} = 1.3 kPa/m. The riser pipe under consideration is steel (E = 1.93x108 kPa), with a diameter D = 0.15 m and wall thickness t = 0.69 cm. A trench length of 100 m is used in the analysis. Based on laboratory model tests in kaolin conducted by NGI (Langford and Aubeny, 2008), The soil stiffness model parameters (ω, ϕ, ψ) and the parameters (a, b) associated with backbone curve are determined for the analysis. All input parameters mentioned above are listed in Table 14.

In finite difference analysis, the number of nodes and the number of steps to maximum vertical displacement effect on simulation results. For determination of reasonable values for dx and du before example simulation, the test simulation with the riser and seabed properties in Table 14 is accomplished under one cyclic displacement loading (u_{max} = 1 m) at the left end of the riser. Figure 89 illustrates the effect of mesh refinement and number of time step to reach maximum vertical displacement (u_{max}). The maximum moments in riser pipe is start to stabilize around dx = 0.5 and du = 0.01 to be used as interaction model parameters.

The initial maximum depth of the trench imposed by self-weight penetration and rotational loading at the touchdown point is estimated to be 0.3 m ($\sim$2D). The riser weight per unit area is calculated assuming a pipe full of water. Ten cycles of a triangular wave with

Table 14. Model Parameters for Example in Figure 66

Type	Parameter	Symbol	Value
Material	pipe length	L	$100\,m$
	pipe diameter	D	$0.15\,m$
	pipe modulus	E	$1.93e8\,kPa$
	pipe thickness	t	$0.0069\,m$
	mudline shear strength	S_{uo}	$3.0\,kPa$
	shear strength gradient	S_g	$1.3\,kPa/m$
	loading velocity	v	$0.05\,mm/s$
Bounding Loop	power law coefficient	a	6.8
	power law exponent	b	0.12
	initial stiffness	k_0	1200
	maximum uplift load	ω	0.75
	uplift load limit	ϕ	0.35
	breakout	ψ	1.3
Degrading	re-penetration	α	0.7
	re-penetration	β	0.25
	degrading rate	μ	0.01
	degrading rate	ϵ	0.43
	Initial load drop	Ω	0.23
Interaction	number of node	$n\,(dx)$	$201\,(0.5\,m)$
	maximum iteration	$-$	100
	tolerance	η	0.00001
	axial tension	T	$100\,kN$
	rotational restraint	θ	$0.04\,kNm/rad$

are selected as the forcing function, as shown in Fig. 90. In these simulations, the riser is always uplifted at the left boundary, never actually forced into the soil. A constant riser tension T = 100 kN is also imposed at the left boundary.

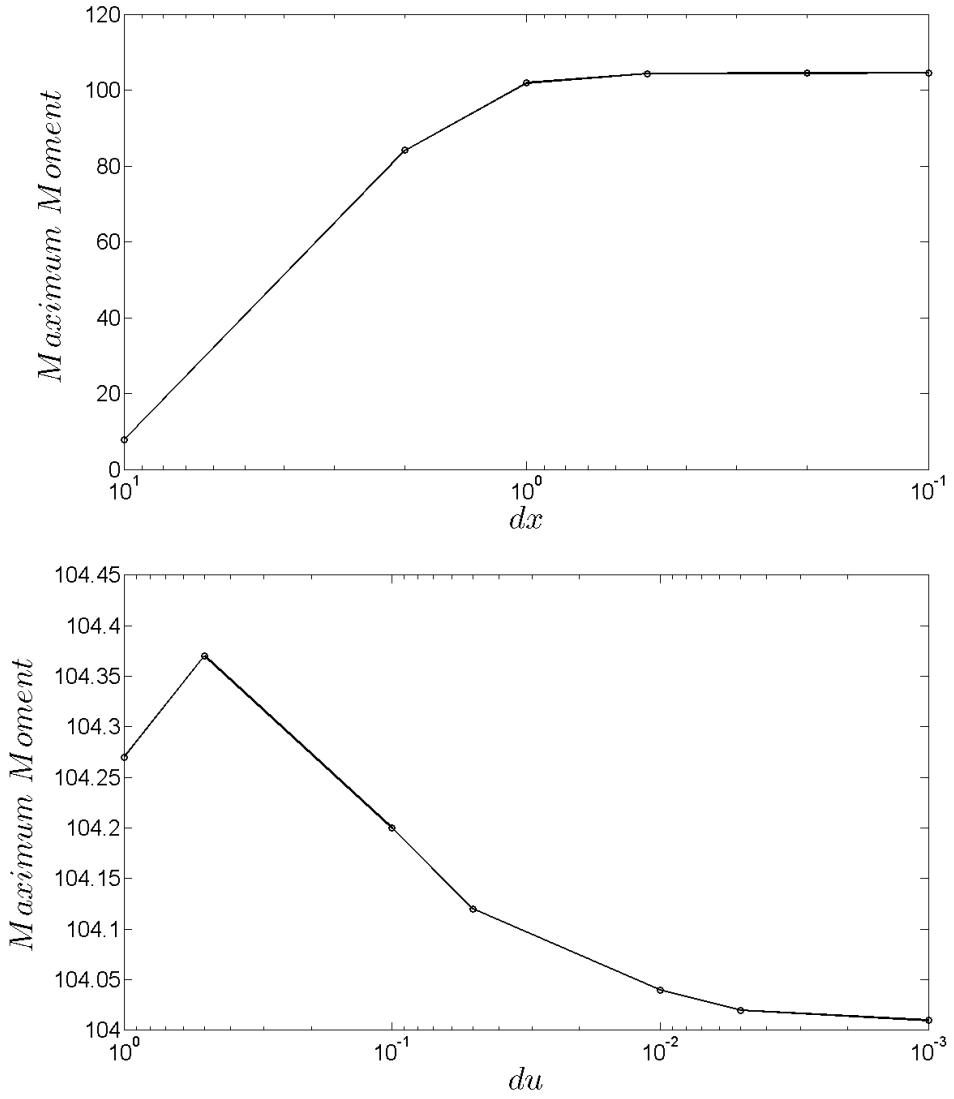

Fig. 89. Variation of Nodal Density and Time-Step

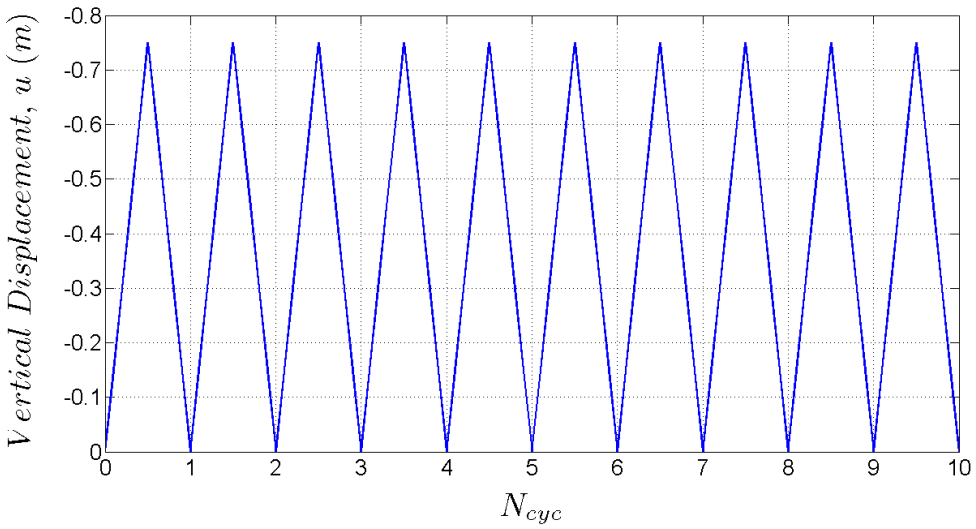

Fig. 90. Vertical Displacement Loading History

5.5.1. Riser Deflections

Figure 91(a) shows the profile of deflections along the riser in the first cycle of loading for the level of excitation with maximum u of $2.5D$. Although the total length of the riser in the simulation is 100 m, the results are displayed only up to 20 m to focus on the area where the range of the motion is appreciable. Only a small selection of the actual calculation steps is shown in the figure 91. As the riser end point is uplifted, the pipe bends with increasing curvature and penetrates further into the soil, at least along a portion of its length. As the end motion reverses and the riser is laid down, the curvature is not eliminated because the penetration in the previous half-cycle is only partially reversed. The same trend can be seen in all cycles analyzed.

The deflection profiles for each half cycle at the maximum uplift and lay-down for u_{max} of $2.5D$ is presented (b) and (c) in Figs. 91, respectively. The riser continues to penetrate during uplift as the cyclic loading progresses, although the rate of penetration decreases with increasing number of cycles. The rate of stiffness degradation depends on the logarithm of the accumulated deflections; therefore it slows down as the cycling continues. Eventually, the incremental deepening of the trench will become negligible and the trench will stabilize.

In this example, the strength of the soil is increasing with depth at a rate of 1.3 kPa/m. Therefore, as the riser digs itself down into the soil with each new cycle of loading, it is also reaching areas of increased resistance to penetration. At a certain depth, the soil resistance has increased enough for the equilibrium conditions expressed by Eq. 5.2 to result in a shift of the deeper point of the riser to the left. The soil at this new maximum penetration point is initially softer, although it has not suffered as much cyclic degradation. At the same time the maximum penetration location moves right on the riser, the curvature decreases. As the point of maximum penetration migrates right and the curvature decreases, the effect of the

continued cyclic loading becomes less and less pronounced and the trench will eventually stabilize. The combination of strength increase with depth and stiffness degradation with cyclic loading increases the non-linearity of the problem, but it also produces more realistic results, matching observations of risers' behavior.

Fig. 92 shows the load-deflection (P-y) curve for the specific locations. During cyclic loading, the bounding loops moves toward further depth and the loops on four different locations are finally stabilized.

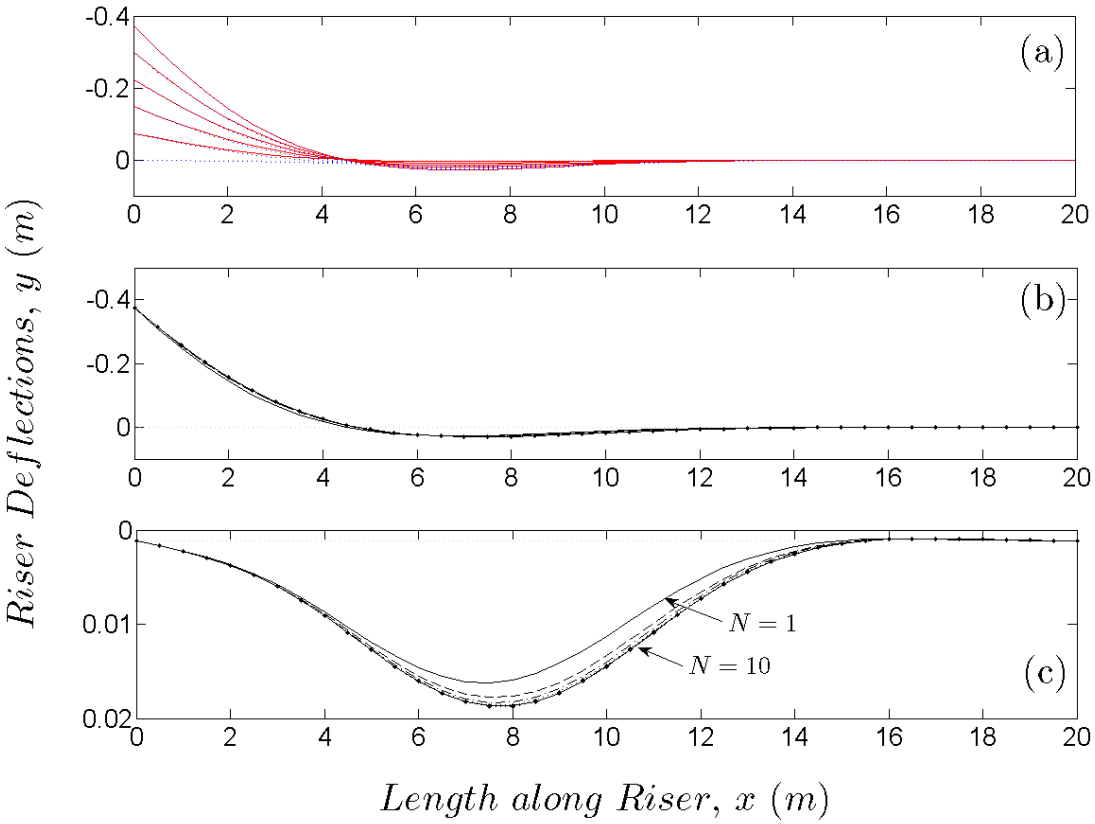

Fig. 91. Riser Configurations for u_{max} = 2.5D : (a) During First Cycle, (b) at Each Half–Cycle for Maximum Uplift for 10 Cycles (c) at Each Half-Cycle for Maximum Lay-Down for 10 Cycles

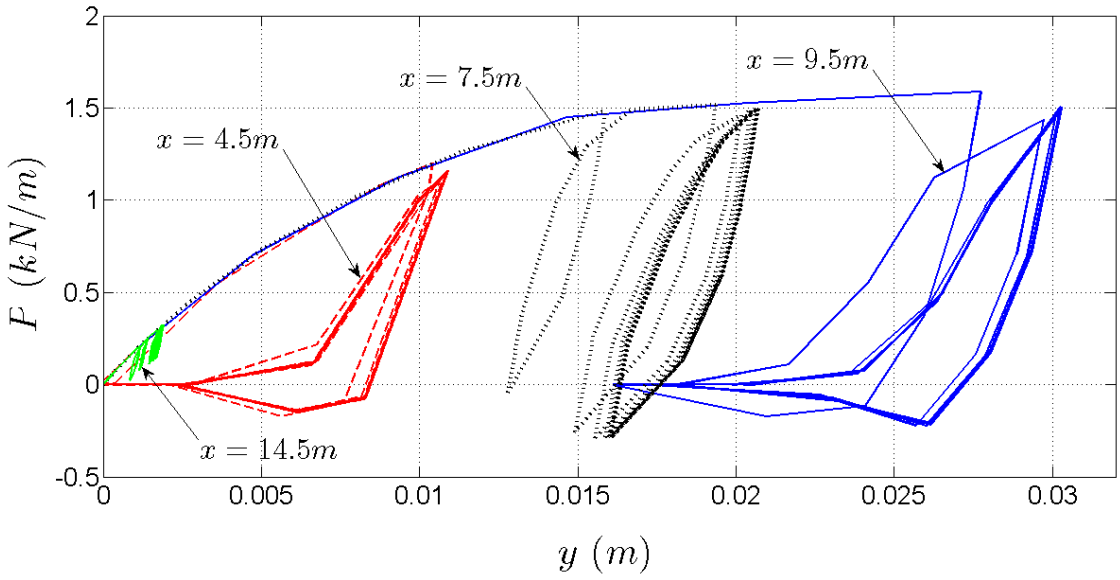

Fig. 92. P-y Curves at x = 4.5, 7.5, 9.5, and 14.5 m for u_{max} = 2.5D

5.5.2. Trench Formation

Fig. 93 illustrates the evolution of the trench shape during the 10 cycles of vertical loading for the case with u_{max} = 2.5D. The lines mark the trench shape for the deepest lay-down for each cycle. During the uplift movement, the soil nearer to the left boundary rebounds, since the riser is no longer in contact with it. Further along the riser, the depth of the trench is advanced at every cycle. The location of the maximum trench depth migrates slightly to the left with increasing number of cycles. The maximum trench depth increased from 0.02 m to 0.024 m during 10 cycles of loading. The location of the point of maximum trench depth moved towards the right boundary, or far field.

As observed earlier, the higher soil resistance due to the increasing strength with depth causes the point of maximum trench depth to shift away from the end of the riser at which the loading is applied. By introducing degradation of soil stiffness with cyclic loading, the seafloor-riser interaction model can simulate the development of a trench and the migration of the touchdown point.

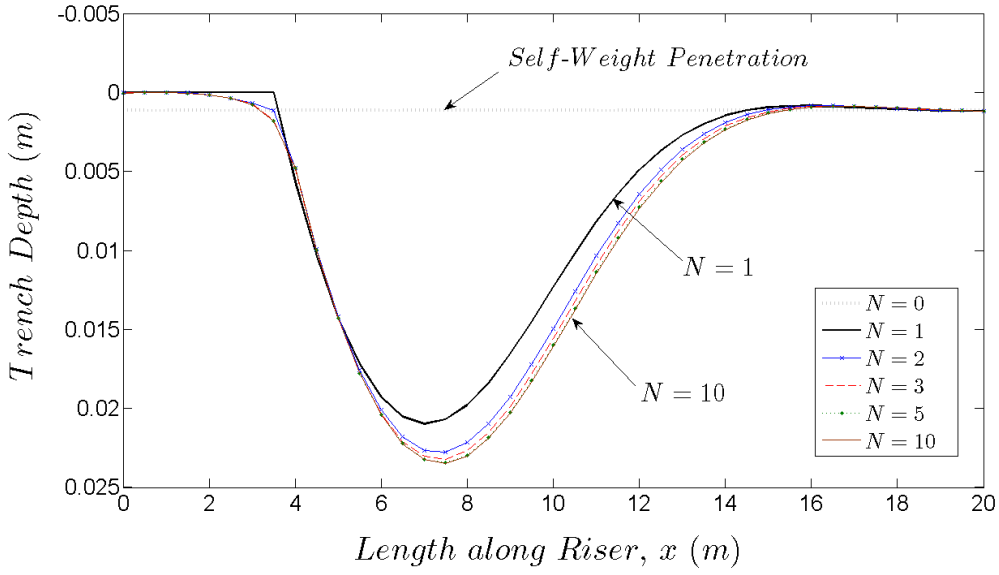

Fig. 93. Trench Evolution with Number of Cycles for u_{max} = 2.5D

5.5.3. Moment Variation

The (a) in Fig. 94 shows the bending moments along the riser during the first uplift and lay-down cycle for example simulation of u_{max} = 2.5D. As the riser is uplifted, the bending moment increases and the location of the maximum value slightly migrates rightward to about 2.5 m from the initial TDP. During the lay-down phase, the curvature of the pipe is smaller and this is reflected in a decrease of the bending moment, as well as a shift of the location of the maximum value. A summary of the maximum bending moments at each half cycle is shown (b) and (c) in Fig. 94. Initially, the moments decrease during each cycle both at the highest uplift and increase the lowest lay-down. The rate of increase and decrease is larger for first cycle. In the uplift, the maximum bending moment drops from about 35 kN-m in cycle 1 to about 28 kN-m in cycle 10, approximately a 20% decrement. As the point of maximum penetration shifts right, the curvature of the riser decreases and causes the maximum moment to drop.

Fig. 95 depicts the evolution of bending moment at various locations. The moment at a given point slightly increases or decreases as cyclic loading progresses and then stabilize after 10 cyclic loading. The moments variation per cycle at the locations near moving boundary are relatively larger than the moment change per cycle at the points of far field location.

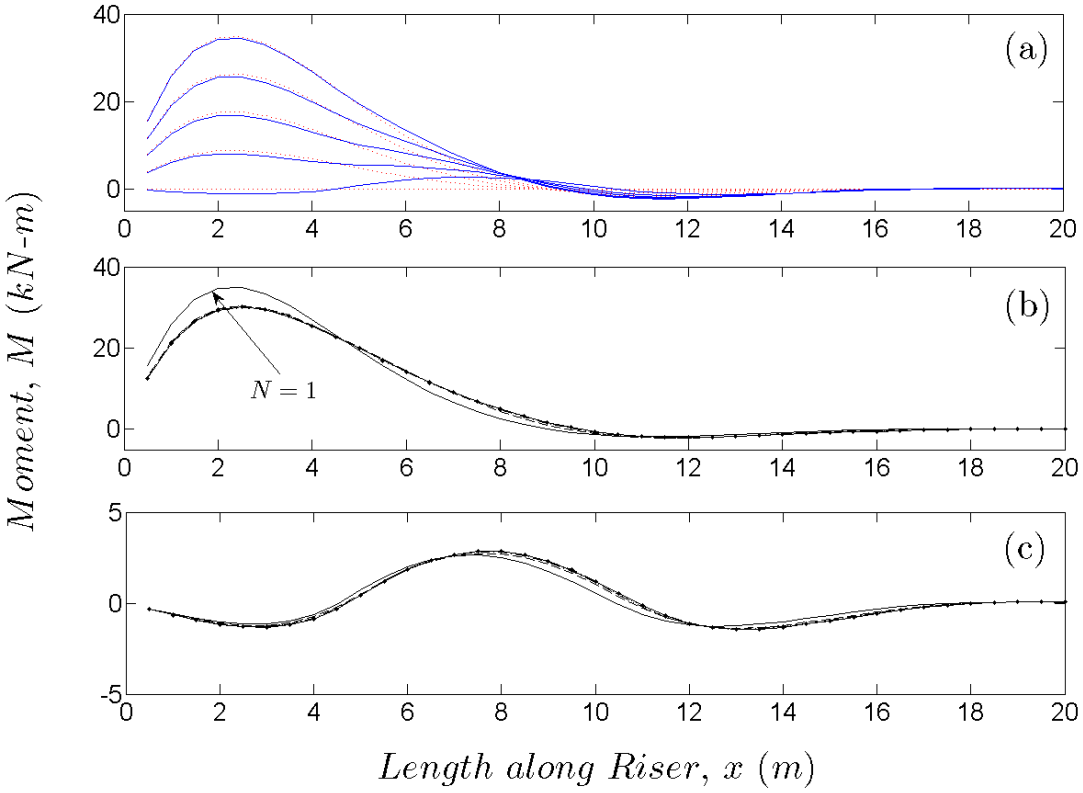

Fig. 94. Moment Variation along the Riser for u_{max} = 2.5D : (a) During First Cycle, (b) at Each Half-Cycle for Maximum Uplift for 10 Cycles (c) at Each Half-Cycle for Maximum Lay-Down for 10 Cycles

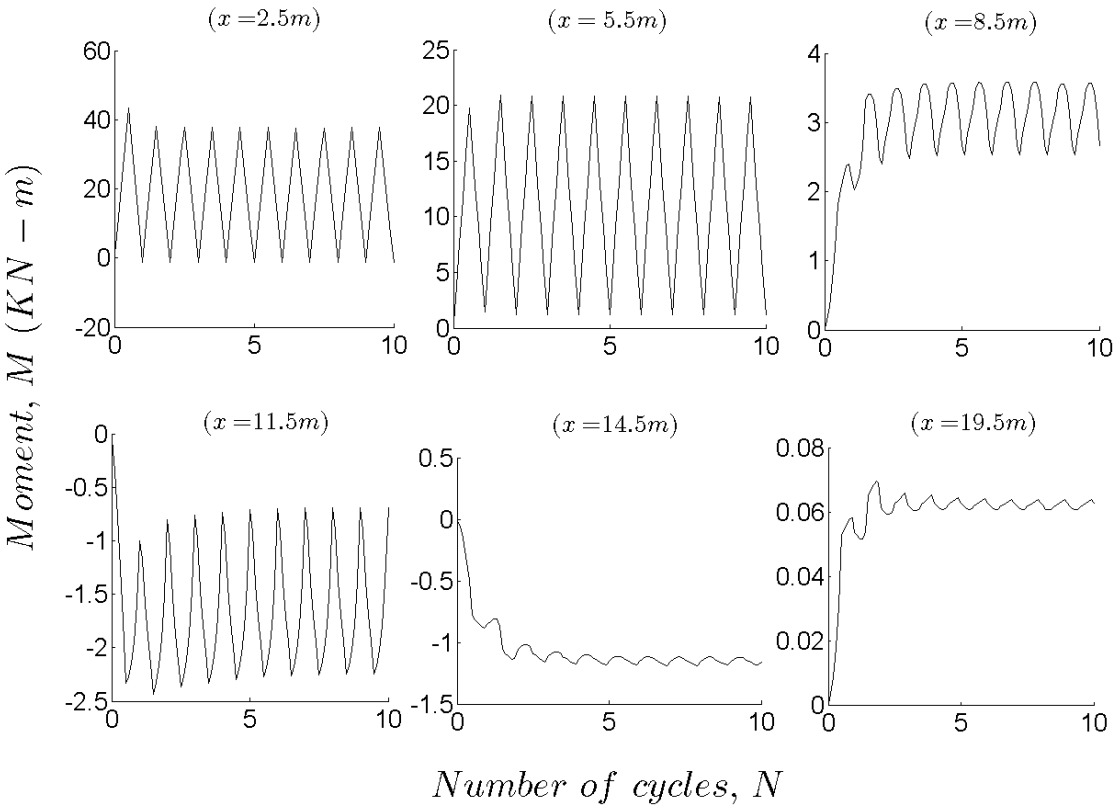

Fig. 95. Moment vs. Load Cycle at x = 2.5, 5.5, 8.5, 11.5, 14.5, and 19.5 m for u_{max} = 5D

5.6. Parametric Studies of Soil-Riser Interaction Model

5.6.1. Material Parameters

Fig. 96 and 97 show the deflection and moment variations for two different riser diameters (D). Parts (a) and (b) in figures are for maximum uplift and maximum lay-down cases. The large diameter riser leads to a greater self-weight penetration. In addition, the trench zone for the large diameter riser progresses toward the far field and forms a greater penetration depth and longer trench along riser length due to less curvature. Plus, since the rigidity of riser is related with section area of riser, maximum bending moment of D = 0.75 m is about 8 times larger than the maximum moment of D = 0.15 m for uplift motion ((a) in Fig.97).

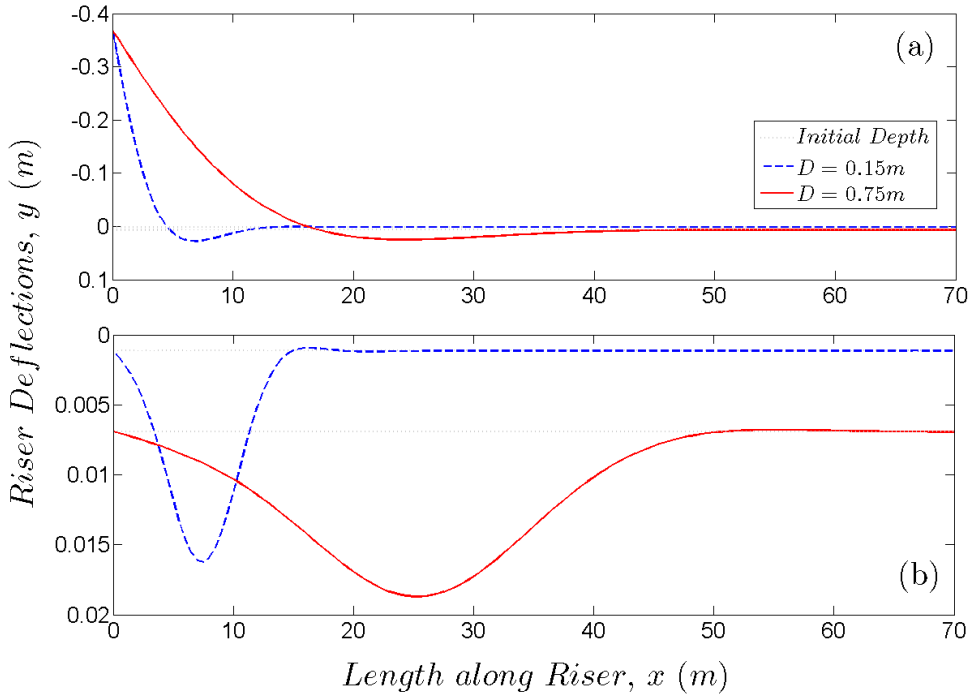

Fig. 96. Effect of Riser Diameter on Deflection

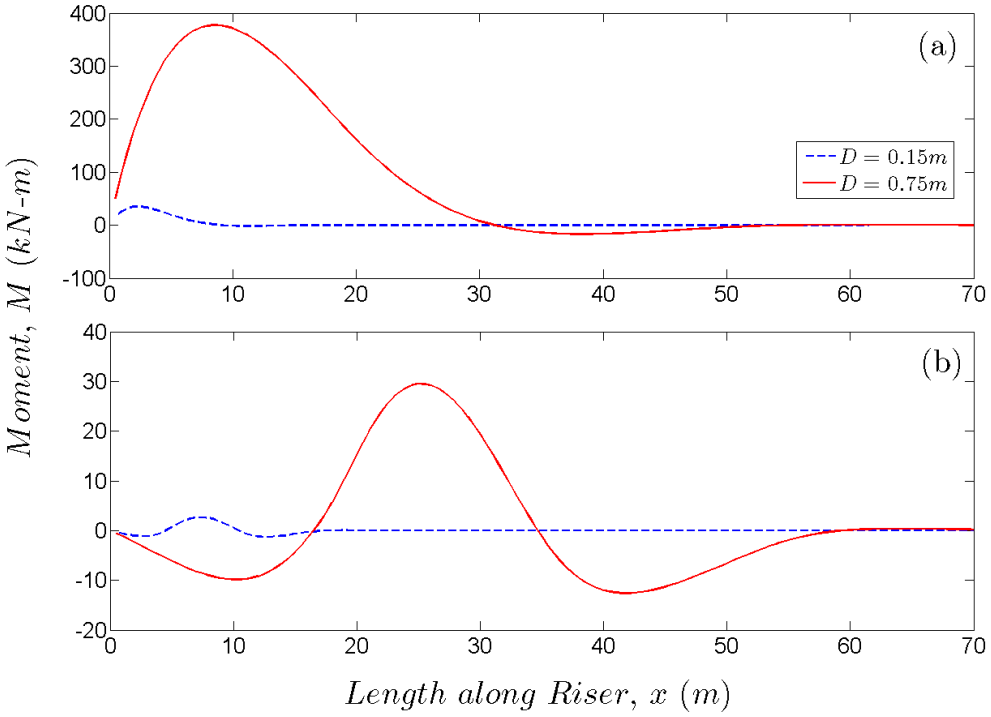

Fig. 97. Effect of Riser Diameter on Bending Moment

Fig. 98 and 99 describes the influence of soil parameters on deflection and moment evolutions. For maximum uplift and lay-down motions (a and b in Figures), both deflection and moment are sensitive to S_{uo}, the strength of mud-line. By contrast the strength gradient, S_g, has slight effect on riser configuration. The moment distribution for S_g = 13 kPa/m, is essentially the same as for S_g = 1.3 kPa/m. However; it should be noted that this simulation is for 1 cycle of loading. For repeated cyclic loading, more moment variation is expected.

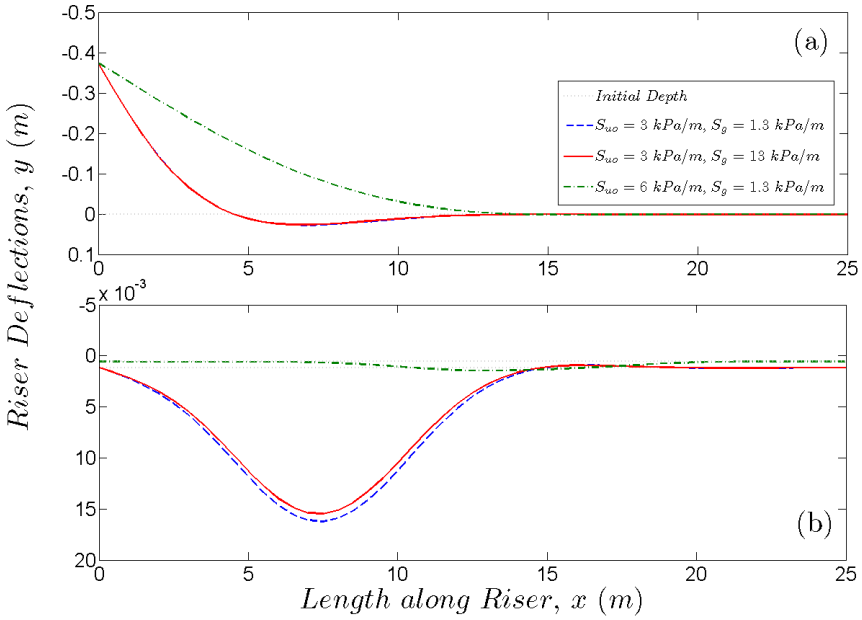

Fig. 98. Effect of Seabed Strength on Deflection

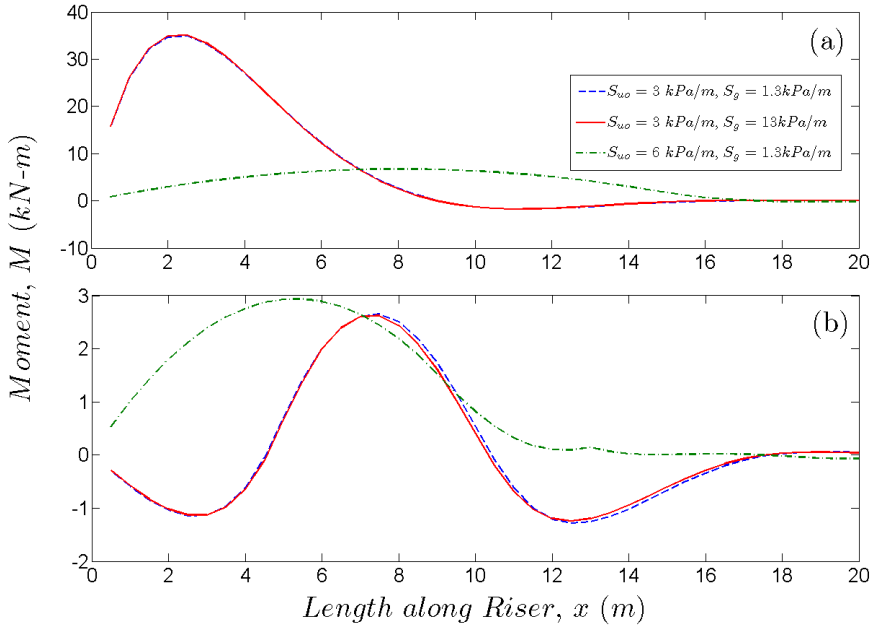

Fig. 99. Effect of Seabed Strength on Bending Moment

5.6.2. Loading Parameters

Loadings such as vertical displacement, tension, and rotational restraint directly influence riser deflections and moments. Figure 100 and 101 shows riser deflections and bending moments for maximum uplift and lay-down motion for u_{max} = 2.5D and 5.0D. The maximum moment immigrates to far side as loading size increases. Although the trench forms deeper shape by the large displacement loading, the trench length is unchangeable. Similar to effect of displacement loading, the deflection curves on three different tensions shows same trend (Figs. 102 and 103). However, the high tension leads less curvature at maximum penetration depth. For the largest tension (T = 100 kN), moment curve shape along riser length results from boundary constraints (Eq. 5.6).

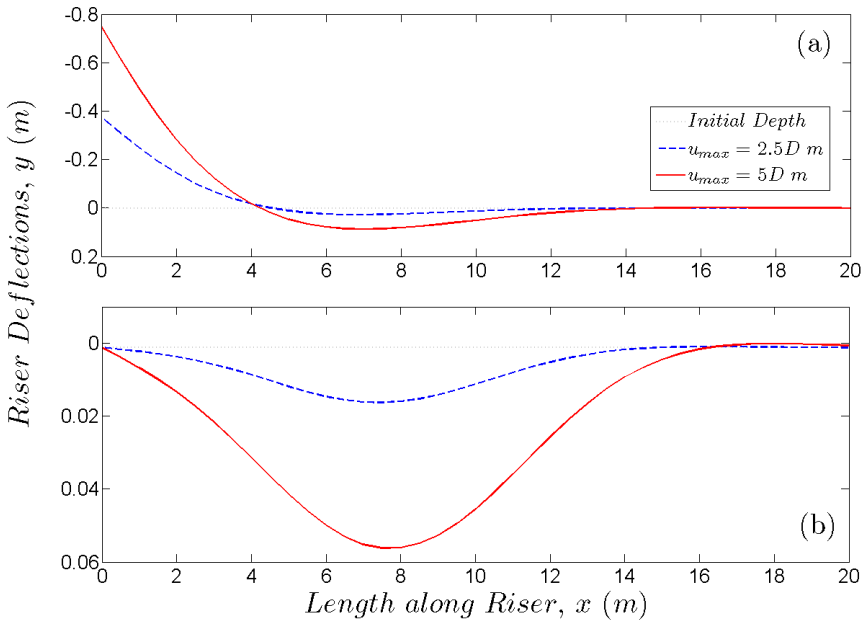

Fig. 100. Effect of Vertical Displacement at Touchdown Point on Deflection

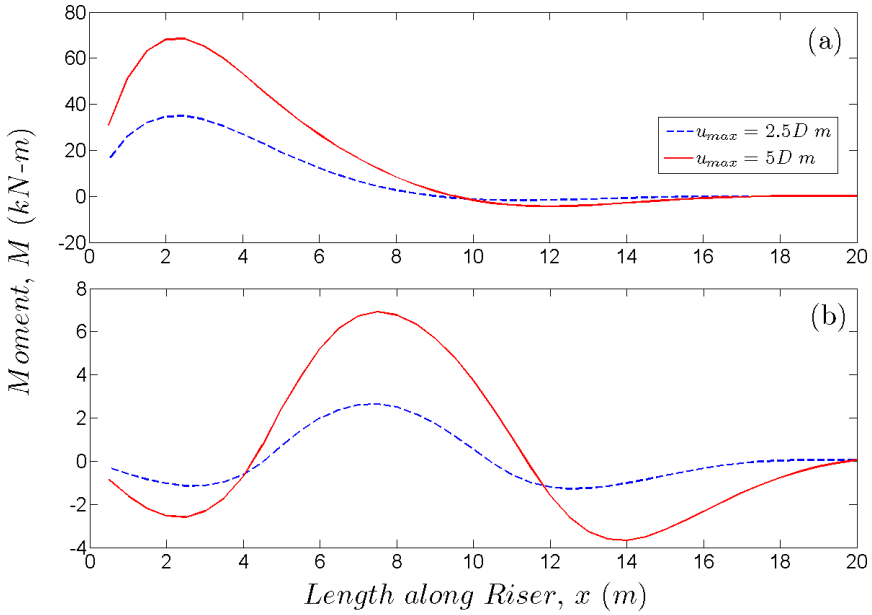

Fig. 101. Effect of Vertical Displacement at Touchdown Point on Bending Moment

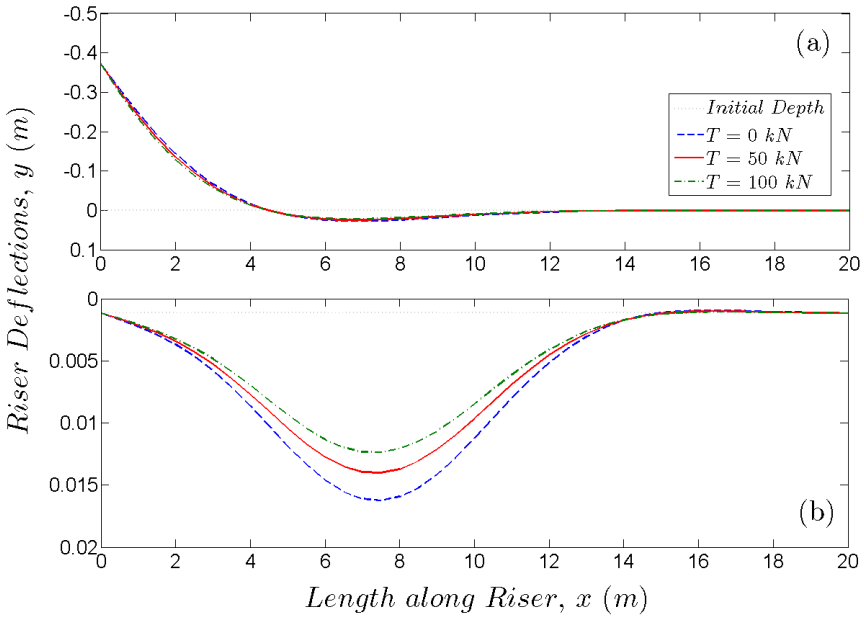

Fig. 102. Effect of Axial Load (Tension) on Deflection

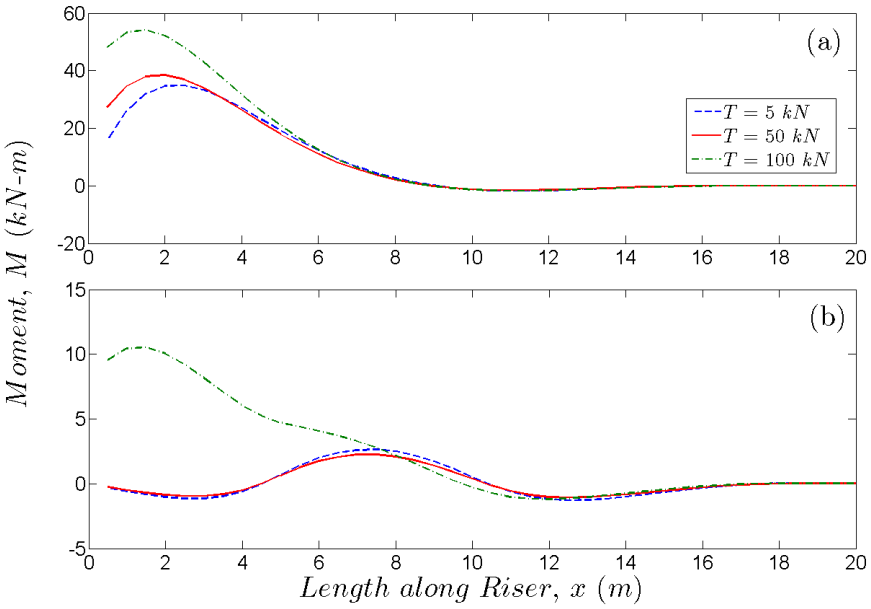

Fig. 103. Effect of Axial Load (Tension) on Bending Moment

5.6.3. Long Term Cyclic Effect

The following discussion addresses the effects of repeated cyclic loading on riser deflections and moments. Figure 104 shows riser configurations during 500 cyclic loading of u_{max} = 10 D. As the number of cycles increase, the riser is penetrates more deeply into the seabed. After 50 load cycles, 99% of the cumulative deflection at 500 cyclic load occurs. In addition, the point where the maximum curvature occurs moves rightward (toward the far field) with increasing cycles. Figure 105 illustrates the trench evolution with increasing load cycles. The location of the point of maximum depth of riser penetration is seen to shift rightward with increasing load cycles.

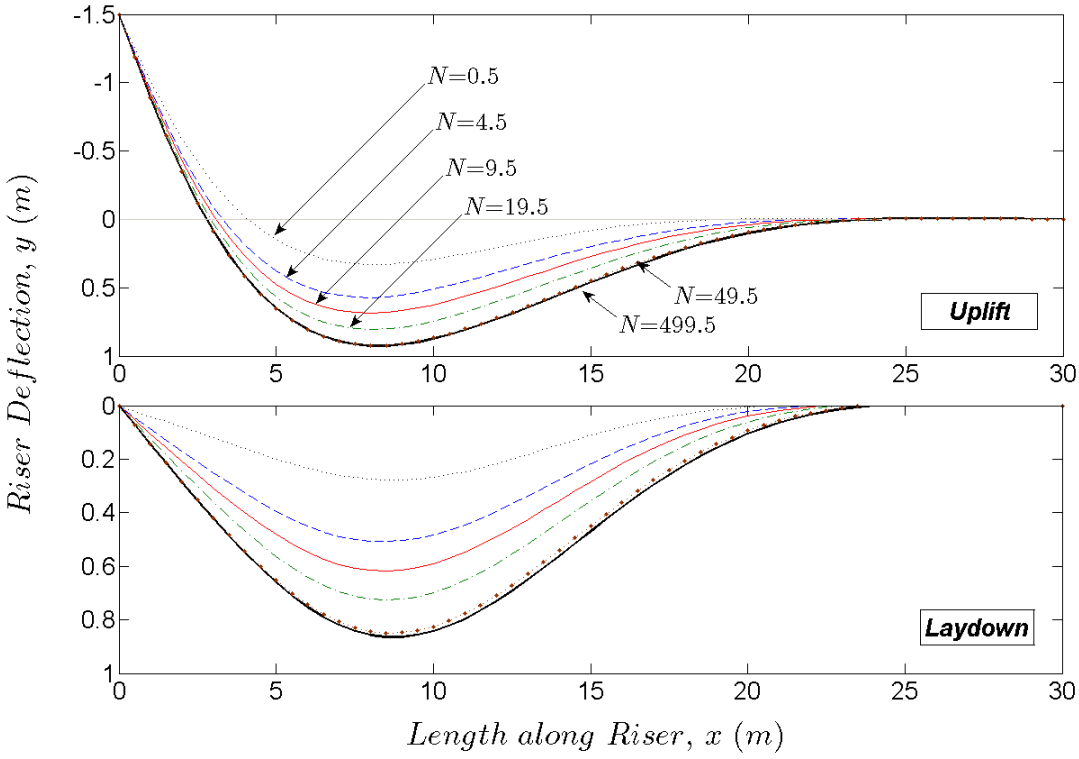

Fig. 104. Riser Configuration for Uplift and Lay-down Motion

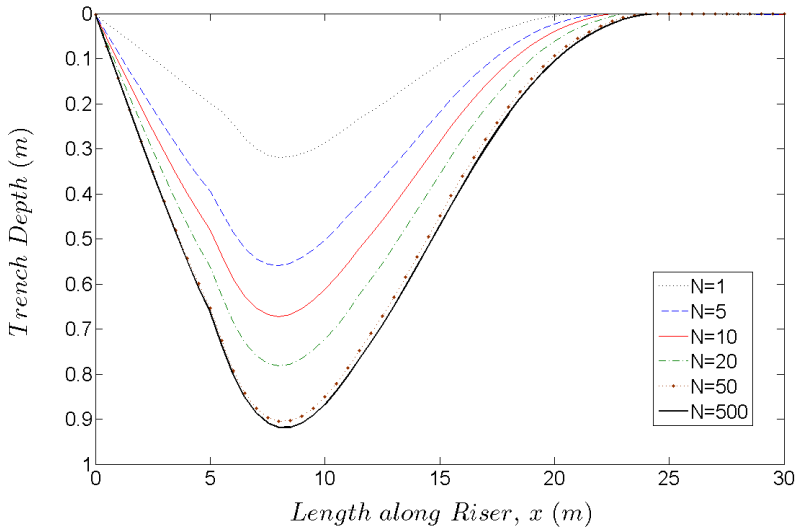

Fig. 105. Trench Evolution for Uplift and Lay-down Motion

Figure 107 presents load-displacement curves at three different locations, x = 5, 8, 14 m. Over 500 cycles, riser embedments progressively increases, but stabilize at depths of 0.55 , 0.67, and 0.93 m, respectively.

Figure 108 shows moment variation along riser length over 500 load cycles. With number of increasing cycles, moments increase for both of uplift and lay-down motions. However, the rate of moment variation for uplift motion is faster than the moment increment rate for lay-down motion. The maximum moment increases from 140 kNm in the first cycle to 165 kNm at end of 500 cycles, as shown in Fig. 110. Figure 109 illustrates that as load cycles increase, moments near the point of maximum penetration (x = 5 and 8 m) increase rapidly during the early stages of cyclic loading and then stabilize to constant values. At large distances from the touchdown point (x = 17 and 20 m), the moments are negative due to riser's reverse curvature.

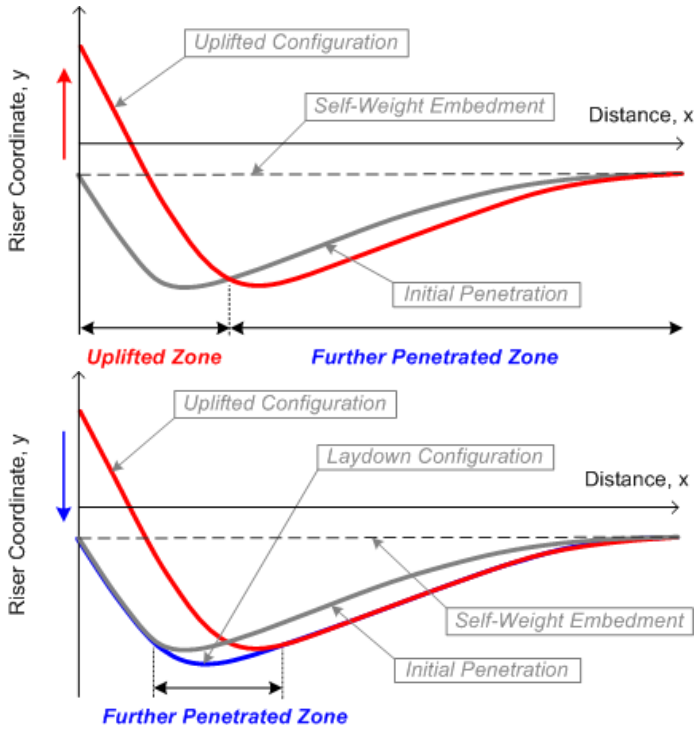

Fig. 106. Riser Shape Variation for Uplift and Lay-down Motion

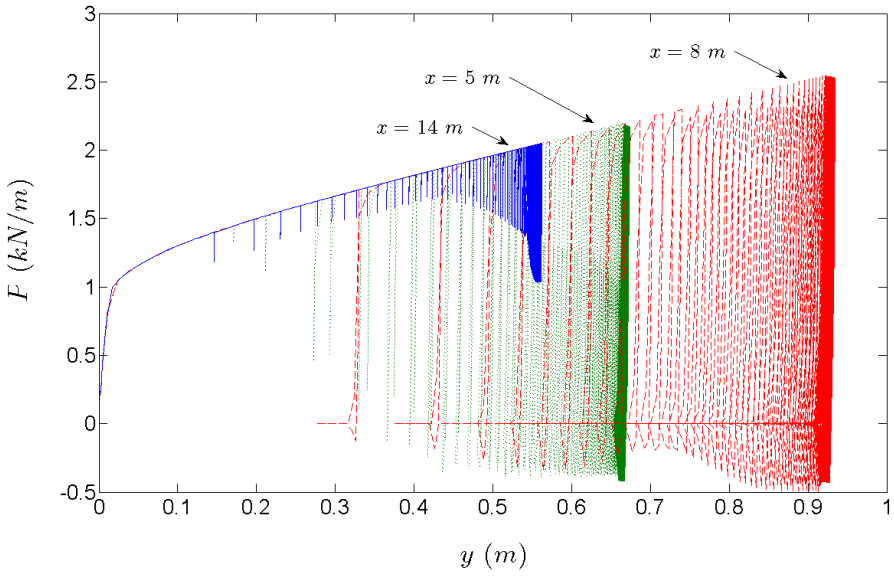

Fig. 107. P-y Curve for u_{max} = 10 D

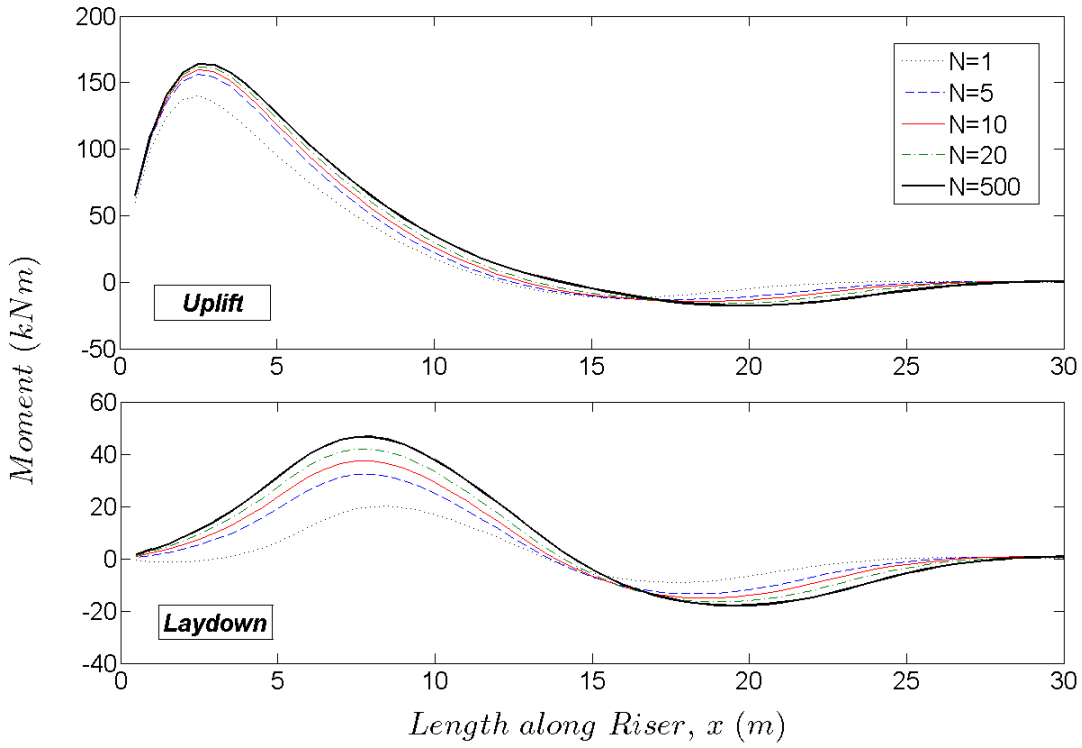

Fig. 108. Moment Variation along Riser Length for u_{max} = 10 D

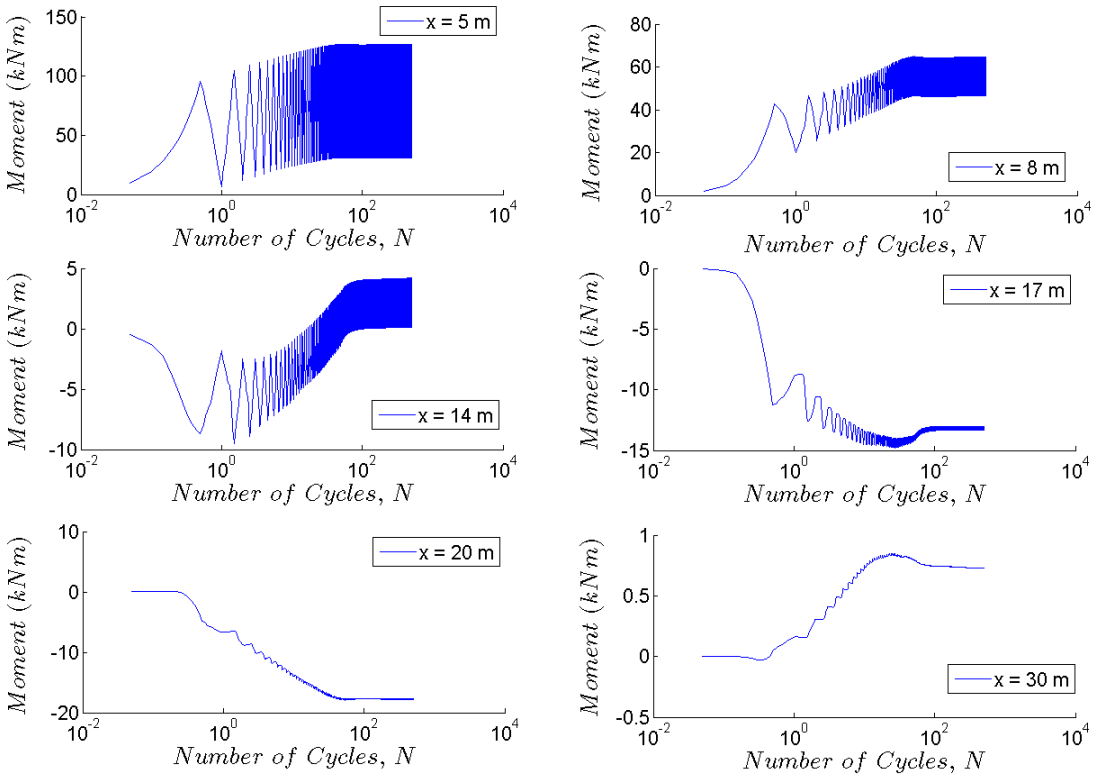

Fig. 109. Moment Variation at Points During 500 Cyclic Loading of u_{max} = 10 D

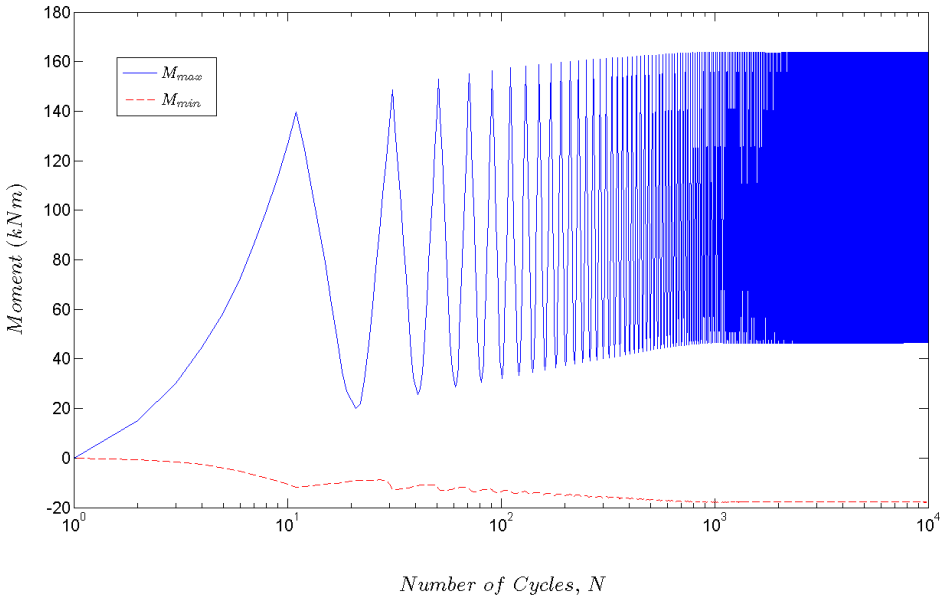

Fig. 110. Moment Variation at Points During 500 Cyclic Loading of u_{max} = 10 D

CHAPTER VI

SUMMARY AND CONCLUSIONS

6.1. Main Findings

A critical issue for steel catenary risers is the fatigue problem. It is not easy to predict fatigue life of a riser due to the uncertainty in complex seabed-riser interaction response. Previous research has focused on the vertical soil-riser interaction problem to better understand these issues and experimental tests were also carried out. Numerical linear or nonlinear soil stiffness models developed based on these experimental test. Linear models are simple and easy. Other advanced nonlinear soil models have limitations because they cannot account for all of phases of interaction behavior between between steel catenary risers and marine clay involving a number of complexities including non-linear soil behavior, soil yielding, softening of seafloor soils under cyclic loading, penetration rate effect, consolidation effect, variable trench width and depth, a wide range of possible riser displacement amplitudes, and conditions in which the riser pipe can actually pull out of contact with the soil. With a view toward making this complex problem more tractable, this research develops a non-linear degrading seabed model comprised of a riser pipe supported on a series of equivalent soil springs and a interaction model to predict riser configuration, trench evolution, moment variation along riser length. It makes possible to track the maximum moment at any point the user may be interested in and the location where the maximum moment occurs. The problem is then investigated through two sets of parallel studies.

6.1.1. Nonlinear Degrading Seabed Model

The proposed P-y approach was developed with both non-degrading and degrading soil stiffness models capable of describing initial plastic penetration into the seafloor, uplift

and reload cycles, fully detachment between seabed and riser, and load-deflection behavior within the bounding loop. The degrading soil model can introduce a reduction in soil stiffness under repeated loading. The proposed seabed models consists of backbone curve, unload-reload hyperbolic curves, and cubic curves including degrading parameters to describe soil-riser interaction response. The primary inputs into the model are seabed model parameters that can be derived from laboratory model tests involving a cyclically loaded pipe in a clay test bed. In addition, the in situ soil strength profile is required as an input parameter.

The Proposed model also has some limitations, but simulations show good agreement with experimental data. Hence, stiffness degradation and rate effects during penetration and uplift motion (suction force increase) of the riser are well captured through comparison with previous experimental tests carried out at NGI and COFS. It shoud be noted that the backbone curve of the seabed model was developed based on two-dimensional finite element studies of a pipe embedded in a trench for various conditions of trench depth, soil elastic modulus, and trench width. These studies were performed independently of the work presented in this dissertation by Sharma (2005), and the trench effect was not considered in the proposed seabed model.

6.1.2. Interaction Model

Seabed-riser interactions are modeled through one-dimensional studies of a spring-supported pipe subjected to displacements at one end of the pipe. Development of this model which can predict trench formation and bending moments in the riser based on a P-y approach is a primary focus of this research. The interaction model can show what variables have the most influence on the riser-seafloor interaction problem. Direct inputs into the interaction model include parameters to characterize the soil springs, the material properties such as riser pipe and soil profile, and the length of the touchdown zone. The riser pipe input

parameters include the elastic modulus of the pipe material (usually steel), pipe diameter, and the moment of inertia of the pipe cross-section. The pipe is modeled as a linearly elastic material. In addition, the proposed interaction model can handle any combination of amplitude of imposed displacements, tension, and moment. The amplitude of imposed motions is specified as a single vertical displacement. The imposed displacement can be either upward or downward. Primary outputs from this model include the deflected shape of the riser pipe and bending moments along riser length. The code also provides the location of maximum trench depth and the position where the maximum bending moment occurs.

The example simulations in this dissertation show that the magnitude of the displacement at the truncated boundary and the number of cycles are strongly related to trench formation and bending moments in the riser because the riser motion and trench evolution are interactive phenomena. As trench depth becomes deeper and the maximum trench depth moves due to the dynamic riser motion, the TDP, where maximum bending moment occurs, also migrates. Finally, the vertical displacement and riser tension at the touchdown point comprise the load inputs for the model in the examples presented here, but any combination of displacement, tension, and moment could be applied just as easily.

6.2. Recommendation for Future Research

Topics for future research include the following:

- Seabed Model Development:

  The current version of seabed model will be developed for more various conditions of trench width, trench backfill, consolidation related with rest time, and lateral loading.

- Fatigue Analysis:

  Prediction of the fatigue life of a riser needs maximum moments, which can be obtained through the proposed interaction model. Simulations by using measured data

on displacement and tension near TDP from monitored risers will allow additional verification of the models and possibly lead to modifications and improvements. Based on moment calculation by the proposed model, the 1st order fatigue analysis can be carried out.

- GUI model Development:

  The proposed work can be executed on a personal computer, and it was formulated with a view toward creating a design package readily accessible to designers. This method can be further developed into a design framework that will allow engineers to estimate the fatigue life of a riser system.

REFERENCES

Andersen, K. (2004). "Cyclic clay data for foundation design of structures subjected to wave loading." *Proc. of the Int. Conf. on Cyclic Behaviour of Soils and Liquefaction Phenomena*, Bochum, Germany, 31, 371–387.

Ashour, M. and Norris, G. (2000). "Modeling lateral soil-pile response based on soil-pile interaction." *J. Geotech. Geoenviron. Eng.*, 126, 420–428.

Ashour, M., Norris, G., and Pilling, P. (1998). "Lateral loading of a pile in layered soil using the strain wedge model." *Journal of Geotechnical and Geoenvironmental Engineering*, 124(4), 303–315.

Aubeny, C. and Biscontin, G. (2008). "Interaction model for steel compliant riser on soft seabed." *SPE Projects, Facilities & Construction*, 3(3), 1–6.

Aubeny, C., Gaudin, C., and Randolph, M. (2008). "Cyclic tests of model pipe in kaolin." *SPE Projects, Facilities & Construction*, 3(4), 1–6.

Aubeny, C., Shi, H., and Murff, J. (2005). "Collapse loads for a cylinder embedded in trench in cohesive soil." *International Journal of Geomechanics*, 5, 320–325.

Aubeny, C. P. and Biscontin, G. (2009). "Seafloor-riser interaction model." *International Journal of Geomechanics*, 9(3), 133–141.

Aubeny, C. P., Biscontin, G., and Zhang, J. (2006). "Seafloor interaction with steel catenary risers." Report No. 9/06A173, Texas A&M University, College Station, TX, 77845.

Beaufait, F. and Hoadley, P. (1980). "Analysis of elastic beams on nonlinear foundations." *Computers & Structures*, 12(5), 669–676.

Biscontin, G. and Pestana, J. (2001). "Influence of peripheral velocity on vane shear strength of an artificial clay." *ASTM Geotechnical Testing Journal*, 24(4), 423–429.

Bouwmeester, D., Peuchen, J., Van der Wal, T., Sarata, B., Willemse, C., Van Baars, S., and Peelen, R. (2009). "Prediction of breakout forces for deepwater seafloor objects." *Proc., Offshore Technology Conf.*, Houston, Texas, OTC 19925.

Bridge, C. and Howells, H. (2007). "Observations and modeling of steel catenary riser trenches." *Proc., 17th Intl. Symposium on Offshore and Polar Engineering*, Lisbon, Portugal, ISOPE-2007-468, 803–813.

Bridge, C., Howells, H., Toy, N., Parke, G., and Woods, R. (2003). "Full-scale model tests of a steel catenary riser." *Advances in Fluid Mechanics*, 36, 107–116.

Bridge, C., Laver, K., Clukey, E., and Evans, T. (2004). "Steel catenary riser touchdown point vertical interaction models." *Proc., Offshore Technology Conf.*, Houston, OTC 16628.

Bridge, C. and Willis, N. (2002). "Steel catenary risers–results and conclusions from large scale simulations of seabed interaction." *Proc., Int. Conf. on Deep Offshore Technology*, New Orleans, Penn Well.

Bruton, D., White, D., Cheuk, C., Bolton, M., and Carr, M. (2006). "Pipe/soil interaction behavior during lateral buckling." *SPE Projects, Facilities & Construction*, 1(3), 1–9.

Clukey, E., Haustermans, L., and Dyvik, R. (2005). "Model tests to simulate riser-soil interaction effects in touchdown point region." *International Symposium on Frontiers in Offshore Geotechnics*, Perth, Australia, 651–658.

Clukey, E., Jacob, P., and Sharma, P. (2008). "Investigation of riser seafloor interaction

using explicit finite element methods." *Proc., Offshore Technology Conf.*, Houston, OTC 19432.

Das, B. (1991). "Bottom breakout of objects resting on soft clay sediments." *International Journal of Offshore and Polar Engineering*, 1(3), 195–199.

Dawson, T. (1980). "Simplified analysis of offshore piles under cyclic lateral loads." *Ocean Engineering*, 7(4), 553–562.

Dunlap, W., Bhojanala, R., and Morris, D. (1990). "Burial of vertically loaded offshore pipelines in weak sediments." *Proc., 22nd Annual Offshore Technology Conf.*, Houston, OTC 6375, 263–270.

Fontaine, E., Nauroy, J., Foray, P., Roux, A., and Guéveneux, H. (2004). "Pipe-soil interaction in soft kaolinite: Vertical stiffness and damping." *Proc., 4th International Offshore and Polar Engineering Conference*, Toulon, France, 517–524.

Grashuis, A., Dieterman, H., and Zorn, N. (1990). "Calculation of cyclic response of laterally loaded piles." *Computers and Geotechnics*, 10, 287–305.

Hale, J., Morris, D., Yen, T., and Dunlap, W. (1992). "Modelling pipeline behavior on clay soils during storms." *Proc., Offshore Technology Conference*, Houston, OTC 7019.

Hatton, S. and Willis, N. (1998). "Steel catenary risers for deepwater environments." *Proc., Offshore Technology Conference*, Houston, OTC 8607, 1–14.

Hetényi, M. and of Michigan, U. (1946). *Beams on elastic foundation*. The Univ. of Michigan Press, Ann Arbor.

Howells, H. (1995). "Advances in steel catenary riser design." *The 2nd Annual International Forum on Deepwater Technology, DEEPTEC*, Aberdeen, UK.

Langford, T. and Aubeny, C. (2008). "Large scale soil-riser model testing on high plasticity clay." *Proc., 18th Int. Offshore and Polar Engineering Conf.*, ISOPE, Vancouver, Canada, 80–86.

Lunne, T. and Andersen, K. (2007). "Soft clay shear strength parameters for deepwater geotechnical design." *Offshore Site Investigation and Geotechnics, Confronting New Challenges and Sharing Knowledge*, SUT, London, UK, OSIG-07-151.

Matlock, H. (1970). "Correlations for design of laterally loaded piles in soft clay." *Annual Offshore Technology Conf.*, OTC, 1, 577–594.

Mekha, B. and Heijermans, B. (2003). "The prince tlp steel catenary risers: Design and fatigue challenges." *22nd Int. Conf. on Offshore Mechanics and Arctic Engineering*, ASME, Cancun, Mexico, 1, 119–126.

Mekha, B. B. (2001). "New frontiers in the design of steel catenary risers for floating production systems." *Journal of Offshore Mechanics and Arctic Engineering*, 123, 153–158.

Morris, D., Webb, R., and Dunlap, W. (1988). "Self-burial of laterally loaded offshore pipelines in weak sediments." *Proc., Offshore Technology Conf.*, OTC, Houston, 4, 421–428.

Murff, J., Wagner, D., and Randolph, M. (1989). "Pipe penetration in cohesive soil." *Geotechnique*, 39(2), 213–229.

Pesce, C., Aranha, J., and Martins, C. (1998). "The soil rigidity effect in the touchdown boundary-layer of a catenary riser: Static problem." *Proc., 8th Int. Offshore and Polar Eng. Conf.*, 2, 207–213.

Poinc, W. (1970). *Marine rescue operations (in Polish)*. Gdansk: Wydawnictwo Morskie.

Randolph, M. and Quiggin, P. (2009). "Non-linear hysteretic seabed model for catenary pipeline contact." *Proc., 28th Int. Conf. on Offshore Mechanics and Arctic Engineering*, OMAE, ASME, Honolulu, Hawaii, OMAE2009-79259.

Randolph, M. and White, D. (2008a). "Pipeline embedment in deep water: processes and quantitative assessment." *Proc., 40th Annual Offshore Technology Conf.*, Houston, Texas, OTC 19128.

Randolph, M. and White, D. (2008b). "Upper-bound yield envelopes for pipelines at shallow embedment in clay." *Géotechnique*, 58(4), 297–301.

Reese, L., Cox, W., and Koop, F. (1974). "Analysis of laterally loaded piles in sand." *Proc., Offshore Technology Conf.*, Houston, Texas, OTC 2080, 473–483.

Reese, L. and Desai, C. (1977). *Laterally loaded piles. In Numerical Methods in Geotechnical Engineering*. McGraw-Hill, 219–228.

Reese, L. and Welch, R. (1975). "Lateral loading of deep foundations in stiff clay." *Journal of the Geotechnical engineering division*, 101(7), 633–649.

Sawicki, A. and Mierczynski, J. (2003). "Mechanics of the breakout phenomenon." *Computers and Geotechnics*, 30(3), 231–243.

Skempton, A. (1951). "The bearing capacity of clays." *the Building Research Congress*, 1, 180–189.

Theti, R. and Moros, T. (2001). "Soil interaction effects on simple-catenary riser response." *Pipes and Pipelines International*, 46(3), 15–24.

Willis, N. and West, P. (2001). "Interaction between deepwater catenary risers and a soft seabed: large scale sea trials." *Proc., Offshore Technology Conf.*, Houston, Texas, OTC 13113.

VITA

Jung Hwan You earned his Bachelor of Science degree in civil engineering from Yeungnam University, Gyeongsan, Korea, in February 2002. In August 2003, he entered the Graduate School of Texas A&M University, College Station, Texas and received his Master of Science degree with specialty in civil engineering from Texas A&M University in December 2005 under the supervision of Dr. Aubeny. While in graduate school, he was employed as a graduate research assistant and teaching assistant. In August 2007, he was awarded the department head fellowship. He earned his Ph.D. degree from Texas A&M University in August 2012. His research interests include foundations and anchors for offshore structures, offshore risers and pipelines, dynamic response of soils, numerical methods and modeling in geomechanics. His email address is jhyeo911@gmail.com.

Department of Civil Engineering care of Dr. Giovanna Biscontin, 3136 TAMU, Department of Civil Engineering, Texas A&M University, College Station, Texas 77843

The typist for this dissertation was Jung Hwan You.